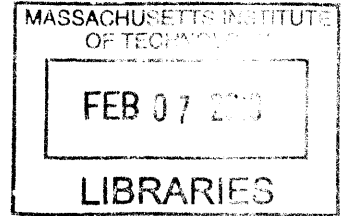


**A Microfluidic Platform for Combinatorial Synthesis and
Optimization of Targeted Polymeric Nanoparticles for Cancer Therapy** **ARCHIVES**

by

Pedro M. Valencia



M.S. Chemical Engineering Practice, Massachusetts Institute of Technology, 2009
B.S. Chemical Engineering, University of Wisconsin-Madison, 2007

Submitted to the Department of Chemical Engineering in
Partial Fulfillment of the Requirements for the Degree of

Doctor of Philosophy in Chemical Engineering
at the
Massachusetts Institute of Technology

~~November 2012~~
[February, 2013]

© Massachusetts Institute of Technology
All rights reserved

Signature of Author

Pedro M. Valencia
Department of Chemical Engineering
November 21st 2012

Certified by

Robert S. Langer
Institute Professor, MIT
Thesis Supervisor

Certified by

Rohit Karnik
Associate Professor of Mechanical Engineering, MIT
Thesis Supervisor

Certified by

Omid Farokhzad
Associate Professor of Anesthesia, Harvard Medical School
Thesis Supervisor

Accepted by

Patrick S. Doyle
Professor of Chemical Engineering
Chairman, Committee for Graduate Students

A Microfluidic Platform for Combinatorial Synthesis and Optimization of Targeted Polymeric Nanoparticles for Cancer Therapy

By

Pedro M. Valencia

Submitted to the Department of Chemical Engineering

On November 21st, 2012 in partial fulfillment of the requirements for the degree of
Doctor of Philosophy in Chemical Engineering

ABSTRACT

The use of nanotechnology to engineer drug delivery vehicles comprised of controlled release polymers with targeting molecules has the potential to revolutionize cancer therapy, among other diseases. Although a myriad of nanotherapeutics have been developed at the bench side, many of them stay at the research stage due to their complexity and difficulty in their optimization. A key challenge for optimization of nanoparticles (NPs) for drug delivery is the ability to systematically and combinatorially create and screen libraries of NPs with distinct physicochemical properties, from which promising formulations can be moved forward to pre-clinical and clinical studies.

In this work, the development of a controlled method to synthesize libraries of NPs with distinct properties is described. The procedure uses a microfluidic platform that rapidly mixes reagents and provides homogeneous reaction environments, resulting in the reproducible, single-step synthesis of NPs with well-defined properties and narrow size distributions. The microfluidic system is composed of a mixing unit and a NP assembly unit. The mixing unit consists of a multi-inlet, 2-layer mixer where different precursors such as polymers of different MW and charge, ligand- and drug-conjugated polymers, free drugs, and solvents are mixed at different ratios into a homogenous solution. In the assembly unit, the precursor solution is quickly mixed with an anti-solvent (i.e. water) using 3D hydrodynamic flow focusing where NPs self-assemble after complete mixing.

With the microfluidic platform, a library of 100 NPs with different sizes (15-200nm), charge (-30 to +30mV), surface chemistry (i.e. PEG coverage), surface ligand density ($0-2.5 \cdot 10^5$ ligands/ μm^2), and drug loading (0-5 w/w%) was produced in a high-throughput manner by simply varying the flow ratios of precursors entering the system. This library was implemented for (i) screening for formulations (*in vitro* and *in vivo*) with optimal clinical properties for cancer treatment and (ii) deepening the understanding of how NP properties affect their biological behavior. The platform developed in this work would likely lead to better understanding of the design parameters for polymeric NPs and their smoother transition to the clinic.

Thesis Supervisors: Institute Professor Robert Langer (Chemical Engineering, MIT)
Professor Rohit Karnik (Mechanical Engineering, MIT)
Professor Omid Farokhzad (BWH and Harvard Medical School)

Thesis Committee: Professor Michael Cima (Materials Science and Engineering, MIT)
Professor Paula Hammond (Chemical Engineering, MIT)

Acknowledgements

First, I would like to acknowledge my three advisors, Bob, Omid, and Rohit. I believe I have been one of the few privileged students to receive constant orientation and guidance at many levels including the experimental and analytical side (Rohit), clinical and business side (Omid) and translation and entrepreneurial side (Bob).

Rohit, thank you for the numerous meetings we had, always helpful in making my roadblocks almost inexistent. The robustness and thoroughness of your work is something I will always try to apply in my own work. Omid thank you for all our meetings, late phone calls, and powerful advices. Most of the inspiration in setting my career goals came from you. I learned tremendously from you in many ways. Bob, thank you for the timely and impactful feedback I always received from you. You amazed me every time you got back to me early in the morning, late at night, during weekends and holidays, as if I was the only lab member—I'm sure the other 120+ members, hundreds of alumni, and tens of companies think the same.

I want to thank the members of my thesis committee, Michael Cima and Paula Hammond. I certainly had an all-star thesis committee. Michael, thank you for all your inspiring advises and useful conversations we had (especially those informal ones at the Koch institute halls). Paula, you were key in my success at MIT. Besides receiving great feedback on my work, I will always remember the summer I spent in your lab in 2005 where I was introduced to the field of drug delivery.

I want to thank all the members of the Langer Lab, Karnik Lab, and Farokhzad labs. Especially I want to thank Eric Pridgen and Aleks Radovic-Moreno: we had many laughs and I truly enjoyed working with you guys.

I want to thank few Langer lab alumni that helped shaped my goals immensely, especially Amir Nashat (the first time I heard about venture capital was from you in Hawaii), and David Berry (I learned so much from you at Flagship, especially how to poke holes on business ideas with the goal to make them better and stronger). Others include, Larry Brown, Anita Peil, Liangfang Zhang, Jeff Hrkach, Maria Jose Alonso, Jason Fuller, Seth Townsend, Tanguy Chau, Christopher Prtichard, and David Lynn (my professor at UW-Madison).

I also want to thank MIT's office of the Dean for Graduate Education, especially Dean Christopher Jones and Monica Orta. Dean Jones, thank you for that unforgettable MSRP summer experience in 2005. This is where I learned and acknowledge that getting to MIT was certainly possible, even if one comes from a community college where most students are underrepresented minorities.

I want to thank all my 15 siblings and 26 nephews and nieces for all the inspiration and support received throughout these years. I especially want to thank my sister Maria del Pilar for always believing in me and supporting me in many ways.

I want to dedicate this thesis to my Mom and Dad. I believe this achievement is theirs as much as it is mine. I will always thank my dad for the sacrifice of leaving home when I was very young to come to United States and set the pathway for my arrival almost 10 years later. I thank my mom's infinite prayers and never-ending care for my well-being. My parents taught me all principles and values I practice, which are even greater than any other degree.

Finally, I want to thank my beautiful wife, Laura, and my little angels Lucia and Felipe. I am the happiest man in the world thanks to my wife and children. Laura, none of my accomplishments would have been possible without you holding the fort at home while I was working late. We as a family are one person, and the success of one is the success of all. I can't thank you enough.

Table of Contents

Chapter 0 – Outline of thesis.....	10
Chapter 1 - Introduction: Microfluidic Technologies for Accelerating the Clinical Translation of Nanoparticles	12
1.1. Promises and limitations in nanomedicine	12
1.2. Well-controlled synthesis of nanoparticles.....	15
1.3. Evaluation and screening of nanoparticles	20
1.4. Future prospects	24
1.5. References.....	27
Chapter 2 - Microfluidic System for Synthesis of Multifunctional Nanoparticles: 2D Flow Focusing with Tesla Structures	31
2.1. Introduction.....	31
2.1. Microfluidic device and nanoparticle design.....	33
2.2. Characterization of PLGA-lipid NPs	35
2.3. Control of NP physicochemical properties: Size and surface charge	39
2.4. Investigating the role of rapid mixing and mechanism of self-assembly of the hybrid nanoparticles	40
2.5. Preparation of lipid-QD NPs.....	46
2.6. Conclusion	48
2.7. Experimental methods	49
2.8. References.....	51
Chapter 3 - Microfluidic System for Synthesis of Multifunctional Nanoparticles: 3D Flow Focusing	54
3.1. Introduction.....	54
3.2. Design of microfluidic device.....	56
3.3. Comparison of 2D versus 3D flow focusing.....	58
3.4 Effect of channel geometry on device performance	62
3.5. Conclusion	64
3.6. Materials and methods	65

3.7. References.....	68
Chapter 4 - Understanding Targeted Nanoparticles: Effects of Ligands with Different Water Solubilities on Self-Assembly and Properties of Targeted Nanoparticles	71
4.1. Introduction.....	71
4.2. Synthesis of PLGA-PEG-RGD and PLGA-PEG-Folate	74
4.3. Synthesis of RGD- and folate-targeted NPs	76
4.4. NP-RGD and NP-Folate ligand densities	77
4.5. Cellular binding and uptake of targeted nanoparticles	80
4.6. Conclusion	84
4.7. Materials and methods	85
4.8. References.....	90
Chapter 5 - Next Generation Nanoparticles: Synthesis of Nanoparticles Encapsulating Multiple Drugs.	93
5.1. Introduction.....	93
5.2. Irinotecan and cisplatin in targeted polymeric nanoparticles	97
5.3 PLGA-PEG-LIG and PLA-Pt polymer synthesis	98
5.4. Microfluidic synthesis of nanoparticles.	100
5.5. Characterization of nanoparticles encapsulating cisplatin and irinotecan	103
5.6. Cell targeting of nanoparticles decorated with LIG.....	105
5.7. Synergistic cytotoxicity of irinotecan-cisplatin nanoparticles.....	106
5.8. Conclusion	108
5.9. Materials and methods	109
5.10. References.....	112
Chapter 6 - Putting all together: Microfluidic Platform for Combinatorial Synthesis and Optimization of Targeted Nanoparticles for Cancer Therapy	116
6.1. Introduction.....	116
6.2. Design and operation of microfluidic platform	118
6.3. Synthesis of nanoparticle library	119
6.4. High-throughput synthesis and screening of nanoparticles	122
6.5. Passive versus active nanoparticle targeting.....	124

6.6. Conclusion	127
6.7. Materials and methods	128
6.8. References.....	132
Chapter 7 - Outlook: The Relationship Between Nanoparticles Properties and Biological Behavior—a Deep Dive.....	135
7.1. Introduction.....	135
7.2. What we have learned so far	136
7.3. Three key research directions	137
7.4. References.....	141
Appendix 1. Supporting information for chapter 2.....	144
Appendix 2 – Supporting information for chapter 3.....	149
Appendix 3 – Supporting information for chapter 4.....	151
Appendix 4. Supporting information for chapter 6.....	153

List of Figures

Figure 0.1 Schematic representation of the microfluidic platform developed and the thesis outline.	11
Figure 1.1. Nanoparticles in clinical development, steps for their translation and microfluidic methods that could improve or complement current technologies.	15
Figure 1.2. Microfluidic synthesis of nanoparticles.....	19
Figure 1.3. Microfluidic systems for <i>in vitro</i> evaluation and screening of nanoparticles.	23
Figure 2.1. Nanoprecipitation of lipid-polymeric nanoparticles.....	35
Figure 2.2. Characterization of Lipid-PLGA structure.....	36
Figure 2.3. Control of nanoparticle physicochemical properties.....	40
Figure 2.4. Slow versus rapid mixing.	42
Figure 2.5. NP formation to elucidate stepwise formation of hybrid lipid-polymer NPs within microchannel.....	44
Figure 2.6. Preparation of hybrid lipid-QD NPs.....	48
Figure 3.1. Device design and representative nanoparticles.....	57
Figure 3.2. Comparison of 3D HFF, 2D HFF, and bulk nanoprecipitation of PLGA-PEG NPs under different conditions.	61
Figure 3.3. Simulation and visualization of focused stream.	63
Figure 4.1. Polymer synthesis and Nanoparticle design.	75
Figure 4.2 Characterization of targeted NP-RGD and NP-Folate.	77
Figure 4.3. Quantification of targeted NP surface composition.	80
Figure 4.4. Cellular binding and uptake of targeted NPs as a function of % of functionalized PLGA-PEG added in the NP formulation.....	83
Figure 5.1. Strategy of co-encapsulation of irinotecan and cisplatin in a single nanoparticle targeted to PSMA receptors in prostate cancer cells.	98
Figure 5.2. Polymer synthesis.....	100
Figure 5.3. Single-step synthesis of targeted nanoparticles in microfluidic devices using hydrodynamic flow focusing.	102

Figure 5.4. Characterization of nanoparticles containing either irinotecan (NP _I) or cisplatin (NP _C) prodrug or both (NP _{I&C}).....	104
Figure 5.5. Uptake of PSMA-targeted NPs in LNCaP cells overexpressing PSMA receptors compared to non-targeted NPs.....	106
Figure 5.6. Cytotoxicity of nanoparticles with irinotecan and cisplatin.	108
Figure 6.1. Microfluidic platform for high-throughput synthesis of nanoparticles.	119
Figure 6.2. Synthesis of NPs with control over physicochemical properties.	121
Figure 6.3. Synthesis and in vitro and in vivo screening of 45 NPs with different sizes and PEG coverage.....	124
Figure 6.4. Comparison of biodistribution and tumor accumulation of targeted and non-targeted NPs with similar biophysicochemical properties.....	127
Figure 7.1. Questions to answer in future work.....	139
Figure A1.1. Changes in average NP size dependency on lipid:polymer (wt/wt).....	144
Figure A1.2. Effect of time on NPs made with different precursors and at different conditions.	145
Figure A1.3. Effect of DSPE-PEG in stability of lipid-PLGA NP.....	146
Figure A1.4. Size distribution of hybrid NPs with different properties.....	147
Figure A1.5 Determination of mixing time.	148
Figure A1.6. Observation of self-assembly.	148
Figure A2.1. Synthesis of PLGA NPs.	149
Figure A2.2. Comparison of size distributions by volume fraction of PLGA-PEG NPs.	149
Figure A2.3. Cloudiness of various PLGA-PEG NPs.	150
Figure A3.1 . MALDI-TOF to verify conjugation of PEG-RGD and PEG Folate.....	151
Figure A3.2. UV-VIS to quantify amount of folate present on PLGA-PEG-Folate.....	152
Figure A3.3. 1H NMR on PLGA-PEG-Folate.....	152
Figure A4.1. NP precursors used for the synthesis of NP library with a wide range of physicochemical properties.....	153
Figure A4.2. Batch-to-batch reproducibility of targeted NPs prepared in the microfluidic system.	154
Figure A4.3. Average size and zeta potential of non-targeted NPs (NT-NP) and targeted NPs (TNP).	154

List of Tables

Table 1: Advantages, disadvantages/challenges, stage of development, and potential impact of microfluidic systems on different steps in the clinical translation of nanoparticles.	27
Table A3.1. Gel Permeation Chromatography (GPC) on TL-conjugated and non-conjugated PLGA-PEG copolymers.....	151

Chapter 0 – Outline of thesis

This work describes the development of a versatile microfluidic platform for the high-throughput synthesis and optimization of targeted polymeric nanoparticles. The platform is useful for the production of nanoparticle libraries, with which one can (i) rapidly screen for nanoparticles with promising clinical properties and (ii) obtain deeper understanding on how nanoparticle properties affect their biological behavior. A schematic that summarizes this work is shown in Figure 0.1. Chapter 1 starts with an overview of the field of nanomedicine, clearly delineating how microfluidics can make an impact in the immediate and long term in the acceleration of discovery and clinical translation of nanoparticles. Subsequently, three distinct topics are discussed in chapters 2 to 5:

(1) Fabrication of microfluidic devices that can synthesize multifunctional polymeric and lipid nanoparticles (chapters 2 and 3). The two main goals were to develop ways to synthesize a variety of nanoparticles with potential for clinical translation (chapter 2) and to make them in a device that minimizes fouling and batch-to-batch variations (chapter 3).

(2) Gain of deeper understanding on targeted nanoparticles. Specifically, understand how the nature of the targeting ligand affects other particle properties as well as their biological

behavior. This work has broader impact when it comes to choosing a targeting ligand for a specific nanoparticle system.

(3) Development of ways of encapsulating multiple drugs in the same nanoparticle. Specifically, the synthesis of a polymer-drug system is described, as well a robust method of incorporating them inside nanoparticles in a precise and reproducible manner through microfluidics.

Finally, with the devices developed in chapter 3, plus the knowledge learned in chapter 4, and the materials synthesized in chapter 5, the microfluidic platform was assembled and tested (chapter 6). With this system, a proof-of-concept nanoparticle library was produced, a high-throughput screening was performed, and insightful in vivo studies were carried out. This thesis closes with the description of three questions that are still unanswered in the field of nanomedicine, and for which the microfluidic platform is well suited to be used as tool to answer them (chapter 7).

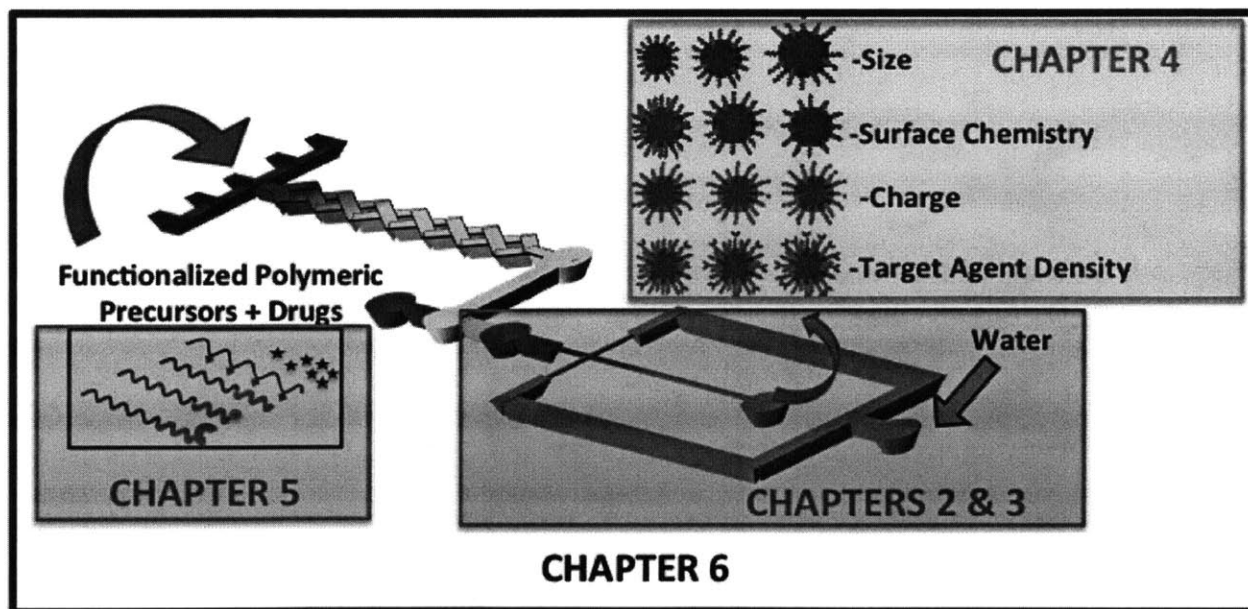


Figure 0.1 Schematic representation of the microfluidic platform developed and the thesis outline.

Chapter 1 - Introduction: Microfluidic Technologies for Accelerating the Clinical Translation of Nanoparticles

1.1. Promises and limitations in nanomedicine

Nanomedicine is the application of nanotechnology to medicine, specifically involving the use of engineered nanomaterials for therapy and diagnosis of major diseases such as cancer, cardiovascular, and infectious diseases¹. The first generation of nanoparticles with applications in medicine dates back to the 1970's, when drug-loaded nanoscale liposomes were developed to deliver their cargo to diseased cells in a "Trojan horse" fashion². Since then a new generation of targeted drug delivery vehicles (for example, polymeric nanoparticles)³, contrast agents (such as iron oxide nanoparticles)⁴, diagnostic tools⁵, and antennas for photothermal therapy (for example, gold nanoparticles)⁶ have emerged. This is driven in part by further understanding of the biology of diseased states, and by technological advances in imaging techniques and synthesis of novel biocompatible and biodegradable materials⁷. Today, nanomedicine promises the precise delivery of drugs to disease sites (such as tumors and atherosclerotic plaques) without

off-target toxicities, and the early detection of diseases using selective contrast agents and sensitive diagnostic tools⁸.

Nanoparticles are attractive in medicine because their surfaces can be chemically modified for targeting specific disease tissues, or for *in vivo* stability. For therapy, drugs can be encapsulated inside nanoparticles and released in a controlled manner over time. For imaging, nanoparticles can provide higher contrast (e.g. iron oxide nanoparticles for magnetic resonance imaging, MRI) or higher brightness (e.g. QDs for fluorescence imaging) than conventional small molecule agents⁹. Despite these advantages and several decades of research, only a handful of nanoparticles have received approval from the US Food and Drug Administration. Few examples include Feridex and Resovist (iron oxide nanoparticles for magnetic resonance imaging, MRI), Doxil (liposome encapsulating doxorubicin for chemotherapy) and Abraxane (protein-based nanoparticle encapsulating paclitaxel for chemotherapy)¹⁰.

In fact, translation of nanoparticles to the clinic has been slow compared to small-molecule drugs, with the majority of nanoparticles not even reaching the point of *in vivo* evaluation, and even fewer reaching clinical trials. This is due to a combination of factors. It remains difficult to reproducibly synthesize batches of nanoparticles that have identical properties and in sufficient quantities for clinical applications¹¹. Moreover, knowledge on the fate of nanoparticles at the body-, organ- and cell-level remains limited¹²; this makes rational design of nanoparticles difficult and necessitates the use of screening-based approaches for synthesis. Furthermore, there are few platforms that can rapidly evaluate the biological behavior of nanoparticles *in vitro* under conditions that can be correlated with their performance *in vivo*¹¹. For example, there is a need for high throughput methods for evaluating the binding and internalization of nanoparticles by cells, the interaction of nanoparticles with plasma proteins and

the immune system, among others. Finally, there is insufficient understanding of the biophysicochemical interactions of nanoparticles with proteins, membranes, DNA, and organelles. These interactions could have either beneficial or adverse outcomes¹³. It is expected that technologies tackling some of these challenges could significantly accelerate the discovery and clinical translation of nanomedicines.

Microfluidics, the science and technology of manipulating nanolitre volumes in microscale fluidic channels, has impacted a range of applications including biological analysis, chemical synthesis, single cell analysis, and tissue engineering¹⁴. Building upon its origins in semiconductor technology and chemical separations, the expansion of microfluidics has been driven by its ability to process small sample volumes and access biologically relevant length scales and microscale transport phenomena. This expansion has been largely facilitated by techniques, such as soft lithography, that enable rapid design and prototyping of microfluidic devices using a variety of materials¹⁴. Recent advances and innovations in microfluidics are expected to improve the synthesis of nanoparticles and accelerate their transition to clinical evaluation (Figure 1.1). Although many of these microfluidic systems are still being developed, they have the potential to become widely adopted because they are economical, reproducible, amenable to modifications, and can be integrated with other technologies¹⁵. In the next sections, we highlight some of these technologies and discuss their impact on accelerating the clinical translation of nanoparticles.

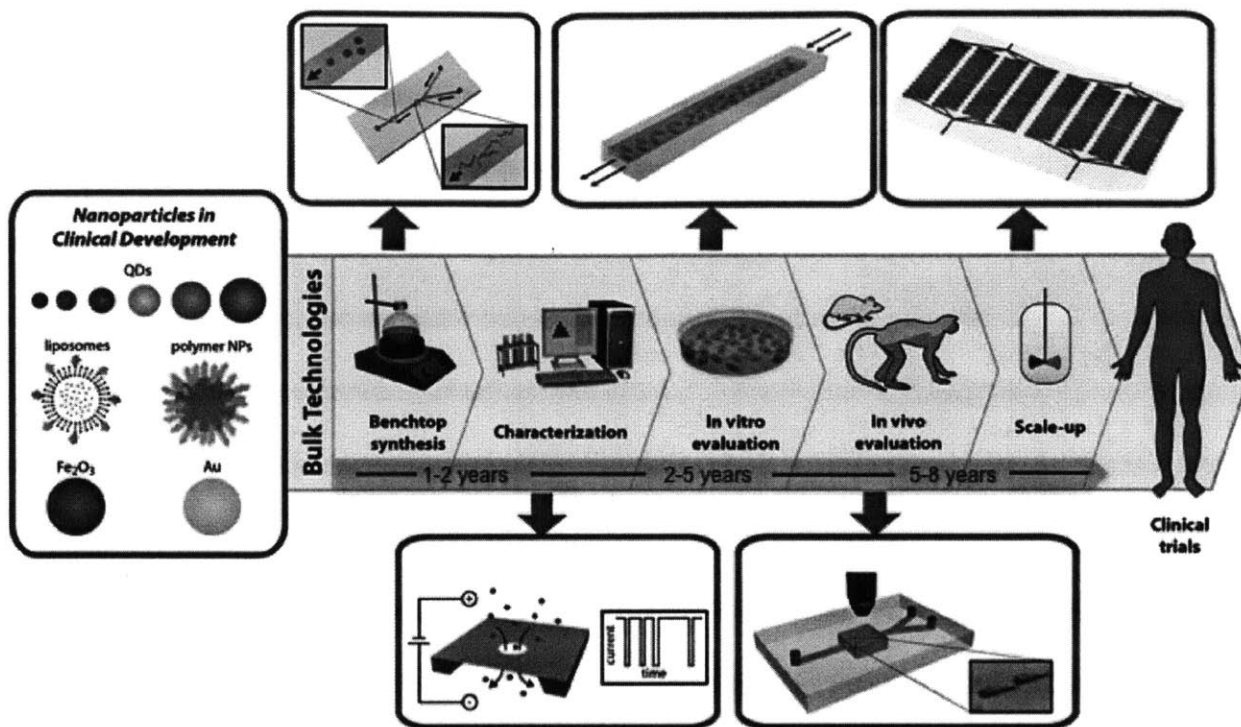


Figure 1.1. Nanoparticles in clinical development, steps for their translation and microfluidic methods that could improve or complement current technologies.

Synthesis is carried out in large reaction flasks, whereas microfluidic synthesis is carried out at micro and nano lengthscales that allow for improved control over reaction conditions. Characterization often involves taking a small sample of nanoparticles and measuring their properties offline, while nanopores embedded in microfluidic devices allow for real time, in-line characterization. In vitro evaluation in plate wells produces a microenvironment far from that in vivo, while continuous flow in microfluidic systems result in conditions closer to those in vivo. In vivo evaluation in large animals is helpful for estimating the pharmacology of nanoparticles. To complement these studies microfluidic systems could enable real-time tracking of nanoparticles in large numbers of small organisms. Scale-up is generally carried out in reactor vessels several times larger than bench top flasks, while parallelization of microfluidic channels can increase the production rate of nanoparticles with properties identical to the one at bench scale.

1.2. Well-controlled synthesis of nanoparticles

Amphiphilic molecules such as block copolymers and lipids can self-assemble into nanoparticles when they experience a change in solvent quality (e.g. from organic solvent to aqueous) (Figure 1.2a). A common and flexible way to accomplish a change in solvent quality is

by mixing the solvent with the anti-solvent, where mixing time directly influences the final size and size distribution of the nanoparticles formed¹⁶. If the mixing timescale, t_{mix} , is longer than the characteristic timescale for chains to nucleate and grow (t_{agg} , ~ 10 - 100 ms depending on the molecular weight of the chain), the nanoparticles begin to assemble under varying degrees of solvent quality. This heterogeneous environment prevents effective stabilization of the nanoparticles by the hydrophilic portion of the amphiphilic molecule and facilitates their aggregation, leading to the formation of larger, polydisperse nanoparticles. However, if $t_{\text{mix}} < t_{\text{agg}}$, particle self-assembly occurs primarily when the solvent change is complete, which presents a homogeneous environment for nanoparticle assembly and facilitates effective stabilization of the nanoparticles by the hydrophilic portion of the molecule, yielding smaller nanoparticles with uniform size¹⁷. While conventional bulk mixing occurs at the timescale of seconds, in microfluidic devices the mixing time of solvents is controllable and tunable from millisecond to microsecond scale (reaching $t_{\text{mix}} < t_{\text{agg}}$)^{16, 18}.

In recent years, several microfluidic systems that enable rapid mixing without the need of external actuators such as stirrers or electric fields have been developed¹⁹. The most widely used include flow focusing mixers²⁰, droplet mixers²¹, and those with micromixing structures embedded inside the channel²². Flow focusing squeezes the solvent stream between two anti-solvent streams, resulting in rapid solvent exchange via diffusion (Figure 1.2b). Droplets and 3D microchannel geometries result in complex folding of fluid flows, which can completely mix two or more streams within milliseconds (Figure 1.2b). The implementation of these mixing techniques for the formation of organic nanoparticles in continuous flow has resulted in polymeric and lipid nanoparticles with tunable nanoparticle size, narrower size distribution,

higher drug loadings, and greater batch-to-batch reproducibility relative to those made with conventional bulk techniques²³ (Figure 1.2c).

Similarly, inorganic nanoparticles comprised of transition metals such as gold, iron, and cadmium, among others, undergo a self-assembly where metal solutes nucleate, grow, and agglomerate into nanoclusters (Figure 1.2d)²⁴. Obtaining narrow particle size distribution requires rapid nucleation followed by growth of nanoparticles to the desired size in the absence of further nucleation, which can be accomplished by controlling the mixing time of reagents, reaction temperature, and reaction time²⁵. In bulk, these parameters are difficult to control, leading to uneven mixing, local temperature fluctuations, and uncontrolled reaction times²⁵. In contrast, microfluidic devices allow for control over the mixing time by varying solvent flow rates or channel geometry. Moreover, better heat transfer due to large surface areas enables better temperature control, preventing the formation of large temperature gradients. Finally, since the channel length directly corresponds to the time spent by the reactants flowing through it in continuous flow synthesis, the reaction time can be controlled by tuning the channel length or by adding reagents at precise downstream locations during the particle formation process to quench the reaction²⁶.

Two-phase droplet mixers where reagents are encapsulated in droplets and separated by inert fluids are commonly used for the synthesis of inorganic nanoparticles (Figure 1.2e)²⁷. In this configuration, rapid mixing of the solutions occur inside the droplets, which serve as identical microscale reactors providing homogeneous conditions for nanoparticle nucleation and growth. Both droplet-based and single-phase systems have been used to synthesize quantum dots exhibiting narrow size distributions that translates into sharper absorption peaks and better luminescence qualities²⁷, and with control over size to tune the absorption spectra (Figure 1.2f)²⁸.

Finally, similar systems have been implemented in the controlled synthesis of gold nanoparticles of defined size and shape, iron oxide nanoparticles with higher magnetization, and QDs with controlled size and biocompatible coatings²⁹.

Over the past four years, several examples showing the use of microfluidics for the synthesis of nanoparticles with different size, shape and surface compositions have emerged³⁰. Currently, there are microfluidic systems capable of characterizing the nanoparticle size and stability following synthesis in a single platform^{31, 32}. Moreover, large numbers of distinct nanoparticles can be obtained through combinatorial synthesis³³, and production rates of identical nanoparticles can be increased through parallelization of the devices^{34, 35}. Similar to high-throughput synthesis of libraries of small molecules, these advantages could potentially enable screening and optimization of libraries of nanoparticles with distinct properties. One of the challenges in gene therapy, for example, is finding the right formulation for delivering nucleic acids to specific sites in the body. By mixing different precursors at varying ratios, microfluidics systems have enabled a one-step combinatorial synthesis of libraries of polymeric and lipid nanoparticles that encapsulate DNA and siRNA, respectively. Screening these libraries of nanoparticles has helped identify superior formulations for gene transfection compared to conventional transfection agents such as lipofectamine 2000. Furthermore, using this method, potent lipid-based siRNA formulations for in vivo delivery to the liver have also been discovered^{33, 34}.

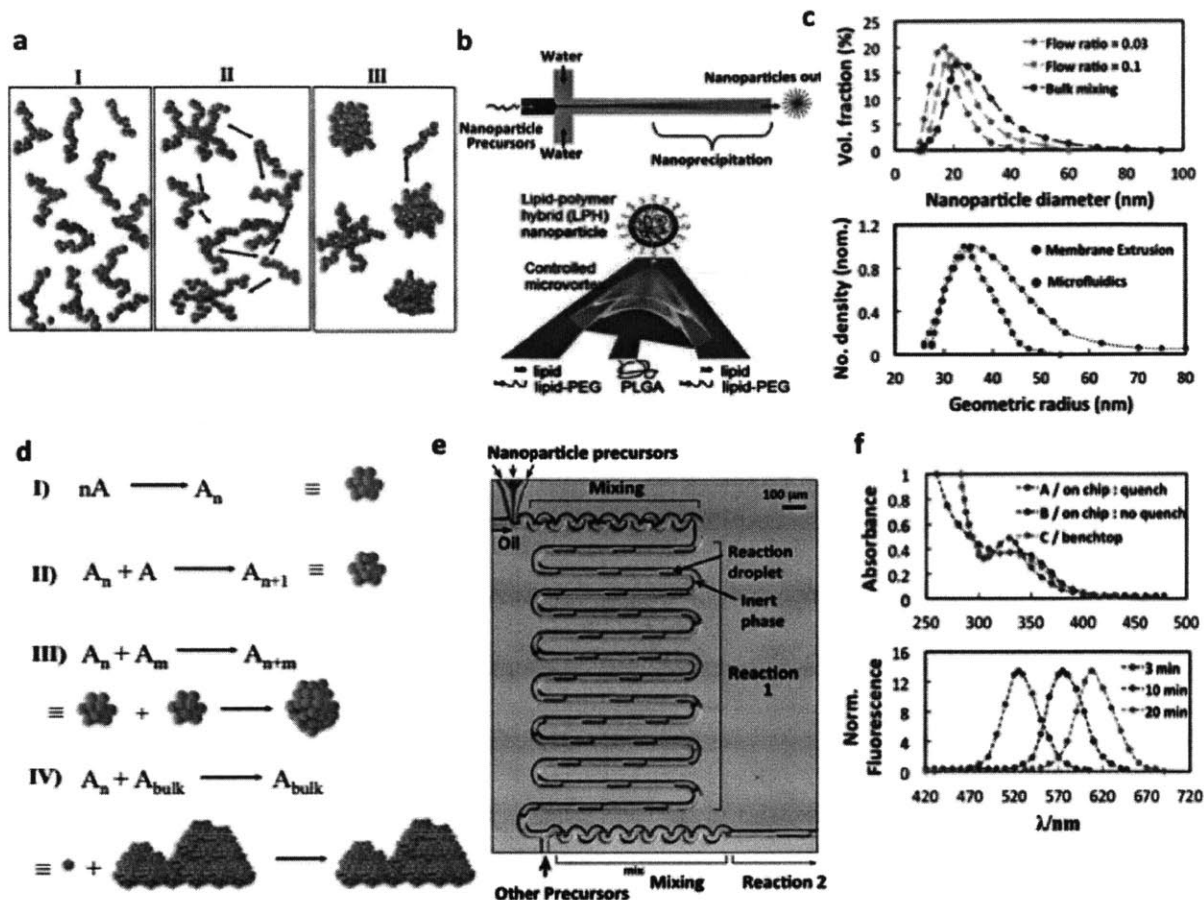


Figure 1.2. Microfluidic synthesis of nanoparticles.

(a) Schematic of the self-assembly mechanism of organic nanoparticles¹⁶. Upon mixing with anti-solvent, polymers (or lipids) are brought to the vicinity of each other (I) then nucleate (II), subsequently aggregating into nanoparticles (III) (b) Schematic of microfluidic synthesis of organic nanoparticles by rapid mixing through hydrodynamic flow focusing¹⁸ (top) and microvortices³⁵ (bottom). Red and dark blue indicate organic and aqueous streams, respectively, while pink and light blue indicate their degree of mixing. (c) Size distribution of polymeric nanoparticles (top) and liposomes (bottom) prepared in microfluidics compared to bulk synthesis^{18, 23}. In both cases narrower particle size distribution were produced through microfluidics. (d) Schematic of the self-assembly mechanism of inorganic nanoparticles²⁴. Individual molecules first nucleate (I and II), followed by aggregation of nuclei into nanoparticles (III). If the reaction is not quenched or stabilized, nanoparticles tend to agglomerate into bulk material (IV). A refers to individual molecules forming the nanoparticle, and A_n and A_m refer to nuclei formed of n and m number of A molecules, respectively. (e) Microfluidic synthesis of inorganic nanoparticles by rapid mixing through two-phase flow where reagents are embedded in fluid droplets carried by an inert fluid²⁷. (f) Sharp versus broad absorption maximum of QDs synthesized in microchannels and bulk, respectively (top); control in the absorption spectra of QDs as function of reaction time^{27, 28} (bottom).

1.3. Evaluation and screening of nanoparticles

Another challenge in nanoparticle development is the lack of *in vitro* models capable of predicting *in vivo* behavior³⁶. Conventionally, nanoparticles are evaluated *in vitro* using cells cultured in well plates, which does not capture the complexity of nanoparticle-cell interactions *in vivo*. For instance, a recent study showed that sedimentation of gold nanoparticles in well plates could lead to misinterpretation of results such as increased nanoparticle uptake³⁷. Microfluidics provides significant advantages over conventional methods for cell and tissue culture by displaying structures and networks at relevant physiological length scales, and by incorporating fluid flow and mechanical forces that bring the cell-based assays a step closer to mimicking the *in vivo* microenvironment³⁸ (Figure 1.3a). This is especially advantageous, for instance, when investigating the toxic effects related to the cell uptake of nanoparticles. A recently developed microfluidic system for evaluating QD toxicity on mouse fibroblasts revealed increased cell viability under flow conditions compared to static incubation, possibly due to the absence of QD sedimentation³⁹.

Recently, researchers have focused on developing biomimetic microfluidic technologies capable of portraying organ-level functions on a chip, such as those observed in the lung, liver, and kidneys, among others^{38, 40}. For instance, microfluidic systems that reconstitute the critical functional alveolar-capillary liquid-air interface of the human lung have been recently fabricated by growing alveolar epithelial cells and microvascular endothelial cells on different sides of a perforated silicone membrane. The membrane was pneumatically actuated to mimic the physiological expansion-contraction motion due to breathing. It was found that cyclic mechanical strain accentuates toxic and inflammatory responses in the lung when exposed to silica nanoparticles, which could have not been observed with other conventional *in vitro*

systems⁴¹ (Figure 1.3b). Using a similar design approach, a “gut-on-a-chip” was developed by coating both sides of a membrane separating two microfluidic devices with extracellular matrix and lined by human intestinal epithelial cells. It was demonstrated that by subjecting the membrane to flow and cyclic strains similar to those encountered in the gut, villi-like structures were formed and the co-culture of the intestinal microbes was made possible⁴² (Figure 1.3c).

Expansion of these technologies to other organs, for instance “liver-on-a-chip”⁴³, could lead to platforms for evaluating and screening nanoparticle toxicity in organs where nanoparticles tend to accumulate and toxicity is likely to be a major concern (e.g. liver, spleen and kidney). While nanoparticles would still need to be evaluated in animals, such microfluidic systems could take *in vitro* nanoparticle screening to a new level of utility by selecting promising candidates with higher probabilities of success from a large pool of nanoparticle formulations and eliminating those that would otherwise have failed in larger animal studies. In addition, coupling these technologies with microfluidic devices used for nanoparticle synthesis opens the possibility of rapid combinatorial screening of a large number of different nanoparticles under various conditions (e.g. concentrations, pH values, under the presence of specific proteins, etc.).

Nanoparticles exhibiting promising results *in vitro* are subsequently evaluated *in vivo*, which is considerably more expensive and resource-intensive, especially in non-human primates. While most of the parameters such as pharmacokinetics, biodistribution, and efficacy are evaluated in mice and larger animals, tracking physiological effects of nanoparticles on animal development could potentially be obtained using a large number of smaller organisms. The zebrafish and *C. elegans* worms are well-known models for studying fundamental mechanisms and progression of human diseases, and for drug screening⁴⁴. For example, the zebrafish was recently utilized as an *in vivo* model to develop a hazard ranking for engineered nanoparticles

based on their impact on mortality rate, and morphological defects in zebrafish embryos exposed to these materials⁴⁵. However, current methods for manipulating these organisms generally suffer from low throughput, low automation and imprecise delivery of external stimuli⁴⁶. To solve these challenges, engineered microfluidic systems with dimensions comparable to small organisms and containing valves and suction points have been developed. These systems enable precise manipulation of these organisms with respect to placement and orientation for high-throughput screening (Figure 1.3d)^{46,47}. Other microfluidic systems are being developed that are capable of imaging dynamic cellular processes in small organisms such as cell division and migration, degeneration, aging and regeneration⁴⁸. With such technologies in place, it might be possible to use real-time microscopy to track physiological responses to fluorescently labeled nanotherapeutics and nano-imaging agents as well as assess the distribution and efficacy of nanoparticles at both the organ and body level. In addition, real-time tracking of nanoparticle-induced toxicity at different concentrations and conditions in small organisms could enable rapid selection of nanoparticles (especially those made with novel synthetic materials) that are more likely to be non-toxic in larger animals.

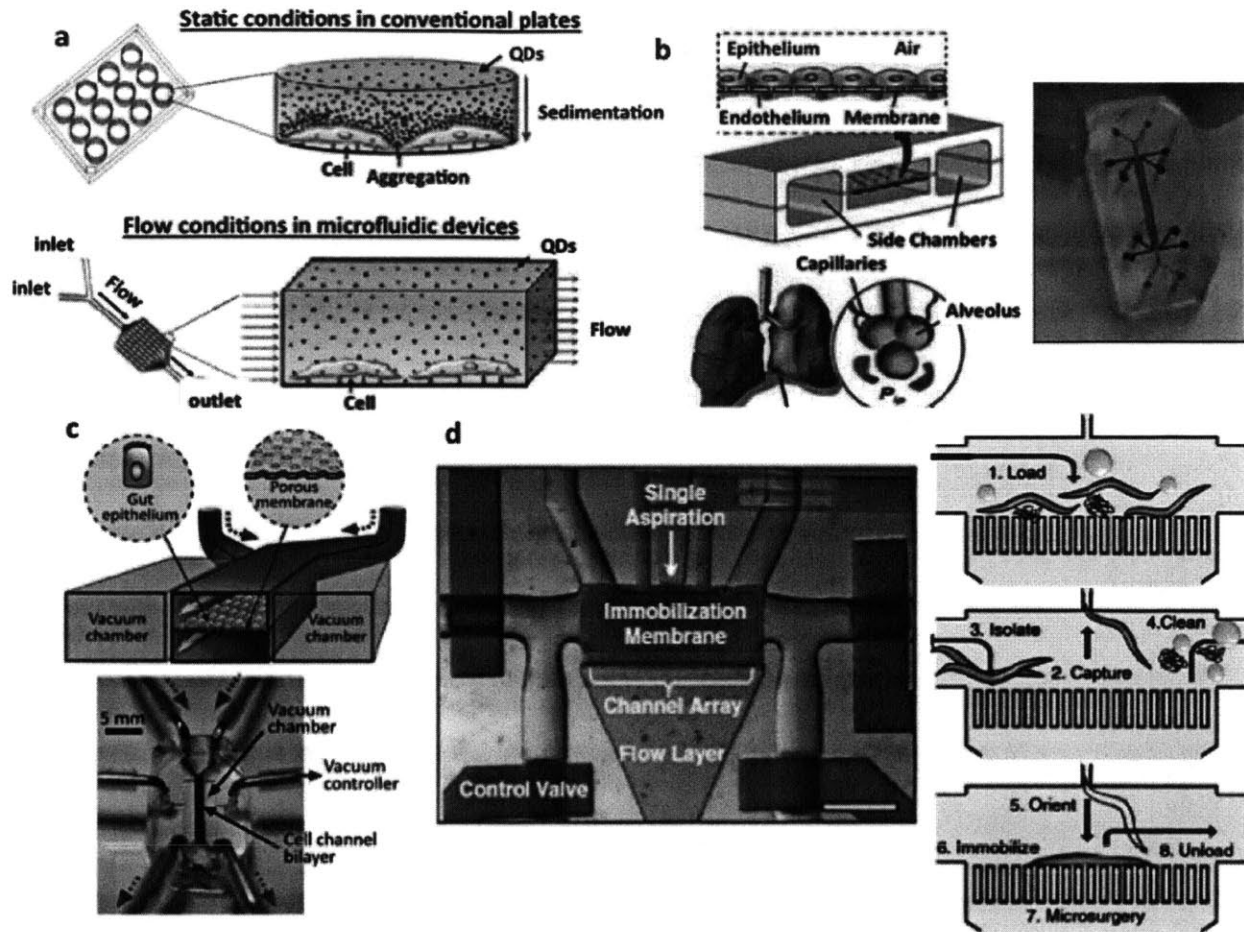


Figure 1.3. Microfluidic systems for *in vitro* evaluation and screening of nanoparticles. (a) Schematic of nanoparticle sedimentation in conventional plates, which could result in misinterpretation of results. In contrast, flow conditions in microfluidics provide a more accurate method for evaluating nanoparticles *in vitro*³⁹. (b) Schematic of the lung-on-a-chip that reconstitutes the critical functional alveolar-capillary interface of the human lung through a stretchable membrane containing an epithelium layer on one side and an endothelium layer on the other⁴¹ (left). Photograph of actual device (right). (c) Schematic of the gut-on-a-chip made by flexible, porous, ECM-coated membrane lined by gut epithelial cells⁴² (top). A photograph of the gut-on-a-chip device made of PDMS elastomer (bottom). A syringe pump was used to perfuse dyes for channel visualization. (d) Photograph of a dye-filled microfluidic system designed to handle *C. Elegans* worms⁴⁸ (left). Red, control valve layer; yellow, flow layer; blue, immobilization layer. Scale bar: 1 mm. Schematic showing load, capture, orient, immobilization and unload of the worm (right).

1.4. Future prospects

Today, the field of microfluidics applied to nanomedicine is still in its infancy. Although nanoparticles at present have a relatively small footprint in the pharmaceutical industry, it is anticipated that as these products bring in revenue, industry-led research and development efforts would likely adopt technologies, such as microfluidics, to accelerate their development. Nevertheless, microfluidic technologies, such as organ-on-a-chip and small animal screening, are likely to be adopted first for the screening of small molecule drug candidates, where the need for such tools is evident.

There are a few key directions at the intersection of microfluidics and nanomedicine that are likely to be pursued in the near future (Table 1). While the quantity of nanoparticles synthesized by microfluidic devices is often in the microgram-milligram range, parallel and stackable microfluidic systems could produce gram to kilogram scale of nanoparticles continuously with the same properties as those prepared at the bench scale. Similarly, the use of microfluidic platform technologies to reproducibly synthesize and screen libraries of nanoparticles with different chemical compositions and/or physicochemical properties could potentially advance nanoparticle discovery analogously to how the high-throughput screening of small molecules in medicinal chemistry advanced small molecule discovery. With respect to the design and development of novel nanoparticle constructs, the use of microfluidics could enable the synthesis of nanoparticles with properties not accessible by conventional synthesis similar to what has already occurred for microparticle synthesis⁴⁹. Another avenue of future research will be the integration of different steps of nanoparticle development into a single system (e.g. nanoparticle synthesis characterization, and evaluation), together with feedback control through a combination of microfluidics, robotics, and automation, thus significantly cutting the time and

cost of nanoparticle development. Finally, mass-produced microfluidic devices and well-defined nanoparticle precursors can aid in the synthesis of identical batches of nanoparticles with little to no variations introduced by user handling. This could lead to the use and commercialization of “nanoparticle synthesis kits” composed of calibrated devices that can reproducibly synthesize a specific class of nanoparticle with well-defined properties for use as standards in conventional toxicological assays. Considering the large number of nanoparticles being made of novel synthetic materials or of unusual shapes, such standardization would be highly useful for regulatory purposes, among others.

Microfluidic technologies are capable of accelerating the discovery and translation of nanoparticles, and could serve as a tool for nanotherapeutics to reach a similar “tipping point” reached by genome sequencing in the past decade after high-throughput sequencing technologies were developed⁵⁰. Among all the microfluidic technologies, those developed for synthesis and *in vitro* screening of nanoparticles have the highest probability of making an impact in the near future (Table 1). Specifically, microfluidic synthesis may be adopted as a second generation manufacturing technology after initial success of FDA-approved nanoparticles in cases where the advantages of microfluidic synthesis are significant. Microfluidic synthesis may also be adopted as a screening tool to identify optimal nanoparticles in academic and industrial research laboratories. Alternatively, the impact of microfluidics might be observable in the medium- to long-term future for nanoparticle characterization and *in vivo* evaluation. For nanoparticle characterization, the use of microfluidics would likely increase once more advanced technologies are developed to characterize several nanoparticle properties (e.g. size, charge, surface composition, and stability) in a single system. Similarly, *in vivo* evaluation of nanoparticles in microfluidics would likely mature once both easily adoptable microfluidic systems for

manipulating small organisms and methods for translating data obtained from these organisms to larger animals are developed.

Overall, the use of microfluidic technologies in nanomedicine brings exciting opportunities to expand the body of knowledge in the field, advance the clinical translation of nano-based therapeutics and imaging agents, and demonstrate innovative ways to develop other classes of drugs.

Table 1: Advantages, disadvantages/challenges, stage of development, and potential impact of microfluidic systems on different steps in the clinical translation of nanoparticles.

	Advantages	Disadvantages/Challenges	Stage of Development	Potential impact
Synthesis	<ul style="list-style-type: none"> • Tunable nanoparticle size. • Narrower size distribution. • Reproducible synthesis. • Potential for high-throughput synthesis and optimization of nanoparticles. 	<ul style="list-style-type: none"> • Solvent and high temperature incompatibility to low-cost PDMS microchannels. • Higher costs and complexities in the fabrication of glass and silicon microdevices. 	*****	Rapid combinatorial, controlled and reproducible synthesis of libraries of distinct nanoparticles for a specific application, and/or reference nanoparticles for toxicology studies.
Characterization	<ul style="list-style-type: none"> • Label-free characterization. • Potential for feedback control and real-time nanoparticle optimization. 	<ul style="list-style-type: none"> • Current methods are not applicable to all classes of nanoparticles. • Not all properties can be characterized, such as drug encapsulation and release, and signal-to-noise ratio. 	*	In-line rapid characterization and optimization of nanoparticles.
In vitro	<ul style="list-style-type: none"> • Biological conditions closer to in vivo microenvironments. • Potential for high-throughput screening of large number of nanoparticles at different concentrations. 	<ul style="list-style-type: none"> • Higher costs and complexities in the fabrication and operation compared to well plates. • Might not be reusable and if reusable, it would be difficult to maintain sterile. 	****	High-throughput studies of nanoparticle toxicity, efficacy, tumor penetration, organ distribution, using in organ-on-a-chip systems
In vivo	<ul style="list-style-type: none"> • Large number organisms could be used for a single measurement. • High-throughput evaluation of toxicity for a large number of nanoparticles. 	<ul style="list-style-type: none"> • Lack of methods to translate data from small-scale organisms to other species. • Pharmacokinetics or biodistribution cannot be determined. 	**	Real-time tracking of the distribution or toxicity of nanoparticles on small-scale organisms.
Large-scale synthesis	<ul style="list-style-type: none"> • Continuous synthesis • Bench-scale to clinical-scale reproducibility. • Parallelization allows for tuning scale of production. 	<ul style="list-style-type: none"> • Difficult to build systems at low-cost comparable to a batch reactor able to prepare grams or kilograms of nanoparticles. 	***	Synthesis of nanoparticles for human administration using stackable parallel microfluidic units.

Rank: Most advanced in development (*****) to least advanced in development (*), based on the amount of research carried out on each category as well as the potential ease of adoption by industry.

1.5. References

1. Petros, R. A.; DeSimone, J. M., Strategies in the design of nanoparticles for therapeutic applications. *Nat Rev Drug Discov* **2010**, *9* (8), 615-27.
2. Gregoriadis, G., Drug entrapment in liposomes. *FEBS Lett* **1973**, *36* (3), 292-6.
3. Hrkach, J.; Von Hoff, D.; Ali, M.; Andrianova, E.; Auer, J.; Campbell, T.; de Witt, D.; Figa, M.; Figueiredo, M.; Horhota, A.; Low, S.; McDonell, K.; Peeke, E.; Retnarajan, B.; Sabnis, A.; Schnipper, E.; Song, J.; Song, Y. H.; Summa, J.; Tompsett, D.; Troiano, G.; van Geen, T.; Wright, J.; LoRusso, P.; Kantoff, P. W.; Bander, N. H.; Sweeney, C. J.; Farokhzad, O. C.; Langer, R.; Zale, S., Preclinical Development and Clinical Translation of a PSMA-Targeted Docetaxel Nanoparticle with a Differentiated Pharmacological Profile. *Sci Transl Med* **2012**, *4*.

4. Qiao, R.; Yang, C.; Gao, M., Superparamagnetic iron oxide nanoparticles: from preparations to in vivo MRI applications. *J. Mater. Chem.* **2009**, *19*, 6274-6293.
5. Haun, J. B.; Castro, C. M.; Wang, R.; Peterson, V. M.; Marinelli, B. S.; Lee, H.; Weissleder, R., Micro-NMR for rapid molecular analysis of human tumor samples. *Sci Transl Med* **2011**, *3* (71), 71ra16.
6. Kim, B. Y.; Rutka, J. T.; Chan, W. C., Nanomedicine. *N Engl J Med* **2010**, *363* (25), 2434-43.
7. Kamaly, N.; Xiao, Z.; Valencia, P. M.; Radovic-Moreno, A. F.; Farokhzad, O. C., Targeted polymeric therapeutic nanoparticles: design, development and clinical translation. *Chem Soc Rev* **2012**, *41* (7), 2971-3010.
8. Peer, D.; Karp, J. M.; Hong, S.; Farokhzad, O. C.; Margalit, R.; Langer, R., Nanocarriers as an emerging platform for cancer therapy. *Nat Nanotechnol* **2007**, *2* (12), 751-60.
9. Barreto, J. A.; O'Malley, W.; Kubeil, M.; Graham, B.; Stephan, H.; Spiccia, L., Nanomaterials: applications in cancer imaging and therapy. *Adv Mater* **2011**, *23* (12), H18-40.
10. Shi, J.; Xiao, Z.; Kamaly, N.; Farokhzad, O. C., Self-assembled targeted nanoparticles: evolution of technologies and bench to bedside translation. *Acc Chem Res* **2011**, *44* (10), 1123-34.
11. Murday, J. S.; Siegel, R. W.; Stein, J.; Wright, J. F., Translational nanomedicine: status assessment and opportunities. *Nanomedicine* **2009**, *5* (3), 251-73.
12. Chou, L. Y.; Ming, K.; Chan, W. C., Strategies for the intracellular delivery of nanoparticles. *Chem Soc Rev* **2011**, *40* (1), 233-45.
13. Nel, A. E.; Madler, L.; Velegol, D.; Xia, T.; Hoek, E. M.; Somasundaran, P.; Klaessig, F.; Castranova, V.; Thompson, M., Understanding biophysicochemical interactions at the nano-bio interface. *Nat Mater* **2009**, *8* (7), 543-57.
14. Whitesides, G. M., The origins and the future of microfluidics. *Nature* **2006**, *442* (7101), 368-73.
15. DeMello, A. J., Control and detection of chemical reactions in microfluidic systems. *Nature* **2006**, *442* (7101), 394-402.
16. Johnson, B. K.; Prud'homme, R. K., Mechanism for rapid self-assembly of block copolymer nanoparticles. *Phys Rev Lett* **2003**, *91* (11), 118302.
17. Chen, T.; Hynninen, A. P.; Prud'homme, R. K.; Kevrekidis, I. G.; Panagiotopoulos, A. Z., Coarse-grained simulations of rapid assembly kinetics for polystyrene-b-poly(ethylene oxide) copolymers in aqueous solutions. *J Phys Chem B* **2008**, *112* (51), 16357-66.
18. Karnik, R.; Gu, F.; Basto, P.; Cannizzaro, C.; Dean, L.; Kyei-Manu, W.; Langer, R.; Farokhzad, O. C., Microfluidic platform for controlled synthesis of polymeric nanoparticles. *Nano Lett* **2008**, *8* (9), 2906-12.
19. Capretto, L.; Cheng, W.; Hill, M.; Zhang, X., Micromixing within microfluidic devices. *Top Curr Chem* **2011**, *304*, 27-68.
20. Rhee, M.; Valencia, P. M.; Rodriguez, M. I.; Langer, R.; Farokhzad, O. C.; Karnik, R., Synthesis of size-tunable polymeric nanoparticles enabled by 3D hydrodynamic flow focusing in single-layer microchannels. *Adv Mater* **2011**, *23* (12), H79-83.
21. Liu, K.; Wang, H.; Chen, K. J.; Guo, F.; Lin, W. Y.; Chen, Y. C.; Phung, D. L.; Tseng, H. R.; Shen, C. K., A digital microfluidic droplet generator produces self-assembled supramolecular nanoparticles for targeted cell imaging. *Nanotechnology* **2010**, *21* (44), 445603.

22. Valencia, P. M.; Basto, P. A.; Zhang, L.; Rhee, M.; Langer, R.; Farokhzad, O. C.; Karnik, R., Single-step assembly of homogenous lipid-polymeric and lipid-quantum dot nanoparticles enabled by microfluidic rapid mixing. *ACS Nano* **2010**, *4* (3), 1671-9.
23. Jahn, A.; Reiner, J. E.; Vreeland, W. N.; DeVoe, D. L.; Locascio, L. E.; Gaitan, M., Preparation of nanoparticles by continuous-flow microfluidics. *Journal of Nanoparticle Research* **2008**, *10* (6), 925-934.
24. Besson, C.; Finney, E. E.; Finke, R. G., A mechanism for transition-metal nanoparticle self-assembly. *J Am Chem Soc* **2005**, *127* (22), 8179-84.
25. Song, Y.; Hormes, J.; Kumar, C. S., Microfluidic synthesis of nanomaterials. *Small* **2008**, *4* (6), 698-711.
26. Gu, F. X.; Karnik, R.; Wang, A. Z.; Alexis, F.; Levy-Nissenbaum, E.; Hong, S.; Langer, R. S.; Farokhzad, O. C., Targeted nanoparticles for cancer therapy. *Nano Today* **2007**, *2* (3), 14-21.
27. Shestopalov, I.; Tice, J. D.; Ismagilov, R. F., Multi-step synthesis of nanoparticles performed on millisecond time scale in a microfluidic droplet-based system. *Lab Chip* **2004**, *4* (4), 316-21.
28. Kikkeri, R.; Laurino, P.; Odedra, A.; Seeberger, P. H., Synthesis of carbohydrate-functionalized quantum dots in microreactors. *Angew Chem Int Ed Engl* **2010**, *49* (11), 2054-7.
29. Marre, S.; Jensen, K. F., Synthesis of micro and nanostructures in microfluidic systems. *Chem Soc Rev* **2010**, *39* (3), 1183-202.
30. Zhao, C. X.; He, L. Z.; Qiao, S. Z.; Middelberg, A. P. J., Nanoparticle synthesis in microreactors. *Chem Eng Sci* **2011**, *66* (7), 1463-1479.
31. Fraikin, J. L.; Teesalu, T.; McKenney, C. M.; Ruoslahti, E.; Cleland, A. N., A high-throughput label-free nanoparticle analyser. *Nat Nanotechnol* **2011**, *6* (5), 308-13.
32. Birnbaumer, G.; Kupcu, S.; Jungreuthmayer, C.; Richter, L.; Vorauer-Uhl, K.; Wagner, A.; Valenta, C.; Sleytr, U.; Ertl, P., Rapid liposome quality assessment using a lab-on-a-chip. *Lab Chip* **2011**, *11* (16), 2753-62.
33. Wang, H.; Liu, K.; Chen, K. J.; Lu, Y.; Wang, S.; Lin, W. Y.; Guo, F.; Kamei, K.; Chen, Y. C.; Ohashi, M.; Wang, M.; Garcia, M. A.; Zhao, X. Z.; Shen, C. K.; Tseng, H. R., A rapid pathway toward a superb gene delivery system: programming structural and functional diversity into a supramolecular nanoparticle library. *ACS Nano* **2010**, *4* (10), 6235-43.
34. Chen, D.; Love, K. T.; Chen, Y.; Eltoukhy, A. A.; Kastrop, C. J.; Sahay, G.; Jeon, A.; Dong, Y.; Whitehead, K. A.; Anderson, D. G., Rapid Discovery of Potent siRNA-Lipid-Nanoparticles Enabled by Controlled Microfluidic Formulation. *J Am Chem Soc* **2012**.
35. Kim, Y.; Lee Chung, B.; Ma, M.; Mulder, W. J.; Fayad, Z. A.; Farokhzad, O. C.; Langer, R., Mass Production and Size Control of Lipid-Polymer Hybrid Nanoparticles through Controlled Microvortices. *Nano Lett* **2012**, *12* (7), 3587-91.
36. Dobrovolskaia, M. A.; Germolec, D. R.; Weaver, J. L., Evaluation of nanoparticle immunotoxicity. *Nat Nanotechnol* **2009**, *4* (7), 411-4.
37. Cho, E. C.; Zhang, Q.; Xia, Y., The effect of sedimentation and diffusion on cellular uptake of gold nanoparticles. *Nat Nanotechnol* **2011**, *6* (6), 385-91.
38. Ziolkowska, K.; Kwapiszewski, R.; Brzozka, Z., Microfluidic devices as tools for mimicking the in vivo environment. *New J Chem* **2011**, *35* (5), 979-990.
39. Mahto, S. K.; Yoon, T. H.; Rhee, S. W., A new perspective on in vitro assessment method for evaluating quantum dot toxicity by using microfluidics technology. *Biomicrofluidics* **2010**, *4* (3).

40. Huh, D.; Torisawa, Y. S.; Hamilton, G. A.; Kim, H. J.; Ingber, D. E., Microengineered physiological biomimicry: Organs-on-Chips. *Lab Chip* **2012**, *12* (12), 2156-64.
41. Huh, D.; Matthews, B. D.; Mammoto, A.; Montoya-Zavala, M.; Hsin, H. Y.; Ingber, D. E., Reconstituting organ-level lung functions on a chip. *Science* **2010**, *328* (5986), 1662-8.
42. Kim, H. J.; Huh, D.; Hamilton, G.; Ingber, D. E., Human gut-on-a-chip inhabited by microbial flora that experiences intestinal peristalsis-like motions and flow. *Lab on a Chip* **2012**, *12* (12), 2165-2174.
43. Toh, Y. C.; Lim, T. C.; Tai, D.; Xiao, G.; van Noort, D.; Yu, H., A microfluidic 3D hepatocyte chip for drug toxicity testing. *Lab Chip* **2009**, *9* (14), 2026-35.
44. Crane, M. M.; Chung, K.; Stirman, J.; Lu, H., Microfluidics-enabled phenotyping, imaging, and screening of multicellular organisms. *Lab Chip* **2010**, *10* (12), 1509-17.
45. George, S.; Xia, T.; Rallo, R.; Zhao, Y.; Ji, Z.; Lin, S.; Wang, X.; Zhang, H.; France, B.; Schoenfeld, D.; Damoiseaux, R.; Liu, R.; Bradley, K. A.; Cohen, Y.; Nel, A. E., Use of a high-throughput screening approach coupled with in vivo zebrafish embryo screening to develop hazard ranking for engineered nanomaterials. *ACS Nano* **2011**, *5* (3), 1805-17.
46. Shi, W.; Wen, H.; Lin, B.; Qin, J., Microfluidic Platform for the Study of *Caenorhabditis elegans*. *Top Curr Chem* **2011**, *304*, 323-38.
47. Baker, M., Screening: the age of fishes. *Nat Methods* **2011**, *8* (1), 47-51.
48. Samara, C.; Rohde, C. B.; Gilleland, C. L.; Norton, S.; Haggarty, S. J.; Yanik, M. F., Large-scale in vivo femtosecond laser neurosurgery screen reveals small-molecule enhancer of regeneration. *Proc Natl Acad Sci U S A* **2010**, *107* (43), 18342-7.
49. Dendukuri, D.; Doyle, P. S., The Synthesis and Assembly of Polymeric Microparticles Using Microfluidics. *Adv Mater* **2009**, *21*, 4071-4086.
50. Zhao, J.; Grant, S. F., Advances in whole genome sequencing technology. *Curr Pharm Biotechnol* **2011**, *12* (2), 293-305.

Chapter 2 - Microfluidic System for Synthesis of Multifunctional Nanoparticles: 2D Flow Focusing with Tesla Structures

2.1. Introduction

The development of smart multifunctional targeted nanoparticles (NPs) that can deliver drugs at a sustained rate to specific cells and carry nanoscale imaging agents may provide better efficacy, lower toxicity, and enhanced prognosis for treatment of multiple diseases¹⁻⁴. Two promising families of NPs that can encapsulate and deliver therapeutic agents are polymeric NPs and liposomes.^{1,2} Biocompatibility, biodegradability, reduced toxicity, and capacity for size and surface manipulations are benefits that these NPs offer in comparison to other delivery systems. Recently, it has been shown that hybrid lipid-polymeric NPs combine the desirable characteristics of polymeric NPs and liposomes such as high drug encapsulation yield, slow drug release, and high serum stability.^{3, 4} In addition, temporal controlled release of two different therapeutic agents has been achieved with these hybrid NPs by entrapping one agent in the lipid envelope and the other one in the polymeric core.⁵

The development of novel nanosystems such as hybrid lipid-polymeric NPs for drug delivery is necessary to advance the frontiers of drug delivery, but the ability to precisely control and predict properties of these systems is critical for their success in clinical translation.⁶ Furthermore, it may be necessary to screen and select NPs with optimal properties for a certain application, which demands reproducible synthesis of NPs with distinct size, charge, and ligand density.⁷ Among some of the technologies developed to prepare polymeric and lipid NPs of well-defined properties, continuous-flow microfluidic synthesis offers better control over NP formation compared to conventional synthesis and has the potential to tune NP characteristics in a reproducible manner, which is critical for identifying optimal NP formulations for any given application.⁸⁻¹¹ Continuous-flow microfluidics has been used to synthesize polymeric nano and microparticles using controlled emulsification,¹² and droplet formation through hydrodynamic flow focusing.^{13, 14} Recently, hydrodynamic flow focusing was used for the synthesis of liposomes with sizes of less than 200 nm^{15, 16}, and PLGA-PEG NPs by nanoprecipitation (also known as solvent-displacement method).⁹

However, conventional methods for synthesizing lipid-polymeric NPs are more complex as compared to the preparation of liposomes or polymeric NPs. These methods involve mixing of polymeric NPs with liposomes to form lipid-polymer complexes, in which a lipid bilayer or lipid multilayer fuses on the surface of polymeric NPs.¹⁷⁻¹⁹ These complexes usually require a two-step formulation process: (i) development of polymeric NPs, and (ii) encapsulation of polymeric NPs within liposomes, resulting in poor control over the final NP physicochemical structure. Recently, our group developed a single step bulk hybrid lipid NP preparation in which a solution of poly-(lactic-co-glycolic) acid (PLGA) in acetonitrile was added to an aqueous solution of lecithin and 1,2-distearoyl-*sn*-glycero-3-phosphoethanolamine-N-

[carboxy(polyethylene glycol)] (DSPE-PEG) resulting in the formation of hybrid lipid-polymeric NPs.^{3, 4} Although this preparation yields sub-100 nm NPs and simplifies the synthesis, intermediate steps such as heating, vortexing, and long incubation time does not make the process easily amenable to combinatorial synthesis and can introduce variability in the properties of the NPs. A single-step process for reproducible synthesis of hybrid lipid-polymer NPs would enable preparation of libraries of NPs with distinct properties and allow for identification of optimal NP properties for different applications.

In this work, we show that rapid mixing of polymer and lipid solutions using continuous-flow microfluidics results in core-shell lipid-polymeric NPs in a single-step nanoprecipitation process. These NPs are composed of PLGA, lecithin and DSPE-PEG. We investigated the conditions under which stable hybrid NPs were formed and showed that by simply changing the precursors, NPs with tunable size from 35-180 nm and tunable zeta potential from -20 to 10 mV in PBS could be synthesized. Using the same microfluidic platform, we prepared homogenous lipid-QD NPs composed of CdSe/ZnS QDs coated by a lecithin and DSPE-PEG layer for potential imaging applications. Simplicity and reproducibility make this technology suitable for the combinatorial synthesis and screening of NPs with different properties without resorting to labor-intensive processing.

2.1. Microfluidic device and nanoparticle design.

Controlled nanoprecipitation of NPs can be obtained by minimizing the mixing time to ensure homogeneous environment for nucleation and growth of the NPs.²⁰ One way to decrease mixing time in microchannels is the use of micromixing structures, such as serpentine, staggered-herringbone, and zig-zag structures.²¹ Here we used an in-plane micromixing structure

called Tesla mixer²² that operates at Reynolds numbers greater than 20. These micromixing structures show contributions from both diffusion and convection at high flow rates.

Figure 2.1a shows a schematic of the microchannel used to synthesize the hybrid lipid-polymeric NPs. An aqueous solution composed of lecithin and DSPE-PEG (lecithin:DSPE-PEG, 8.4:1.6 by mol) was mixed with an organic solution of PLGA dissolved in acetonitrile (1 mg/mL) at a volume ratio of 10:1. At the junction of the streams, the organic stream is hydrodynamically focused and enhanced mixing occurs through the Tesla structures as the focused streams flows along the channel. The hybrid NPs generated have PLGA-lecithin-PEG core-shell structure and properties as those previously synthesized using bulk synthesis methods (Figure 1b)^{3,4}. TEM imaging allowed qualitative assessment of the product stream including its core-shell structure and monodispersity (Figure 2.1c). The average NP size is 40 nm and its size distribution by volume indicated that over 85% of the NPs have a size within 30-60 nm (Figure 2.1d). A fluorescent dye was used to observe the unfolding-folding flow pattern inside the micromixer and used to illustrate the degree of mixing within the channel (Figure 2.1e). From this image, observation of complete mixing at a total flow rate of 50 $\mu\text{L}/\text{min}$ occurs within the fourth turn of the Tesla mixer on a timescale of 10 ms (see supporting information for determination of mixing timescale in microchannel). This flow rate was fast enough to ensure good mixing in the Tesla mixer, yet low enough to limit the pressure drop in the device and hence prevent device failure.

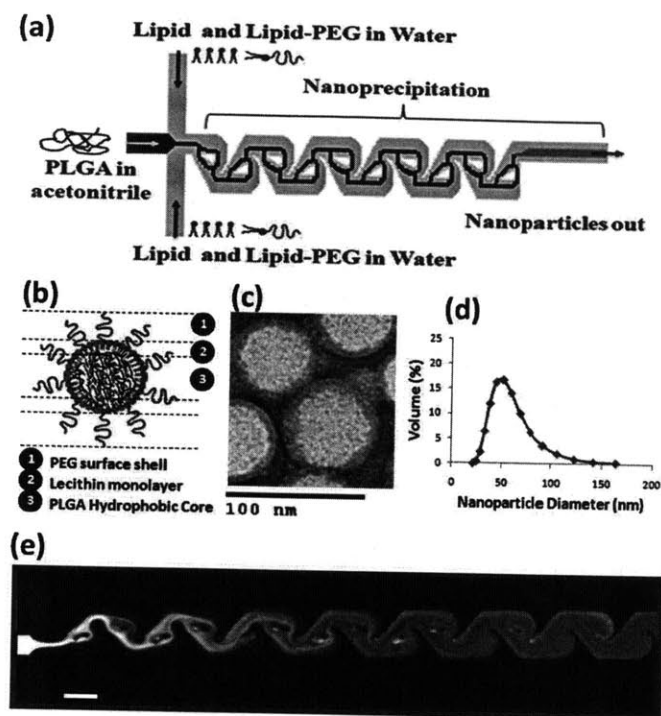


Figure 2.1. Nanoprecipitation of lipid-polymeric nanoparticles.

(a) A representative schematic of input and output streams within hybrid lipid-polymeric nanoparticle formation in microchannels with Tesla structures (b) Illustrative figure of microfluidic synthesized NP component layers (c) TEM image of uranyl acetate stained hybrid NPs after synthesis which highlights differences in density of the core versus near the surface of the NP potentially illustrating the lipid-PEG layer. Bar is labeled at 100 nm (d) Reproducible average size distribution of hybrid NPs generated through microfluidics. Average size is 40 nm. (e) Solvent mixing in the Tesla micromixing structures using fluorescent dye and water at 5 $\mu\text{L}/\text{min}$ and 50 $\mu\text{L}/\text{min}$, respectively, shows complete mixing at the fourth turn in the channel (scale bar: 100mm).

2.2. Characterization of PLGA-lipid NPs

The overall structure of the NPs synthesized was tested by multiple measures to ensure that they were hybrid particles of both lipid and polymeric nature rather than a combination of liposomes and unprotected PLGA NPs. Using different components in the input stream such as polymer alone, lipid/ lipid-PEG alone, or a combination of both illustrated differences in size of particles generated through the Tesla mixer (Figure 2.2a). When only polymer was present, NPs formed with a size of 40-50 nm and experienced slow aggregation within a few hours of

formation, resulting in sizes ranging from 50-100 nm. When only lipid and lipid-PEG were added in the input streams, NPs obtained had a much larger size (~250 nm) and wider size distribution, which is typical for liposomes. However, particles prepared with both polymer and lipid had a size of 40 nm that did not significantly change over a long period of time (see figure A2.2, appendix). This difference in size suggests that when both polymer and lipid are present in the input streams, polymeric NPs formed are stabilized by a lipid coating that helps maintain a size of 40 nm. Moreover, NPs generated with varying flow ratios of aqueous to organic stream did not appear to have a significant influence on the NP size (Figure 2.2a).

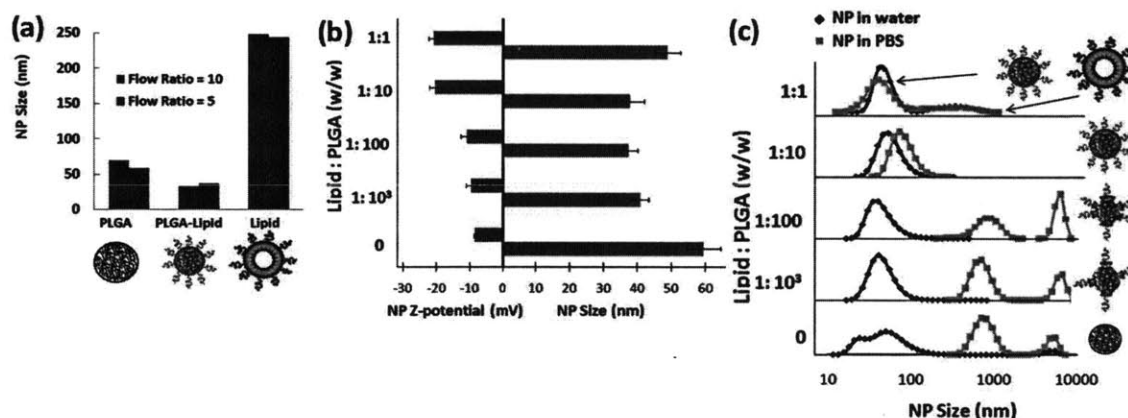


Figure 2.2. Characterization of Lipid-PLGA structure

(a) Comparison of average NP size from the product stream with aqueous : organic flow ratios of 10:1 and 5:1 respectively where the input organic stream is either PLGA, PLGA and lipid, or lipid alone. (b) Determination of lipid coverage of polymeric NPs. Zeta potential and size of NPs as the ratio of lipid to PLGA (w/w) is decreased. (c) Size distributions in water and PBS of NPs as the ratio of lipid to PLGA is changed. Complete lipid coverage of polymeric cores is observed at a ratio of lipid to PLGA ratio of 1:10. Above this ratio, the remaining lipid forms other nanostructures such as liposomes and below this ratio, NPs are not stable in PBS due to inadequate lipid coverage.

To investigate the optimal amount of lipid needed to obtain a stable hybrid NP that do not experience aggregation over time and under biological conditions, we first determined the extent

of lipid coverage through measurements of NP zeta potential. A hybrid NP completely covered by lipid and lipid-PEG-COOH had a zeta potential in PBS of approximately -20 mV while a NP without lipid and only PLGA-OCH₃ had a zeta potential of -8 mV (Figure 2.2b). Therefore, by decreasing the amount of lipid with respect to PLGA while keeping other conditions consistent, one may expect to see an increase in zeta potential as the NP goes from complete lipid coverage to no coverage. Variation of the amount of lipid to PLGA from 1:10 to 1:100 lead to an increase in zeta potential without a significant change in size (Figure 2.2b) which suggests that complete lipid surface coverage is not required to maintain NP size stability at 40 nm in water. In fact, a lipid to polymer ratio of 1:1000 was sufficient to prevent aggregation of the NPs. When lipid was absent, the size of the polymeric NP increased to that of PLGA NPs, similar to the trend observed in Figure 2.2a. The size increase in the case of 1:1 lipid to PLGA indicates that there is enough lipid to completely cover all PLGA NPs, and the excess lipid present results in an increase in the average NP size either by addition of layers, or by the formation of liposomes.

To confirm this hypothesis, we obtained the size distributions by volume of NPs in water as the amount of lipid introduced in the input stream was decreased. In addition, since PLGA NPs covered by lipid are stable in PBS as opposed to those without lipid coverage, we obtained the size distribution of the NPs in PBS as way to assay their stability (Figure 2.2c). Our studies indicate that two populations of particles are formed at a lipid to PLGA ratio of 1:1 with sizes at 40 nm and 250 nm. The smaller particles correspond to hybrid NPs with full lipid coverage while the larger particles correspond to liposomes similar to ones observed in Figure 2.1a. For a lipid to PLGA ratio of 1:10, a homogenous size distribution was observed in water and PBS. It must be noted that a small shift of the average NP size peak is observed when the samples were measured in water versus PBS. This peak shift could be explained by an aggregation of 2 or 3 NPs after

immersion in PBS and it can be controlled by tuning the ratio of lipid to lipid-PEG in the formulation (Figure S3, supporting information). For lipid to PLGA ratio of 1:100 and 1:1000, there is enough lipid present to keep the NP at size of 40 nm in water, yet it is not enough to avoid NPs aggregation in PBS. Our studies suggest that the optimal lipid coverage is obtained at a lipid to PLGA ratio of approximately 1:10. In fact, NPs prepared at this ratio were stable for a period of 24 hours in 10% BSA and 10% serum, which are surrogates for *in vivo* protein adsorption and biofouling (Appendix, figure A2.2).³ Considering the thickness and hydrodynamic radius of a lecithin layer with DSPE-PEG, estimation of the amount of lecithin and DSPE-PEG needed to completely cover NP core of 40 nm lead to a calculated ratio of 1.4:10 of lipid to PLGA. Although this calculation relies on several assumptions (*e.g.* all NPs are spheres and monodisperse, constant ratio of lecithin to DSPE-PEG, full lipid coverage on surface etc), it still offers an adequate approximation of the amount of lipid necessary to form a stable hybrid lipid-polymeric NP.

At the same lipid to PLGA ratio, we found that there was no significant difference in the size of NPs prepared at aqueous to organic flow ratios of 10:1 and 5:1 (see figure A1.1 in appendix). Larger flow ratios (*e.g.* 20:1, aqueous to organic) resulted in pulsing of the flow due to the syringe pumps, and required higher PLGA concentrations that made the device more susceptible to fouling. On the contrary, lower flow ratios (*e.g.* 1:1, aqueous to organic) would result in an inadequate environment for NP formation since for optimal nanoprecipitation a flow ratio of aqueous to acetonitrile streams at least 3:1 is desired.⁹ Therefore, all the NPs prepared in this work were obtained at a flow ratio of 10:1 or 5:1.

2.3. Control of NP physicochemical properties: Size and surface charge

After confirming the core-shell structure of the lipid-PLGA NPs, and knowing their range of optimal lipid coverage, we investigated the possibility of controlling the NP's physicochemical properties, mainly size and surface charge. Figure 2.3a illustrates a change in zeta potential of the lipid-polymeric NPs when different end-functional groups of DSPE-PEG were introduced in the input streams. The zeta potential of the NPs could be controlled from positive to neutral to negative charge by utilizing $-\text{COOH}$, $-\text{CH}_3$ and $-\text{NH}_2$ respectively, while the size remained essentially unchanged. Specific values for zeta potentials of different modified end groups agree with those previously published.²³ These results not only show that the surface charge of the NP can be finely tuned but they also confirm that lipid-PEG is on the surface of the polymeric core. Finally, NP size was controlled by varying the inherent viscosity of the polymer and the PLGA concentration while keeping other conditions such as organic and aqueous flow rates and flow ratio the same. Decrease in inherent viscosity and increase in initial polymer concentration lead to the generation of larger NPs as reported similarly in bulk synthesis of these particles (Figure 2.3b)⁴. This illustrates that hybrid NPs made from microfluidics are similar in nature to those made in bulk and their physicochemical properties such as size and charge can be controlled.

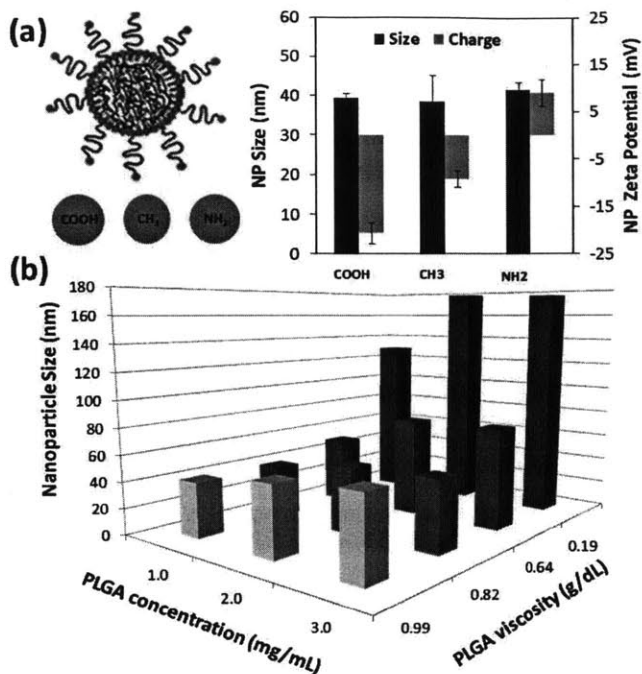


Figure 2.3. Control of nanoparticle physicochemical properties.

(a) Control of surface charge and lipid coverage of the hybrid NPs is elucidated by changes in zeta potential of the NPs in PBS using DSPE-PEG with modified functional groups of carboxyl, methyl, and amine (b) Control of NP size by varying PLGA viscosity and concentration in the organic stream. Flow ratios of aqueous to organic streams and rate were kept constant at 10 : 1 at a total flow rate of 50 $\mu\text{L}/\text{min}$.

2.4. Investigating the role of rapid mixing and mechanism of self-assembly of the hybrid nanoparticles

To gain more insight into the role of rapid mixing in self-assembly of the NPs, we compared the formation of NPs under rapid mixing conditions versus slow mixing conditions obtained by pipetting the same volume of polymer solution used in the microfluidic device into a lipid solution without sonication or heating. Figure 2.4a shows the size distributions in water and in PBS of NPs prepared under rapid mixing with the microfluidic chip and slow mixing

conditions. Under slow mixing conditions at a 1:1 ratio of lipid to PLGA, the formation of liposomes is noted by the peak around 400 nm. A peak around 10 μm in PBS, characteristic of aggregates of polymeric NPs, indicates the formation of polymeric NPs. Finally some hybrid lipid-polymeric NPs are formed since there is a stable peak around 100 nm in water and PBS. The hybrid NPs formed under slow mixing are not homogenous, noted from the irregularity in the peak around 100 nm. This observation suggests uneven distribution of lipid-PEG among the polymeric NPs since lipid-PEG confers stability to the hybrid NPs through formation of the PEG corona (Figure A1.3, appendix). Formation of polymeric NPs, lipid-polymeric NPs and liposomes, was also observed for a lipid to a PLGA ratio of 1:10. However, the larger peaks in water and PBS around 100-1000 nm are not as prominent as for the 1:1 case since the percentage by volume of polymeric NPs formed is much higher than that of liposomes. Under rapid mixing within the microfluidic channel, homogenous and stable hybrid NPs and liposomes are obtained at a lipid to polymer ratio of 1:1 and only stable homogenous hybrid NPs are obtained at a lipid to polymer ratio of 1:10, as inferred by the absence of larger aggregates upon addition of PBS. A size distribution by intensity is shown in the supporting information where the formation of distinct populations of NPs is clearly evident in the case of slow mixing of lipid and PLGA solutions, but only a single population is seen in the case of rapid mixing of lipid and PLGA solutions (Figure A1.4, appendix).

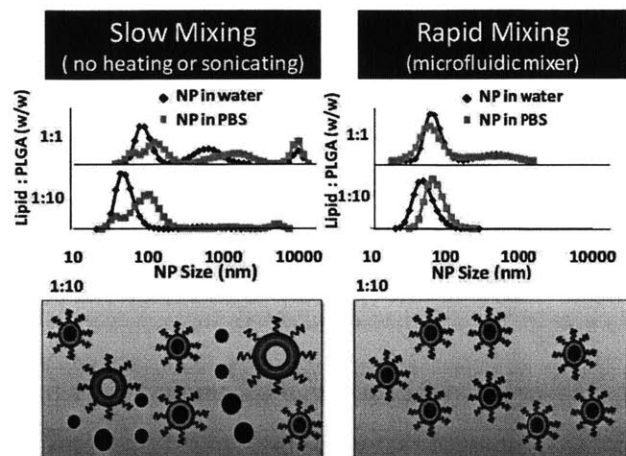


Figure 2.4. Slow versus rapid mixing.

Comparison of NP size distribution in water and PBS for rapid and slow mixing of lipid and PLGA solutions with lipid : PLGA ratios of 1:1 and 1:10. Under slow mixing conditions without the input of any form of energy, aggregation upon addition of PBS indicates the presence of heterogeneous NPs (*i.e.* polymeric, lipid, and lipid-polymeric). Under rapid mixing conditions, absence of aggregation upon addition of PBS indicates that only homogenous hybrid lipid-polymeric NPs are formed, except for the 1:1 ratio that results in homogeneous hybrid NPs and liposomes.

These results give some insight into the role of rapid mixing in the self-assembly of hybrid lipid NPs. Under rapid mixing, there is uniform lipid and lipid-PEG coverage around polymeric cores resulting in the formation of homogenous hybrid lipid-polymeric NPs. In contrast, under slow mixing, some lipid and lipid-PEG is deposited onto polymeric NPs while the rest forms lipid structures leaving polymeric NPs with uneven or no coverage. The result is the formation of a combination of liposomes, polymeric NPs, and hybrid-lipid NPs (Figure A1.4, appendix). An input of energy to the system in the form sonication and/or raise in the temperature as provided in the bulk methods of synthesis may assist in the disassembly of lipid structures and their re-assembly around the polymeric cores forming homogenous lipid-polymeric NPs. Integration of rapid mixing using microfluidics bypasses the intermediate steps needed in slow mixing conditions in the preparation of homogenous lipid-polymeric NPs.

While the above experiment suggests that rapid mixing plays an important role in ensuring uniform lipid coverage on the NPs, it does not explain the invariance of NP size with lipid concentration. Interestingly, even a 1:1000 lipid : PLGA ratio was sufficient to maintain the hybrid NP at a size of 40 nm as opposed to NPs made with only PLGA, which increased in size over a period of few hours. In addition, subsequent increase of the lipid : PLGA ratio by three orders of magnitude did not affect the hybrid NP size (although some liposomes were formed in the 1:1 case). To investigate the role of lipid in self-assembly of the NPs, we designed experiments to elucidate to what extent the self-assembly of PLGA was affected by the presence of the lipid component.

In these experiments, we prepared lipid-PLGA NPs using a ‘two-stage’ manner, where a PLGA polymeric core of a specific size was formed first followed by deposition of the lipid onto PLGA core by flowing the solutions through the microfluidic device for a second time. We then compared the size and size distributions of these NPs with those prepared using the conventional one-step method. First, a PLGA solution in acetonitrile and water were injected into the device. These unprotected PLGA NPs (NP1) were washed and suspended in water at a concentration of 1 mg/mL. Next, NP1 particles in water were immediately reintroduced into the center inlet of the channel and the lipid solutions were introduced through the side channels. The size and size distribution of the lipid-covered NPs (NP2) obtained at the outlet were measured. NP2 particles were placed in PBS to test their stability in comparison to those NPs synthesized through conventional one-step microfluidic method (*i.e.* mixing PLGA solution with the lipid solution) (Figure 2.5). NP2 particles prepared using the two-stage manner had similar size distribution and stability properties to the hybrid NPs prepared in the conventional one-step microfluidic method.

In other words, NPs made from a one-step method and NP2 particles had a uniform distribution with an average size of 40 nm and remained stable when placed in PBS.

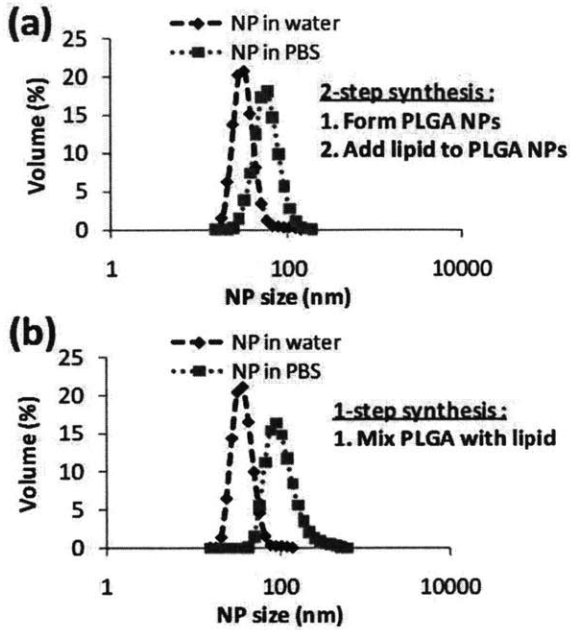


Figure 2.5. NP formation to elucidate stepwise formation of hybrid lipid-polymer NPs within microchannel.

(a) NP size distribution in water and PBS of particles formed in two-stage manner. PLGA NPs were prepared in the microfluidic mixer, then washed and placed as an input along with lipid aqueous stream resulting in the generation of hybrid lipid-PLGA NPs. (b) NP size distribution in water and PBS formed through the current one-step microfluidic method.

These results suggest that self-assembly of the polymeric core of lipid-PLGA NPs in the device was unaffected by the presence of the lipid component. It can be then rationalized that the one-step method indeed involves the above two distinct stages in a very small timescale. The Péclet number ($Pe = V \cdot w / D$) in this case is over 1000, which indicates that convective transport can enhance mixing of particles as long as the streams move laterally.^{24, 25} The Tesla structures in our mixing channel enforce such lateral movement of particles at their junctions. PLGA core formation, the first assembly stage, requires that PLGA chains in the focused acetonitrile stream encounter the anti-solvent, (*i.e.* water molecules), which results in conditions under which PLGA

can precipitate¹⁸. Our microfluidic mixer ensures that complete solvent displacement of acetonitrile by water (0.2-2 ms, see supporting information) occurs on a timescale that is shorter than that of formation of PLGA cores. Furthermore, solvent displacement is almost complete before a substantial amount of lipid approaches the PLGA cores. Lipid shell formation, the second stage, then follows as soon as the lipid molecules are transported to the vicinity of already-formed PLGA cores. Although the diffusion of lipid molecules is slower than that of water molecules at least by an order of magnitude, embedded Tesla structures considerably enhance particle mixing due to their convective effects. Such laterally dispersive transport (combination of diffusion and convection) occurs on a mixing timescale of ~ 10 ms (see supporting information). It is worth noting that the minimal lipid coverage required to stabilize the NPs in water occurs at a lipid : PLGA ratio of 1:1000 and is obtained on a sub-millisecond timescale after sufficient amount of lipid has been transported near the core. In other words, sufficient lipid coverage to prevent long-term aggregation is achieved on a sub-millisecond timescale after complete mixing of solvent and anti-solvent. Thus, the formation of the lipid shell is a transport-limited process since the timescale of coverage is limited by the timescale of mixing. In cases of ratios of lipid : PLGA higher than 1:1000, partial mixing of lipid molecules with acetonitrile would be sufficient for minimum lipid coverage of the PLGA cores. The lipid shell forms on the timescale of 1 ms in the case of 1:1 ratio of lipid : PLGA. Therefore, the timescales for self-assembly of the PLGA cores is on the same order of magnitude as the timescale for minimum lipid coverage, at least for high lipid : PLGA ratios (see supporting information). In contrast to this minimum coverage, complete coverage of the NP with lipid requires complete mixing, which occurs on the timescales of >10 ms. The fact that hybrid NPs could be prepared in two steps (*i.e.* by first forming PLGA NPs followed by mixing with lipid)

indicates that the size of the NPs formed in the device is independent of the presence of the lipid component on short timescales, and the differences in size of PLGA versus hybrid lipid-PLGA NPs shown in Figure 2.2a occur over a longer timescale before measurement of the NP size. Therefore, these results, along with the invariance of NP size with lipid ratio, show that the lipid component does not play a significant role in the self-assembly of the polymeric NPs but rather it stabilizes the NPs and prevents their aggregation on longer timescales. These results are further supported by measuring the size and size distribution of PLGA NPs immediately upon synthesis, which are in a similar range to hybrid NPs (Figure A1.2 and A1.4, supporting information).

2.5. Preparation of lipid-QD NPs

To demonstrate the versatility of our platform design, we examined the ability of rapid mixing to synthesize hybrid quantum dot (QD) lipid NPs for imaging applications. QDs are semiconducting nanocrystals that possess excellent optical properties that make them suitable to be used as imaging probes.²⁶ However, the hydrophobicity and poor colloidal stability at physiological conditions frequently renders them inappropriate for clinical use.²⁷ In the same fashion as for hybrid lipid-polymeric NPs, it has been proposed and shown that lipid-coated QD provide enhanced NP hydrophilicity, stability in plasma, and an overall improvement of in their biocompatibility.^{28, 29} Others have encapsulated other type of particles such as magnetic NPs³⁰ and gold NPs³¹ inside a lipid and polymeric envelope, respectively.

As a proof of concept to show that a similar microfluidic platform can be used to prepare other NPs, we prepared hybrid NPs composed of QDs encapsulated by lecithin and DSPE-PEG layer (Figure 2.6a). Lipophilic QDs were dissolved in THF (0.5 mg/mL) and introduced in the middle input stream in place of the polymeric stream from the

prior study. The lipid-QD NPs in the product stream showed a homogenous size distribution with an average size of 60 nm and did not need further processing for *in vitro* and/or *in vivo* experiments except for the removal of a small fraction of THF through filtration or evaporation (Figure 2.6b). At an initial concentration of 0.5 mg/mL, TEM images show an average of four quantum dots encapsulated per NP (Figure 2.6c). The number of QDs could be controlled by varying the concentration of QDs in THF. To ensure that the images obtained from TEM are QDs encapsulated on lipid NPs and not QDs adhered to the surface of a lipid matrix, images were taken of the operating channels to study their formation. It was observed that before encapsulation of QDs, some aggregation of QDs was visible inside the channel and after encapsulation, the channel remained free of QD aggregates (Figure S6, supporting information). These results clearly show that one can use the same microfluidic platform to synthesize distinct types of hybrid NPs. The results suggest that by using this continuous-flow microfluidic technology one can entrap other imaging agents such as gold NPs and/or magnetic NPs inside a lipid or polymeric envelope to form multifunctional particles for use of various imaging modalities. Through selection of appropriate solvents and concentration, therapeutic and imaging agents can be introduced into the input stream to form a theranostic system.

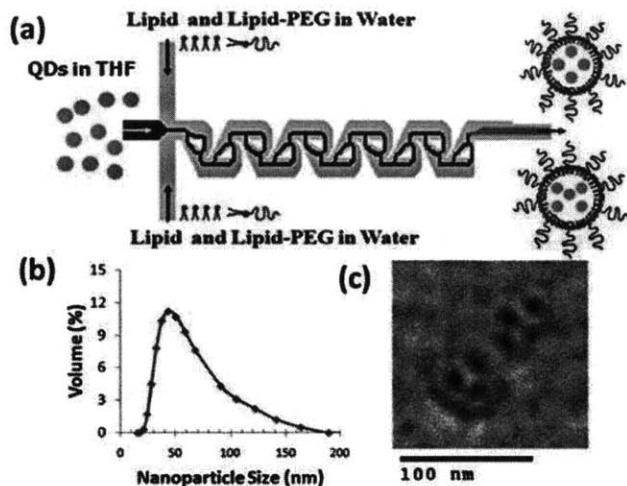


Figure 2.6. Preparation of hybrid lipid-QD NPs.

(a) Schematic of liposome formation in the Tesla mixer with quantum dots encapsulated within the core (b) NP distribution of quantum dot encapsulated liposomes formed through the Tesla mixer (c) TEM image of hybrid lipid-QD NPs stained with 1% phosphotungstic acid aqueous solution showing monodisperse particles with a Z-average size of 60nm. Bar is labeled at 100 nm

2.6. Conclusion

In conclusion, we demonstrated that hybrid lipid-PLGA NPs can be prepared by rapid mixing of a polymeric solution with a lipid solution in a microfluidic device. We identified an optimal ratio of lipid : PLGA that resulted in stable and homogeneous NPs. The size and charge of the NPs could be controlled by using PLGA of different viscosities (molecular weights) and by using lipid molecules with different end groups, respectively. The experiments suggest that the self-assembly of PLGA core occurs independent of the lipid component, but the lipid component provides stability to the NP against aggregation over time and in the presence of high salt concentrations. Furthermore, rapid mixing ensures formation of homogeneous NPs; in contrast, slow mixing results in different populations of NPs that are not uniform in composition and size. We also demonstrated that hybrid lipid-QD NPs could be formed in the same system. Reproducible manufacture of monodisperse, stable NPs with the ability to control properties by

varying concentrations of different precursors in a simple mixing step could greatly facilitate combinatorial synthesis and prove to be useful in the emerging field of nanomedicine.

2.7. Experimental methods

Device fabrication and experimental setup. Microfluidic devices were fabricated with poly(dimethylsiloxane) (PDMS) using a standard micromolding process. PDMS (Sylgard 184, Dow Corning) monomer and curing agent were mixed in a ratio of 10:1 by weight, pored over the silicon wafer mold, and degassed. After curing, PDMS was peeled off and inlet/outlet holes were drilled using a 300 μm diameter drill bit. The PDMS component was then bonded to a 1" \times 2" glass slide using air plasma. The resulting device had one inlet each for water and solvent streams, and one outlet. The water stream was split into two in order to achieve two water streams at the flow focusing junction. The mixing channel was 50 μm wide, 60 μm high and 2.5 mm long. One 500 μL syringe was mounted on a syringe pump (SP230IW, World Precision Instruments) while the other syringe was mounted on another syringe pump (PHD 22/2000, Harvard Apparatus) to control flow through the device. Water flow rate was maintained at 50 $\mu\text{L}/\text{min}$, while the solvent flow rate was varied from 5 $\mu\text{L}/\text{min}$ to 10 $\mu\text{L}/\text{min}$.

Preparation of PLGA-lecithin-PEG NPs. A solution of PLGA (intrinsic viscosity 0.82 g/dL; Lactel, Pelham, AL) was dissolved in acetonitrile (1mg/mL) and lipid solution composed of 4% ethanol aqueous solution of lecithin (soybean, refined, molecular weight: \sim 330 Da; Alfa Aesar, Ward Hill, MA) and DSPE-PEG (molecular weight: \sim 2850 Da; Avanti Polar Lipids, Alabaster, AL) (lecithin/DPSE PEG, 8.4/1.6) were prepared independently for separate inlets and mixed within the chip at fixed flow rates using syringe pumps. Lipid solution flow rate was fixed at 50

$\mu\text{L}/\text{min}$ while polymer solution flow rate was set at $10 \mu\text{L}/\text{min}$ for some experiments and $5 \mu\text{L}/\text{min}$ for others. Lipid concentration was varied from 10^2 to $0.1 \mu\text{g}/\text{mL}$ at a constant flow rate of $50 \mu\text{L}/\text{min}$. To prepare NPs at slow mixing conditions, $100 \mu\text{L}$ of the lipid solution described in the previous paragraph was mixed with $10 \mu\text{L}$ of PLGA solution in acetonitrile using pipette tips. For the NP stability studies, $20 \mu\text{L}$ of $10\times$ PBS were added to $60 \mu\text{L}$ of the NP solution. Size and zeta potential of NPs were immediately measured upon addition of PBS. For hybrid lipid-PLGA NPs prepared with the microchannel, up to four consecutive additions of $20 \mu\text{L}$ of $10\times$ PBS were pipetted to $60 \mu\text{L}$ of the sample and its size was monitored for each addition. No change in size was observed after the first addition of the buffer.

Preparation of QD-lecithin-PEG NPs. A solution of lipophilic quantum dots (TOP-coated CdSe/ZnS QDs, Invitrogen, CA, USA) was dissolved in tetrahydrofuran (THF) ($0.5 \text{ mg}/\text{mL}$) and a lipid solution of 4% ethanol aqueous solution of lecithin and DSPE-PEG (lecithin/DPSE PEG, 8.4/1.6) at a concentration of $0.2 \text{ mg}/\text{mL}$ were prepared independently for separate inlets and mixed within the chip. Lipid solution flow rate was set at $50 \mu\text{L}/\text{min}$ while QD solution flow rate was set at $5 \mu\text{L}/\text{min}$. Both flow rates were controlled with syringe pumps.

Particle sizing and zeta potential measurements. Particle sizing was performed using dynamic light scattering with Zetasizer Nano ZS (Malvern Instruments Ltd., U.K.). For each measurement, $100 \mu\text{L}$ or more volume of the sample was loaded in a disposable low-volume cuvette. Three measurements were performed on each sample. We observed that the presence of acetonitrile changed the NP size by less than 3 % when water-acetonitrile mixtures containing up to 5 % acetonitrile were further diluted in water. All measurements were performed at acetonitrile concentrations of less than 10 % acetonitrile to ensure that any observed variation in particle size was not due to the solvent. The NP surface zeta potential was measured by using

ZetaPALS (Brookhaven Instrument., U.S.A). For each measurement, particles were washed with water three times and reconstituted in 1mL of PBS (0.5mg/mL). The zeta potential was recorded as the average of three measurements.

Transmission electron microscopy (TEM)

Lipid-polymeric NPs. TEM experiments were carried out on a JEOL JEM-200CX instrument at an acceleration voltage of 200 kV. The TEM sample was prepared by depositing 10 μ L of the NP suspension (1.0 mg/mL) onto a 200-mesh carbon-coated copper grid. Samples were blotted away after 30 min incubation and grids were negatively stained for 20 min at room temperature with freshly prepared and sterile-filtered 2% (w/v) uranyl acetate aqueous solution. The grids were then washed twice with distilled water and air dried prior to imaging.

Lipid-QD NPs TEM experiments were carried out on a JEOL JEM-2011 instrument at an acceleration voltage of 200 kV. The TEM sample was prepared by depositing 10 μ L of the NP suspension (1.0 mg/mL) onto a 300-mesh formvar-coated copper grid. Samples were blotted away after 30 min incubation and grids were negatively stained for 20 min at room temperature with sterile-filtered 1% (w/v) phosphotungstic acid aqueous solution. The grids were then washed twice with distilled water and air dried prior to imaging.

2.8. References

1. Peer, D.; Karp, J. M.; Hong, S.; Farokhzad, O. C.; Margalit, R.; Langer, R., Nanocarriers as an Emerging Platform for Cancer Therapy. *Nat Nanotechnol* **2007**, 2, (12), 751-60.
2. Wagner, V.; Dullaart, A.; Bock, A. K.; Zweck, A., The Emerging Nanomedicine Landscape. *Nat Biotechnol* **2006**, 24, (10), 1211-7.
3. Zhang, L.; Chan, J. M.; Gu, F. X.; Rhee, J. W.; Wang, A. Z.; Radovic-Moreno, A. F.; Alexis, F.; Langer, R.; Farokhzad, O. C., Self-Assembled Lipid--Polymer Hybrid Nanoparticles: A Robust Drug Delivery Platform. *ACS Nano* **2008**, 2, (8), 1696-702.

4. Chan, J. M.; Zhang, L.; Yuet, K. P.; Liao, G.; Rhee, J. W.; Langer, R.; Farokhzad, O. C., Plga-Lecithin-Peg Core-Shell Nanoparticles for Controlled Drug Delivery. *Biomaterials* **2009**, 30, (8), 1627-34.
5. Sengupta, S.; Eavarone, D.; Capila, I.; Zhao, G.; Watson, N.; Kiziltepe, T.; Sasisekharan, R., Temporal Targeting of Tumour Cells and Neovasculature with a Nanoscale Delivery System. *Nature* **2005**, 436, (7050), 568-72.
6. Hall, J. B.; Dobrovolskaia, M. A.; Patri, A. K.; McNeil, S. E., Characterization of Nanoparticles for Therapeutics. *Nanomed* **2007**, 2, (6), 789-803.
7. Gu, F.; Zhang, L.; Teply, B. A.; Mann, N.; Wang, A.; Radovic-Moreno, A. F.; Langer, R.; Farokhzad, O. C., Precise Engineering of Targeted Nanoparticles by Using Self-Assembled Biointegrated Block Copolymers. *Proc Natl Acad Sci U S A* **2008**, 105, (7), 2586-91.
8. Jahn, A.; Reiner, J. E.; Vreeland, W. N.; DeVoe, D. L.; Locascio, L. E.; Gaitan, M., Preparation of Nanoparticles by Continuous-Flow Microfluidics. *J. Nanopart Res* **2008**, 10, 925-934.
9. Karnik, R.; Gu, F.; Basto, P.; Cannizzaro, C.; Dean, L.; Kyei-Manu, W.; Langer, R.; Farokhzad, O. C., Microfluidic Platform for Controlled Synthesis of Polymeric Nanoparticles. *Nano Lett* **2008**, 8, (9), 2906-12.
10. Gu, F. X.; Karnik, R.; Wang, A. Z.; Alexis, F.; Levy-Nissenbaum, E.; Hong, S.; Langer, R.; Farokhzad, O. C., Targeted Nanoparticles for Cancer Therapy *nanotoday* **2007**, 2, (3), 14-21.
11. Yen, B. K.; Gunther, A.; Schmidt, M. A.; Jensen, K. F.; Bawendi, M. G., A Microfabricated Gas-Liquid Segmented Flow Reactor for High-Temperature Synthesis: The Case of Cdse Quantum Dots. *Angew Chem Int Ed Engl* **2005**, 44, (34), 5447-51.
12. Xu, Q.; Hashimoto, M.; Dang, T. T.; Hoare, T.; Kohane, D. S.; Whitesides, G. M.; Langer, R.; Anderson, D. G., Preparation of Monodisperse Biodegradable Polymer Microparticles Using a Microfluidic Flow-Focusing Device for Controlled Drug Delivery. *Small* **2009**, 5, (13), 1575-81.
13. Martin-Banderas, L.; Flores-Mosquera, M.; Riesco-Chueca, P.; Rodriguez-Gil, A.; Cebolla, A.; Chavez, S.; Ganan-Calvo, A. M., Flow Focusing: A Versatile Technology to Produce Size-Controlled and Specific-Morphology Microparticles. *Small* **2005**, 1, (7), 688-92.
14. Rondeau, E.; Cooper-White, J. J., Biopolymer Microparticle and Nanoparticle Formation within a Microfluidic Device. *Langmuir* **2008**, 24, (13), 6937-45.
15. Jahn, A.; Vreeland, W. N.; DeVoe, D. L.; Locascio, L. E.; Gaitan, M., Microfluidic Directed Formation of Liposomes of Controlled Size. *Langmuir* **2007**, 23, (11), 6289-93.
16. Jahn, A.; Vreeland, W. N.; Gaitan, M.; Locascio, L. E., Controlled Vesicle Self-Assembly in Microfluidic Channels with Hydrodynamic Focusing. *J Am Chem Soc* **2004**, 126, (9), 2674-5.
17. De Miguel, I.; Imbertie, L.; Rieumajou, V.; Major, M.; Kravtsoff, R.; Betbeder, D., Proofs of the Structure of Lipid Coated Nanoparticles (Smbv) Used as Drug Carriers. *Pharm Res* **2000**, 17, (7), 817-24.
18. Thevenot, J.; Troutier, A. L.; David, L.; Delair, T.; Ladaviere, C., Steric Stabilization of Lipid/Polymer Particle Assemblies by Poly(Ethylene Glycol)-Lipids. *Biomacromolecules* **2007**, 8, (11), 3651-60.
19. Wong, H. L.; Rauth, A. M.; Bendayan, R.; Manias, J. L.; Ramaswamy, M.; Liu, Z.; Erhan, S. Z.; Wu, X. Y., A New Polymer-Lipid Hybrid Nanoparticle System Increases Cytotoxicity of Doxorubicin against Multidrug-Resistant Human Breast Cancer Cells. *Pharm Res* **2006**, 23, (7), 1574-85.

20. Johnson, B. K.; Prud'homme, R. K., Mechanism for Rapid Self-Assembly of Block Copolymer Nanoparticles. *Phys Rev Lett* **2003**, *91*, (11), 118302.
21. DeMello, A. J., Control and Detection of Chemical Reactions in Microfluidic Systems. *Nature* **2006**, *442*, (7101), 394-402.
22. Hong, C. C.; Choi, J. W.; Ahn, C. H., A Novel in-Plane Passive Microfluidic Mixer with Modified Tesla Structures. *Lab Chip* **2004**, *4*, (2), 109-13.
23. Salvador-Morales, C.; Zhang, L.; Langer, R.; Farokhzad, O. C., Immunocompatibility Properties of Lipid-Polymer Hybrid Nanoparticles with Heterogeneous Surface Functional Groups. *Biomaterials* **2009**, *30*, (12), 2231-40.
24. Asgar, A.; Bhagat, S.; Papautsky, I., Enhancing Particle Dispersion in a Passive Planar Micromixer Using Rectangular Obstacles. *Journal of Micromechanics and Microengineering* **2008**, *18*, (8), -.
25. Rhee, M.; Burns, M. A., Drop Mixing in a Microchannel for Lab-on-a-Chip Platforms. *Langmuir* **2008**, *24*, (2), 590-601.
26. Michalet, X.; Pinaud, F. F.; Bentolila, L. A.; Tsay, J. M.; Doose, S.; Li, J. J.; Sundaresan, G.; Wu, A. M.; Gambhir, S. S.; Weiss, S., Quantum Dots for Live Cells, in Vivo Imaging, and Diagnostics. *Science* **2005**, *307*, (5709), 538-44.
27. Klostranec, J. M.; Chan, W. C. W., Quantum Dots in Biological and Biomedical Research: Recent Progress and Present Challenges. *Adv. Mater* **2006**, *18*, 1953-1964.
28. Carion, O.; Mahler, B.; Pons, T.; Dubertret, B., Synthesis, Encapsulation, Purification and Coupling of Single Quantum Dots in Phospholipid Micelles for Their Use in Cellular and in Vivo Imaging. *Nat Protoc* **2007**, *2*, (10), 2383-90.
29. Dubertret, B.; Skourides, P.; Norris, D. J.; Noireaux, V.; Brivanlou, A. H.; Libchaber, A., In Vivo Imaging of Quantum Dots Encapsulated in Phospholipid Micelles. *Science* **2002**, *298*, (5599), 1759-62.
30. Park, J. H.; von Maltzahn, G.; Ruoslahti, E.; Bhatia, S. N.; Sailor, M. J., Micellar Hybrid Nanoparticles for Simultaneous Magnetofluorescent Imaging and Drug Delivery. *Angew Chem Int Ed Engl* **2008**, *47*, (38), 7284-8.
31. Gindy, M. E.; Panagiotopoulos, A. Z.; Prud'homme, R. K., Composite Block Copolymer Stabilized Nanoparticles: Simultaneous Encapsulation of Organic Actives and Inorganic Nanostructures. *Langmuir* **2008**, *24*, (1), 83-90.

Chapter 3 - Microfluidic System for Synthesis of Multifunctional Nanoparticles: 3D Flow Focusing

3.1. Introduction

Recently, polymeric nanoparticles (NPs) have attracted enormous attention as targeted drug delivery vehicles¹⁻⁴. Especially, biodegradable and biocompatible polymeric NPs comprised of poly(lactide-*co*-glycolide)-*b*-polyethyleneglycol (PLGA-PEG) block copolymers exhibit optimal physicochemical characteristics such as the ability to incorporate various targeting agents, enhanced immune evasion, controlled drug release, and high payload of drug molecules^{5,6}. Targeted PLGA-PEG NPs have shown very promising *in vivo* results for treatment of cancer⁷⁻⁹ and they are now poised to enter clinical trials. Preparation of such targeted NPs in a robust and reproducible manner has thus become very important for therapeutic applications where precise control of the physicochemical properties of NPs is required to achieve optimal biodistribution and therapeutic efficacy¹⁰.

While the conventional approach to synthesize polymeric NPs relies on ‘bulk’ nanoprecipitation by solvent exchange^{11,12}, our group recently reported a new reproducible synthesis of highly uniform PLGA-PEG NPs using 2D hydrodynamic flow focusing (HFF) in

microfluidic channels^{13,14}. In this method, the polymer stream in acetonitrile (ACN) horizontally focused only by water sheath streams experiences rapid mixing with water with a characteristic mixing time faster than the NP assembly time, resulting in homogeneous NPs^{13,15}. However, one of the challenges for optimal NP synthesis by 2D HFF is that NPs made from polymers with a PLGA block of high molecular weight (MW) (> 45kDa) tend to aggregate on the channel walls, resulting in clogging of the channels. Aggregation is caused by the adsorption of the hydrophobic PLGA onto the hydrophobic walls of PDMS, which depends both on concentration and molecular weight^{16,17}. This substantially reduces the robustness of operation – the ability to synthesize NPs without device failure – and is a nontrivial drawback of the 2D HFF technique because NPs made from high MW PLGA blocks tend to exhibit higher drug loading and tunable drug release profile as the polymer MW is varied^{12, 18, 19}. Furthermore, aggregation of the polymer on the channel walls frequently causes the device to irreversibly fail due to increased internal pressure²⁰. Such channel fouling may be circumvented by modification of the channel surface with Teflon-like materials²¹. However, efficient surface modification requires laborious silicon/glass fabrication or a separate deposition/curing step that is extremely demanding, and the coating tends to degrade over time. For this application and many others, a preferred solution would be to isolate the precipitating polymer from the channel walls by 3D focusing in both the horizontal and the vertical dimensions, thereby preventing aggregation and clogging.

Over the past few years, several unique 3D HFF systems have been reported²²⁻³¹, including intrinsic 3D structures such as horizontal nozzles^{22,23} and vertical chimneys²⁴. Other 3D HFF systems with 3D channel network either with a single two-level layer^{27,28} or with two individual layers²⁹⁻³¹ have been also proposed. However, their construction requires high-level expertise of fabrication, considerably high costs and limited reproducibility. More recently,

‘microfluidic drifting,’ a methodology of 3D fluid manipulation in a single layer, has been also introduced^{25,26}. Despite its fabrication simplicity, this method functions only at high Re numbers and a relatively low sample flow rate, which may cause substantial dilution of the sample flow and low throughput. Because of the complications with the previously proposed 3D HFF systems, there is demand for a platform that is sufficiently versatile and simple for both fabrication and operation.

In this work we present a simple design for 3D HFF composed of a monolithic single layer with three sequential inlets for vertical focusing followed by a conventional cross junction for horizontal focusing. We use this device for the synthesis of polymeric NPs at various polymer concentrations and MWs —the assembly of some of them being significantly difficult by 2D HFF or bulk nanoprecipitation. Optimal ranges of operational parameters are predicted by mathematical modeling and geometric dimensions of channels and inlet holes are fine-tuned by finite element simulations to ensure that the polymer stream is sufficiently exposed to the anti-solvent (water) stream but is not in touch with channel walls. Using confocal microscopy, we further confirm the presence, the position and the shape of the 3D focused polymer stream, which is important for optimal nanoprecipitation of polymeric NPs.

3.2. Design of microfluidic device

Figure 3.1a shows a schematic of our 3D focusing channel design for polymeric NP synthesis. The polymer flow (Inlet B) containing polymer precursors dissolved in ACN is first vertically focused by two vertical ACN sheath flows (Inlet A and C). The vertically arranged stream is subsequently focused horizontally by the water sheath streams and the resulting solvent exchange induces self-assembly of the nanoparticles. Thus, 3D focusing enables isolation of the precipitating polymer from the channel walls. Using this microfluidic device, we synthesized

various PLGA-PEG NPs at different polymer precursor concentrations and MWs to investigate the robustness of nanoprecipitation by 3D HFF. In Figure 3.1b, TEM images of PLGA-PEG NPs made from polymers with various MW and concentrations by 3D HFF show that this method yields fairly monodisperse NPs with a range of sizes.

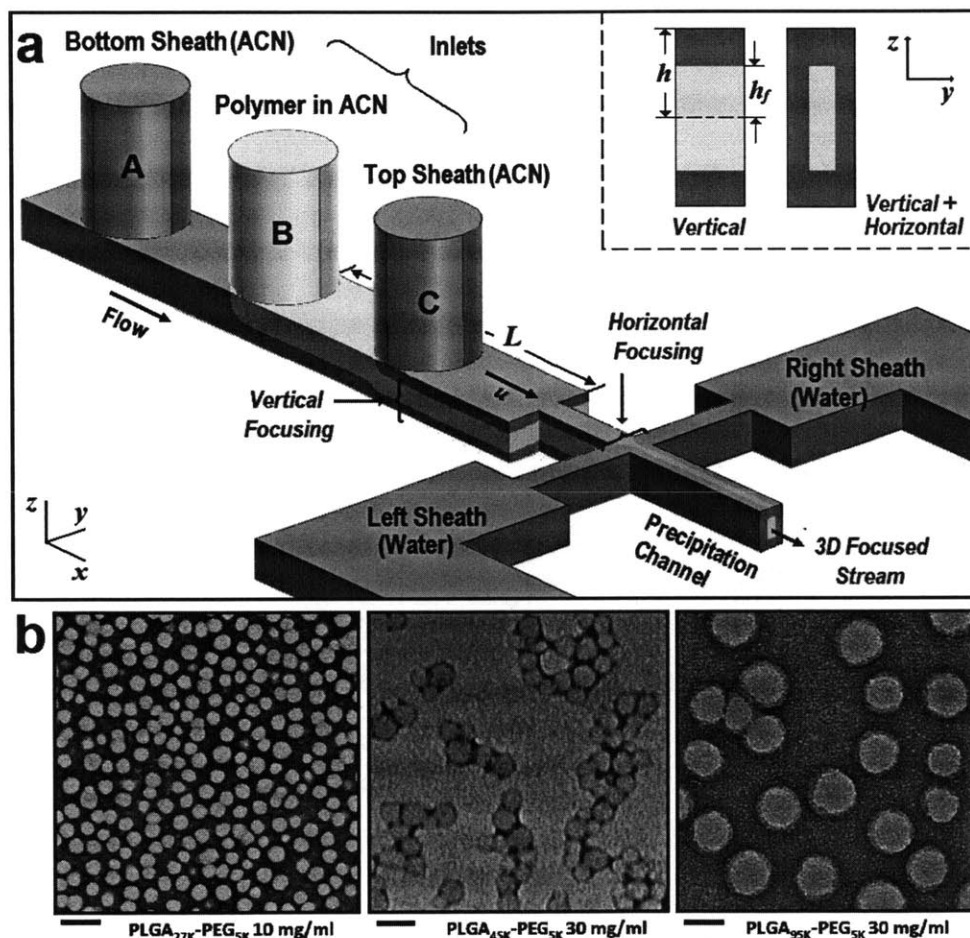


Figure 3.1. Device design and representative nanoparticles.

(a) Concept of device for 3D hydrodynamic focusing (not to scale) consisting of three sequential inlets for vertical focusing and a separate inlet for side sheath flows (not shown). The cross-sectional views in the inset show the vertically focused stream profile (left) and the heterogeneous 3D hydrodynamic focusing where the sample flow is isolated both horizontally and vertically (right). (b) TEM images of PLGA-PEG NPs obtained from PLGA_{27K}-PEG_{5K} at 10 mg/mL in ACN (scale bar 100 nm), PLGA_{45K}-PEG_{5K} at 30 mg/mL in ACN (scale bar 100 nm) and PLGA_{95K}-PEG_{5K} at 30 mg/mL in ACN (scale bar 200 nm) using 3D HFF with the flow ratio of Polymer:ACN = 3:7 and organic:water = 1:5. Average NP sizes are 33.8, 55.0, and 200 nm, respectively.

3.3. Comparison of 2D versus 3D flow focusing

For comparison between the conventional 2D HFF and 3D HFF, we also constructed 2D HFF channel with identical geometry except for the absence of the two ACN sheath inlets in Figure 3.1a and we maintained all flow parameters such as net organic stream and water stream flow rates, ensuring similar focused stream geometry and molecular residence time the same for 2D and 3D. When comparing nanoprecipitation using 2D versus 3D HFF (Figure 3.2a), we found that only the 3D HFF method could successfully produce NPs with long-term operation (>10 min) without channel fouling. Polymers with high MWs or high concentrations are usually more susceptible to aggregation in microchannels. Such aggregation during 2D HFF occurred unpredictably at random locations along the channel and thus resulted in poor reproducibility. We also compared the size and monodispersity of NPs synthesized by 3D HFF to 2D HFF and conventional bulk nanoprecipitation for various concentrations (10-50 mg/mL) and PLGA-PEG MWs (27, 45, and 95kDa) to verify the quality of NPs prepared by this method (Figure 3.2b). 3D HFF consistently yielded NPs with the smallest size and lowest polydispersity while 2D HFF and bulk method sometimes produced distinctly larger NPs, or failed to produce NPs at all. NP synthesis by 2D HFF was impossible for high MW and high concentration cases due to device failure caused by aggregation. Figure 3.2c shows a comparison of the size distributions of NPs made from PLGA_{95K}-PEG_{5K} precursors at low and high concentrations (10mg/mL and 50mg/mL, respectively) using the three different methods. At high concentrations, NPs obtained by 2D HFF and bulk method yielded highly polydisperse particles of extremely large size (>1000 nm), while 3D HFF consistently resulted in smaller NPs with relatively low polydispersity regardless of polymer concentrations. These observations indicate that 2D HFF is comparable with 3D HFF

only for small MW polymers or very low polymer concentrations where the channels are less susceptible to fouling. Consequently, 3D HFF is the only method that enables the reproducible synthesis of monodisperse NPs made from different PLGA MWs and at different concentrations with average NP sizes ranging from 30 to 230 nm.

To identify conditions that enable robust nanoprecipitation in our 3D HFF device, we assembled pure poly(lactic-co-glycolic acid) (PLGA) NPs that are especially prone to aggregation due to the absence of the protective hydrophilic PEG chain as an extreme case model of PLGA-PEG NPs without the PEG shell. Since the flow velocity is slow before horizontal focusing by the water streams, diffusion of the vertically focused polymer stream to the walls must be minimized to prevent isolation. We used a mathematical model to predict optimal parameter ranges for reproducible synthesis of PLGA NPs without aggregation. These parameters collectively define two phases to which the synthesis conditions correspond; the conditions where good and predictable NPs are synthesized in the microfluidic rapid mixing environment without aggregation (Phase I, Good NPs) and the conditions where aggregation occurs (Phase II, Aggregation) (Figure 3.2d). We expressed the phase space in terms of two parameters: *i*) the fraction of polymer flow rate and *ii*) the modified *Péclet* number (Pe^*). First, as the fraction of polymer flow rate in total organic (polymer + ACN) flow rate (f) increases, the vertical sheath layer becomes thinner, and eventually the focusing profile approaches to 2D HFF ($f=1$ for 2D HFF), where the system is more susceptible to aggregation. Second, Pe^* , defined as a product of the *Péclet* number ($u_{max} \cdot h/D$, where u_{max} is the maximal flow velocity and D is the diffusion coefficient of polymer precursors in ACN) and the ratio of channel height to focusing length (h/L), takes into account the relative importance of convection to diffusion of the polymer precursor. The solid green line in Figure 3.2d represents conditions where the focusing *Péclet*

number, $Pe_f = (1/3) * Pe^* \cdot (1-f)^2$, is 10, which indicates that axial convection effectively dominates over lateral diffusion. This dimensionless number not only describes the ratio of diffusive and convective timescales but accounts for thickness of the sheath layer during flow focusing. For low Pe^* , precursor molecules in the focused stream rapidly diffuse from the center to the channel wall. We then expect significant concentration of polymer at the wall, invalidating vertical focusing. The condition where $Pe_f = 10$ thus serves as a suggested boundary line between Phase I and II. The polymer precursor concentration near the walls acts as a critical determinant of aggregation. Based on the empirical observations that aggregation occurred only when the polymer concentration exceeded a certain threshold (in case of 2D HFF), we defined a critical wall concentration (1 mg/mL for PLGA_{70K}) for 3D HFF, above which aggregation may be expected. Conditions under which a wall concentration of 1 mg/mL is obtained from mathematical modeling (dashed red line in Figure 3.2d) agree qualitatively with the line corresponding to $Pe_f = 10$, as is expected for the polymer concentration used in experiments. Consequently, Figure 3.2d shows good agreement between experimental data and the calculated phase diagram. These results suggest that diffusion of polymers into the vertical sheath flows, governed by the polymer flow ratio (f) and the modified *Péclet* number can explain regimes where the 3D HFF device can successfully isolate the precipitating polymers from the channel walls and operate without aggregation. Thus, we can mathematically predict optimal operating conditions in our system that result in robust nanoprecipitation of NPs and prevent fouling of the microchannel.

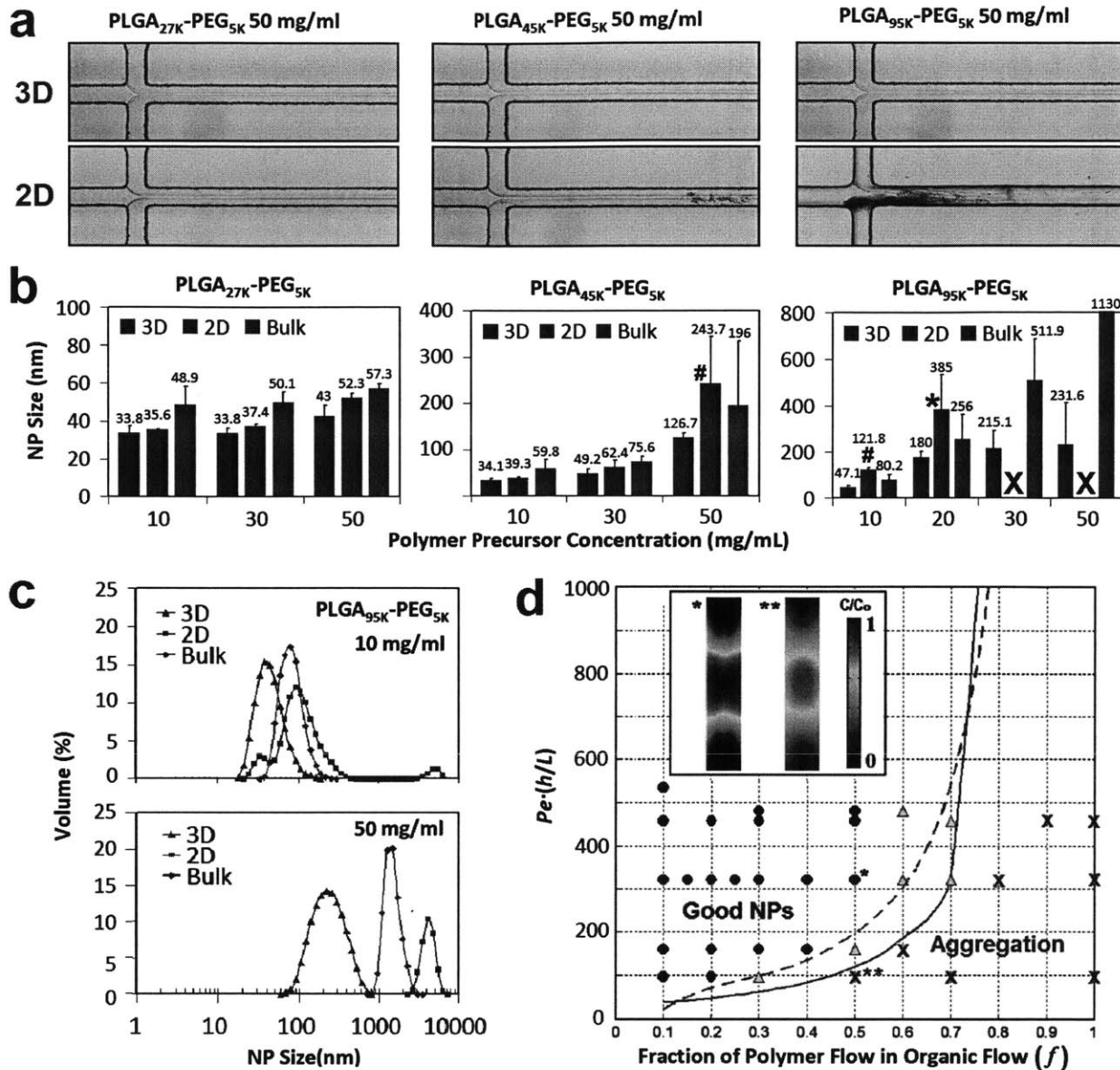


Figure 3.2. Comparison of 3D HFF, 2D HFF, and bulk nanoprecipitation of PLGA-PEG NPs under different conditions.

(a) Representative channel images of the device during synthesis of PLGA-PEG NPS by 3D HFF and 2D HFF for various MW precursors, showing aggregation in the case of 2D HFF. All micrographs were captured after ~500 s of operation (channel width 20 μ m). (b) Effect of the PLGA-PEG precursor concentration on the final NP sizes depending on the MW of the precursors and the choice of a synthesis method. X = Clogging of channel within 3 minutes of operation. * = Aggregation of polymer in channel observed after 5-10 minutes of operation. # = Aggregation of polymer in channel observed after >10 minutes of operation. (c) Size distributions by volume fraction of PLGA_{95K}-PEG_{5K} NPs prepared by microfluidic 3D HFF, 2D, and bulk mixing methods for the precursor concentrations of 10 and 50 mg/mL, respectively. Aggregated particles are found in the 1000-10,000 nm range. (d) Phase space of 3D HFF operation parameters (Pe^* and f) for synthesis of PLGA NPs from pure PLGA_{70K} precursors (10

mg/mL). Solid green line represents conditions where $Pe_f^*=10$ and dashed red line represents conditions under which the PLGA_{70K} precursor reaches a critical wall concentration (1 mg/mL) that results in aggregation. Both lines delineate conditions that result good synthesis of NPs (Phase I) from those that are susceptible to aggregation (Phase II). Symbols indicate experimental data for the synthesis of PLGA_{70K} NPs. (O: reproducible, successful NP synthesis, X: aggregation with microparticle formation, Δ : mild or occasional aggregation). Inset shows simulated concentration profiles at the starting point of nanoprecipitation under the conditions where flow rates (u_{max}) are different but f is the same for Phase I (*) and Phase II (**), respectively.

3.4 Effect of channel geometry on device performance

To elucidate the effect of inlet hole geometry on device performance, we performed finite element simulations using COMSOL. The aspect ratio (width to height, w/h) of the channel where vertical focusing occurs and the size and position of inlet holes are particularly important design factors since they determine the shape of 3D focusing in the channel. The simulations showed a strong influence of the aspect ratio (w/h) on the distribution of the polymer after vertical focusing (Figure 3.3a). For the deep channel with $w/h < 2$, vertical lamination successfully occurred with a flat concentration profile, whereas the channel with $w/h > 2$ resulted in a ‘banana-like’ profile with long tails extending to the top wall, making this configuration more susceptible to aggregation. The inlet hole diameter was also found to significantly influence the concentration profile (Figure 3.3b) and the most uniform vertical focusing was obtained for hole sizes slightly larger than the channel width. Smaller holes significantly compromised vertical focusing, again resulting in a ‘banana-like’ polymer stream profile. Likewise, the lateral position of inlet holes affected the shape of vertically focused polymer stream. Off-centered inlets resulted in a tilted polymer stream (Figure 3.3c), which invalidates vertical focusing since precipitating polymer would touch the channel wall. These simulations

show that the best 3D focusing is obtained using deep, high aspect ratio channels with well-centered holes of diameters slightly larger than the channel width.

Finally, we used confocal microscopy to verify the performance of 3D HFF by three sequential inlets. We used a FITC (green) labeled stream as the focused stream, and a rhodamine (red) labeled stream as the vertical sheath streams. The results in Figure 3.3d showed vertical and horizontal hydrodynamic focusing with the three-sequential-inlet system. In accordance with simulation results, we observed a biased distribution of the focused flow for off-center holes. Similarly, with an inlet hole size smaller ($\sim 150 \mu\text{m}$) than the width ($\sim 200 \mu\text{m}$) of the shallow channel, ‘banana-like’ concentration profiles were observed as predicted with simulations. However, such distortion in polymer distributions was avoided and successful 3D focusing was obtained with a deep channel (low w/h). These observations by confocal microscopy, collectively, are in good agreement with the previous simulations.

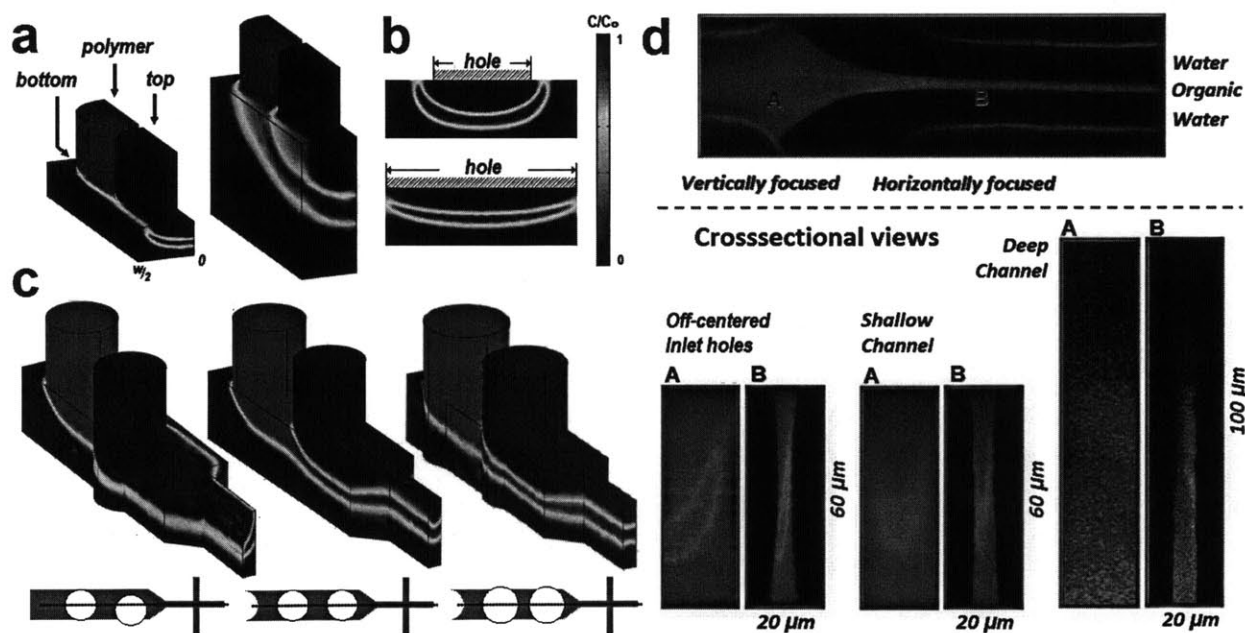


Figure 3.3. Simulation and visualization of focused stream.

(a) 3D simulations with different channel aspect ratios (w/h); 3.33 (left) and 0.83 (right), respectively. Perspective views of the channel with the width of 200 μm and the inlet of 150 μm . Only the left halves about the symmetry plane are shown. (b) Simulated cross-sectional views for two different inlet hole diameters at a fixed channel aspect ratio ($w/h = 3.33$). (c) 3D simulations for a channel of $w = 100 \mu\text{m}$ and $h = 100 \mu\text{m}$, showing off-centered inlet (left), well aligned inlet (center), and slightly larger inlet (right). (d) Confocal micrographs showing cross-sectional views of vertical focusing before (A) and after (B) horizontal focusing. The top panel shows a top-view of the system near the lateral squeezing cross junction. In the bottom left panel, off-centered holes directly compare with the left panel in (c). The bottom center panel shows vertical focusing occurred in the channel of $w/h = 3.33$ while the sequential inlet hole size was slightly smaller. The bottom right panel shows vertical focusing occurred in the channel of $w/h = 1.0$.

3.5. Conclusion

In summary, we presented a new yet simple method to isolate precipitating precursors in microfluidic channels using 3D hydrodynamic focusing enabled by sequential inlets. This approach was used to synthesize PLGA-PEG and PLGA NPs by nanoprecipitation under conditions where monodisperse NPs could neither be synthesized by 2D HFF nor by bulk mixing in a controlled manner. NPs synthesized by 3D HFF exhibited smaller sizes and improved monodispersity compared to 2D HFF or bulk synthesis, keeping the NP size small enough for optimal uptake (i.e. $< 100 \text{ nm}$), which is desired in applications where a high MW PLGA block is needed to obtain a specific release profile or where different hydrophobic polymers are mixed³²⁻³⁴. More importantly, the monodispersity of the 3D HFF enables the fine-tuning of NP size by carefully choosing PLGA block size of the polymer and the concentration in ACN. Mathematical modeling, together with simulations and confocal microscopy verified the design validity for the performance of the device and defined optimal device geometry and operating conditions for robust 3D HFF. This simple yet versatile design can be easily adapted to microfluidic reactors for synthesis of various materials where isolation of precipitating or reacting flow streams is desirable to prevent fouling and increase robustness during operation^{31, 35-37}.

3.6. Materials and methods

Polymer Precursors. For PLGA NPs, a solution of PLGA (inherent viscosity 0.82 dL/g, molecular weight \sim 70,000; Lactel, Pelham, AL) was dissolved in ACN at varying concentrations from 0.5 to 10 mg/mL). For PLGA-PEG NPs, solutions of PLGA-PEG (Boehringer Ingelheim GmbH, Germany) at molecular weights of PLGA_{27K}-PEG_{5K}, PLGA_{45K}-PEG_{5K}, and PLGA_{95K}-PEG_{5K} were dissolved in ACN at concentrations of 10-50 mg/mL.

Device Fabrication. The prototypical device was manufactured using the standard soft-lithographic technique. The SU-8 (MicroChem) resist was spun on a bare 4" silicon wafer and prebaked on a hot plate for 3 min at 65 °C and for 9 min subsequently at 95 °C. After exposure to 365 nm UV light, the coated wafer was postbaked for 1 min at 65 °C and for 7 min subsequently at 95 °C. The successive 4 min development resulted in the 60 μ m thick mold. PDMS (Sylgard 184, Dow Corning) monomer and curing agent were mixed in a ratio of 10:1 by weight, poured over the silicon wafer mold, and degassed. After curing at 100 °C for 60 min, the cured PDMS cast was carefully removed from the mold and diced into individual dies. For each die, inlet/outlet holes were drilled by a 150 μ m diameter drill bit. To prevent holes drilled at off-center positions, a manual travel translation stage was used with a mechanical drill to define the position precisely. The PDMS component was then bonded to a 1 in. \times 2 in. glass slide using air plasma. Typical channel dimensions used in the NP synthesis experiments had a width of 100 μ m and a height of 60 μ m for the vertical focusing part and had a width of 20 μ m for the horizontal focusing part, or precipitation channel.

Fluid Control and NP synthesis. For 3D HFF, A 2.500 mL syringe for water injection was mounted on a syringe pump (SP101I, World Precision Instruments), two 500 μ L syringes for

ACN injection were mounted on a different syringe pump (PHD 2000, Harvard Apparatus), and finally a 250 μL syringe for polymer solution injection was mounted on a syringe pump (PHD ULTRA, Harvard Apparatus). Water and organic flow rates were maintained at 50 $\mu\text{L}/\text{min}$ and 10 $\mu\text{L}/\text{min}$, respectively (60 $\mu\text{L}/\text{min}$ in total), while the fraction of polymer flow rates in the organic flow were varied from 0.1 to 1. To prepare NPs by 2D HFF we used a channel design previously published⁵ and ran a polymer stream at different concentrations at an organic to aqueous flow ratio of 1:10. For 3D and 2D, we used devices with the exactly same dimensions, and all flow rates were also identical. The water flow rate was always 50 $\mu\text{L}/\text{min}$ for both 3D and 2D, and the organic flow rate was always 10 $\mu\text{L}/\text{min}$ for both 3D and 2D. For example, for 3D HFF with polymeric stream 3 $\mu\text{L}/\text{min}$ and total ACN sheath 7 $\mu\text{L}/\text{min}$ ($f = 0.3$) for a net organic flow rate of 10 $\mu\text{L}/\text{min}$, the corresponding 2D HFF polymeric stream flow rate was 10 $\mu\text{L}/\text{min}$. Consequently, the width of the organic stream focused by the water sheath streams, fluid velocities, and residence times were the same for 3D and 2D. The average fluid velocity for the vertical focusing region was approximately 0.028 m/s. The corresponding residence time for this 1.5 mm vertical focusing region was about 54 ms. The average fluid velocity in the following precipitation channel was 0.83 m/s and the residence time for 4 mm long precipitation channel was about 4.8 ms. The total residence time for polymeric molecules in the microfluidic channel was ~ 58.8 ms. Reynolds numbers for precipitation and vertical focusing channels were 16.6 and 3.5, respectively. In bulk, we mixed 200 mL of polymer precursor solution drop-wise with 2 mL of water during 1-2 hrs. NPs were measured immediately after. It was also noticed that NPs size did not varied significantly after washing NPs with water several times.

Particle Sizing. Particle sizing was performed using dynamic light scattering with Zetasizer Nano ZS (Malvern Instruments Ltd., U.K.). For each measurement, 100 μL or more volume of

the sample was loaded in a disposable low-volume cuvette. More than three measurements were performed on each sample. All measurements were performed at ACN concentrations of less than 10% ACN to ensure that any observed variation in particle size was not due to the solvent.

Transmission Electron Microscopy (TEM). TEM experiments were carried out on a JEOL JEM-2011 instrument at an acceleration voltage of 200 kV. The TEM sample was prepared by depositing 10 μL of the NP suspension (1.0 mg/mL) onto a 300-mesh carbon-coated copper grid. Samples were blotted away after 30 min incubation and grids were negatively stained for 20 min at the room temperature with sterile-filtered 3% (w/v) uranyl acetate aqueous solution. The grids were then washed twice with distilled water and air dried prior to imaging.

Image Acquisition. For confocal imaging, a Zeiss LSM 510 Laser Scanning Confocal microscope (Carl Zeiss MicroImaging, Inc., Thornwood, NY) was used. Microfluidic device was mounted on a thin cover slip and with corresponding tubing for inlets and outlets. A FITC solution was used for the focused stream at flow rates of 1-5 mL/min and a rhodamine solution was used for the vertical sheath streams at flow rates of 5-9 mL/min. Water stream was not labeled. For each combination of flow rates a z-stack of 165 images was taken at 0.76 mm per z-sectioning step at different regions of the channel. Lasers at 488nm and 543nm wavelengths were used together with 25x objective. For nanoparticle synthesis the experiments were performed on the device oriented on a stage of a stereomicroscope (Nikon Eclipse TE 2000U).

Simulation Methods. Two-dimensional and three-dimensional simulations were performed using COMSOL Multiphysics software, a commercial finite element package (COMSOL Inc., Burlington, MA). The flow rates at the bottom, polymer, and top inlets were 3.5, 3, and 3.5 $\mu\text{L}/\text{min}$, respectively, as were used in the experiments. After flow profiles in the channel were obtained by solving the incompressible Navier-Stokes equation, concentration profiles were

separately calculated by solving the Convection and Diffusion equation. The diffusion coefficient of the polymeric solute (PLGA_{70K}) in ACN used in the simulations ($D \sim 1.95 \times 10^{-10}$ m²/s) was based on the value estimated from the Einstein-Stokes equation (ACN viscosity ~ 0.38 cp, radius of gyration of PLGA precursors ~ 4 -5 nm) and further comparison with the data for similar molecules.

3.7. References

1. Peer, D.; Karp, J. M.; Hong, S.; Farokhzad, O. C.; Margalit, R.; Langer, R., Nanocarriers as an emerging platform for cancer therapy. *Nat Nanotechnol* **2007**, *2* (12), 751-60.
2. Riehemann, K.; Schneider, S. W.; Luger, T. A.; Godin, B.; Ferrari, M.; Fuchs, H., Nanomedicine--challenge and perspectives. *Angew Chem Int Ed Engl* **2009**, *48* (5), 872-97.
3. Davis, M. E.; Chen, Z. G.; Shin, D. M., Nanoparticle therapeutics: an emerging treatment modality for cancer. *Nat Rev Drug Discov* **2008**, *7* (9), 771-82.
4. Gref, R.; Minamitake, Y.; Peracchia, M. T.; Trubetskoy, V.; Torchilin, V.; Langer, R., Biodegradable long-circulating polymeric nanospheres. *Science* **1994**, *263* (5153), 1600-3.
5. Farokhzad, O. C.; Langer, R., Impact of nanotechnology on drug delivery. *ACS Nano* **2009**, *3* (1), 16-20.
6. Farokhzad, O. C.; Cheng, J.; Teply, B. A.; Sherifi, I.; Jon, S.; Kantoff, P. W.; Richie, J. P.; Langer, R., Targeted nanoparticle-aptamer bioconjugates for cancer chemotherapy in vivo. *Proc Natl Acad Sci U S A* **2006**, *103* (16), 6315-20.
7. Farokhzad, O. C.; Jon, S.; Khademhosseini, A.; Tran, T. N.; Lavan, D. A.; Langer, R., Nanoparticle-aptamer bioconjugates: a new approach for targeting prostate cancer cells. *Cancer Res* **2004**, *64* (21), 7668-72.
8. Gu, F.; Zhang, L.; Teply, B. A.; Mann, N.; Wang, A.; Radovic-Moreno, A. F.; Langer, R.; Farokhzad, O. C., Precise engineering of targeted nanoparticles by using self-assembled biointegrated block copolymers. *Proc Natl Acad Sci U S A* **2008**, *105* (7), 2586-91.
9. Hrkach, J.; Von Hoff, D.; Ali, M. M.; Andrianova, E.; Auer, J.; Campbell, T.; De Witt, D.; Figa, M.; Figueiredo, M.; Horhota, A.; Low, S.; McDonnell, K.; Peeke, E.; Retnarajan, B.; Sabnis, A.; Schnipper, E.; Song, J. J.; Song, Y. H.; Summa, J.; Tompsett, D.; Troiano, G.; Van Geen Hoven, T.; Wright, J.; Lorusso, P.; Kantoff, P. W.; Bander, N. H.; Sweeney, C.; Farokhzad, O. C.; Langer, R.; Zale, S., Preclinical Development and Clinical Translation of a PSMA-Targeted Docetaxel Nanoparticle with a Differentiated Pharmacological Profile. *Sci Transl Med* **2012**, *4* (128), 128ra39.
10. Murday, J. S.; Siegel, R. W.; Stein, J.; Wright, J. F., Translational nanomedicine: status assessment and opportunities. *Nanomedicine* **2009**, *5* (3), 251-73.

11. Cheng, J.; Teply, B. A.; Sherifi, I.; Sung, J.; Luther, G.; Gu, F. X.; Levy-Nissenbaum, E.; Radovic-Moreno, A. F.; Langer, R.; Farokhzad, O. C., Formulation of functionalized PLGA-PEG nanoparticles for in vivo targeted drug delivery. *Biomaterials* **2007**, *28* (5), 869-76.
12. Avgoustakis, K., Pegylated poly(lactide) and poly(lactide-co-glycolide) nanoparticles: preparation, properties and possible applications in drug delivery. *Curr Drug Deliv* **2004**, *1* (4), 321-33.
13. Karnik, R.; Gu, F.; Basto, P.; Cannizzaro, C.; Dean, L.; Kyei-Manu, W.; Langer, R.; Farokhzad, O. C., Microfluidic platform for controlled synthesis of polymeric nanoparticles. *Nano Lett* **2008**, *8* (9), 2906-12.
14. Valencia, P. M.; Basto, P. A.; Zhang, L.; Rhee, M.; Langer, R.; Farokhzad, O. C.; Karnik, R., Single-step assembly of homogenous lipid-polymeric and lipid-quantum dot nanoparticles enabled by microfluidic rapid mixing. *ACS Nano* **2010**, *4* (3), 1671-9.
15. Johnson, B. K.; Prud'homme, R. K., Mechanism for rapid self-assembly of block copolymer nanoparticles. *Phys Rev Lett* **2003**, *91* (11), 118302.
16. Wong, I.; Ho, C. M., Surface molecular property modifications for poly(dimethylsiloxane) (PDMS) based microfluidic devices. *Microfluid Nanofluidics* **2009**, *7* (3), 291-306.
17. Wu, D.; Luo, Y.; Zhou, X.; Dai, Z.; Lin, B., Multilayer poly(vinyl alcohol)-adsorbed coating on poly(dimethylsiloxane) microfluidic chips for biopolymer separation. *Electrophoresis* **2005**, *26* (1), 211-8.
18. Govender, T.; Riley, T.; Ehtezazi, T.; Garnett, M. C.; Stolnik, S.; Illum, L.; Davis, S. S., Defining the drug incorporation properties of PLA-PEG nanoparticles. *Int J Pharm* **2000**, *199* (1), 95-110.
19. Riley, T.; Stolnik, S.; Heald, C. R.; Xiong, C. D.; Garnett, M. C.; Illum, L.; Davis, S. S.; Purkiss, S. C.; Barlow, R. J.; Gellert, P. R., Physicochemical evaluation of nanoparticles assembled from poly(lactic acid)-poly(ethylene glycol) (PLA-PEG) block copolymers as drug delivery vehicles. *Langmuir* **2001**, *17* (11), 3168-3174.
20. Chan, E. M.; Alivisatos, A. P.; Mathies, R. A., High-temperature microfluidic synthesis of CdSe nanocrystals in nanoliter droplets. *J Am Chem Soc* **2005**, *127* (40), 13854-61.
21. Rolland, J. P.; Van Dam, R. M.; Schorzman, D. A.; Quake, S. R.; DeSimone, J. M., Solvent-resistant photocurable liquid fluoropolymers for microfluidic device fabrication [corrected]. *J Am Chem Soc* **2004**, *126* (8), 2322-3.
22. Huang, S. H.; Tan, W. H.; Tseng, F. G.; Takeuchi, S., A monolithically three-dimensional flow-focusing device for formation of single/double emulsions in closed/open microfluidic systems. *J Micromech Microeng* **2006**, *16* (11), 2336-2344.
23. Wolff, A.; Perch-Nielsen, I. R.; Larsen, U. D.; Friis, P.; Goranovic, G.; Poulsen, C. R.; Kutter, J. P.; Telleman, P., Integrating advanced functionality in a microfabricated high-throughput fluorescent-activated cell sorter. *Lab on a Chip* **2003**, *3* (1), 22-27.
24. Mao, X. L.; Waldeisen, J. R.; Huang, T. J., "Microfluidic drifting" - implementing three-dimensional hydrodynamic focusing with a single-layer planar microfluidic device. *Lab on a Chip* **2007**, *7* (10), 1260-1262.
25. Lim, J. M.; Kim, S. H.; Yang, S. M., Liquid-liquid fluorescent waveguides using microfluidic-drifting-induced hydrodynamic focusing. *Microfluid Nanofluid* **2011**, *10* (1), 211-217.
26. Simonnet, C.; Groisman, A., Two-dimensional hydrodynamic focusing in a simple microfluidic device. *Appl Phys Lett* **2005**, *87* (11).

27. Scott, R.; Sethu, P.; Harnett, C. K., Three-dimensional hydrodynamic focusing in a microfluidic Coulter counter. *Rev Sci Instrum* **2008**, *79* (4).
28. Kim, D. S.; Kim, D. S.; Han, K.; Yang, W., An efficient 3-dimensional hydrodynamic focusing microfluidic device by means of locally increased aspect ratio. *Microelectron Eng* **2009**, *86* (4-6), 1343-1346.
29. Chang, C. C.; Huang, Z. X.; Yang, R. J., Three-dimensional hydrodynamic focusing in two-layer polydimethylsiloxane (PDMS) microchannels. *J Micromech Microeng* **2007**, *17* (8), 1479-1486.
30. Bong, K. W.; Bong, K. T.; Pregibon, D. C.; Doyle, P. S., Hydrodynamic focusing lithography. *Angew Chem Int Ed Engl* **2010**, *49* (1), 87-90.
31. Jiang, W.; Kim, B. Y.; Rutka, J. T.; Chan, W. C., Nanoparticle-mediated cellular response is size-dependent. *Nat Nanotechnol* **2008**, *3* (3), 145-50.
32. Beletsi, A.; Panagi, Z.; Avgoustakis, K., Biodistribution properties of nanoparticles based on mixtures of PLGA with PLGA-PEG diblock copolymers. *Int J Pharm* **2005**, *298* (1), 233-41.
33. Takayama, S.; Ostuni, E.; LeDuc, P.; Naruse, K.; Ingber, D. E.; Whitesides, G. M., Subcellular positioning of small molecules. *Nature* **2001**, *411* (6841), 1016.
34. Dittrich, P. S.; Schuille, P., An integrated microfluidic system for reaction, high-sensitivity detection, and sorting of fluorescent cells and particles. *Anal Chem* **2003**, *75* (21), 5767-74.

Chapter 4 - Understanding Targeted Nanoparticles: Effects of Ligands with Different Water Solubilities on Self-Assembly and Properties of Targeted Nanoparticles

4.1. Introduction

Targeted nanoparticles (NPs), which have the capability of encapsulating different therapeutic agents and preferentially delivering them to specific tissues and cells, hold the promise of revolutionizing the treatment of many diseases including cancer, cardiovascular diseases, and immunological disorders ¹⁻⁴. With respect to cancer, NPs able to encapsulate chemotherapeutic drugs and directly deliver them to tumor cells can reduce systemic cytotoxicity caused by these agents and improve their efficacy ⁵. Among the different classes of NPs, polymeric nanoparticles have gained much attention due to several attractive properties, including biodegradability and biocompatibility of materials, favorable synthesis conditions, self-assembly in aqueous solution, and requirement of relatively little post-processing and purification work ⁶. A central challenge, however, has been the development of methods to reproducibly synthesize targeted NPs with well-characterized and optimized surface compositions. Although there are examples showing the synthesis of targeted polymeric NPs

with different targeting ligands such as the glycoprotein transferrin ⁷, HER-2 antibody ⁸, RGD peptide ⁹, and folic acid ¹⁰, it is common to see characterization and optimization of the surface ligand density underemphasized. Due to the delicate balance between the amount of targeting ligand to promote effective targeting and the protective shield (commonly conferred by poly(ethylene glycol), PEG) to avoid immune detection ¹¹, methods that enable the prediction and characterization of NP surface composition and the control of NP surface density become essential for the clinical translation of these vehicles.

Conventional methods of synthesizing polymeric targeted NPs involve use of amphiphilic block copolymers that self-assemble into drug-encapsulated NP in aqueous solution, followed by chemical conjugation of the targeting ligands to the surface of the NP ¹². Post-synthesis NP surface modification often requires the addition of excess reactant to drive the chemical reaction, and thus makes it difficult to adjust the density of TL on NP surface in a meaningfully reproducible manner. Furthermore, the post-synthesis conjugation of TL to drug encapsulated NPs is often done under aqueous condition during which there is an uncontrolled release of the drug from NPs primarily through diffusion. Consequently, the post-synthesis particle-processing methods offer limited ability to precisely engineer the NP surface properties in a robust and reproducible manner, and the targeted NPs produced by such methods may have significant batch-to-batch variations in their biophysicochemical properties. Our group recently developed a pre-functionalized biopolymer composed of hydrophobic poly(lactide-co-glycolide) (PLGA) that makes up the NP core, PEG that forms a corona-like ‘stealth’ shell, and A10 2-fluoropyrimidine RNA aptamer (Apt), which binds to the prostate-specific membrane antigen (PSMA) on the surface of prostate cancer (PCa) ¹³. This functionalized polymer possessed all

required components for a targeted NP and enabled single step self-assembly of targeted functional particles, simplifying the optimization and the potential manufacturing of the NPs ¹⁴.

Extension of this single-step self-assembly technology to other types of targeting molecules, such as peptides and small molecules with distinct solubilities and modes of action, is desired along with methods that enable the characterization and optimization of these ligands *in vitro* before embarking on *in vivo* studies. Likewise, it is of interest to understand the effect of some of the chemical properties of targeting ligands on the properties and performance of self-assembled NPs. Currently, two of the most frequently employed targeting ligands are RGD peptide, which has high water solubility (>50 mg/mL at neutral pH), and folic acid, which has a relatively poor water solubility (0.0016 mg/mL at neutral pH) ¹⁵. RGD is a small peptide that preferentially binds to integrin- $\alpha_3\beta_1$ receptor, which is often over-expressed in endothelial cells and tumor neovasculature ¹⁶. There are reports showing preparation of NPs encapsulating drugs and genes in which the RGD ligand enables preferential targeting of angiogenic tumor blood vessels, thus producing an anticancer response ¹⁷. Folic acid is a small molecule that binds to the folate receptor, which is over-expressed in some cancer cells including breast, lung, kidney, ovary, brain, among others ¹⁸. Although there are a few examples of single-step preparation of NPs using a polymer functionalized with either RGD or folic acid ^{9, 19}, previous studies lack investigation of the effects of varying ligand densities on the NP biophysicochemical properties together with characterization and optimization of the NP surface composition.

This work presents a comparison of the surface composition and targeting specificity of self-assembled RGD- and Folate-targeted NPs – two widely used TLs with different solubility

profiles. Two different biofunctional polymers composed of PLGA-PEG-RGD (high water solubility TL) and PLGA-PEG-Folate (low water solubility TL) were synthesized, and targeted NPs with different ligand densities were prepared by controlling the ratios of TL-conjugated polymers with non-conjugated PLGA-PEG lacking the TL in a nanoprecipitation process (otherwise known as solvent displacement method)^{20, 21}. The surface ligand densities of these NPs were quantified and compared to the theoretical ligand densities estimated from their initial concentrations. Finally, *in vitro* binding and uptake of these NPs against macrophages, HUVEC cells (for NP-RGD), and KB cells (for NP-Folate) was investigated to determine an optimum formulation window where NPs exhibit minimum uptake by macrophages and maximum uptake by HUVEC cells or KB cells.

4.2. Synthesis of PLGA-PEG-RGD and PLGA-PEG-Folate

Figure 4.1A outlines the synthesis procedure of PLGA-PEG-RGD and PLGA-PEG-Folate block co-polymers. The underlying principles of the synthesis of these two compounds are the same: conjugation of an amine group (NH₂) with a succinimide group in the presence of a base such as DIEA. The succinimide end group can be obtained from a carboxyl group (COOH) in the presence of EDC, such as the conversion of PLGA-COOH to PLGA-NHS. For the case of PLGA-PEG-RGD, the initial materials were the commercially available modified cyclic RGD (cRGD-PEG₄-NH₂) and tBOC-NH-PEG-NHS. For the case of PLGA-PEG-Folate, it is known that the *g*-COOH group of folic acid is more reactive when derivatized and it allows folic acid to maintain its binding properties with the folate receptor²². Therefore, modification of the *g*-COOH group of folic acid to NHS was the preferred strategy. Once folate-NHS was obtained, it was reacted with commercially available tBOC-NH-PEG-NH₂. The chemistry presented here for

the synthesis of PLGA-PEG-RGD and PLGA-PEG-Folate may allow for the conjugation of many targeting ligands (e.g. peptides, proteins, aptamers, small molecules, etc.), provided there is an available NH₂ or COOH group to be conjugated to PEG, with the PEG conjugate subsequently conjugated to PLGA.

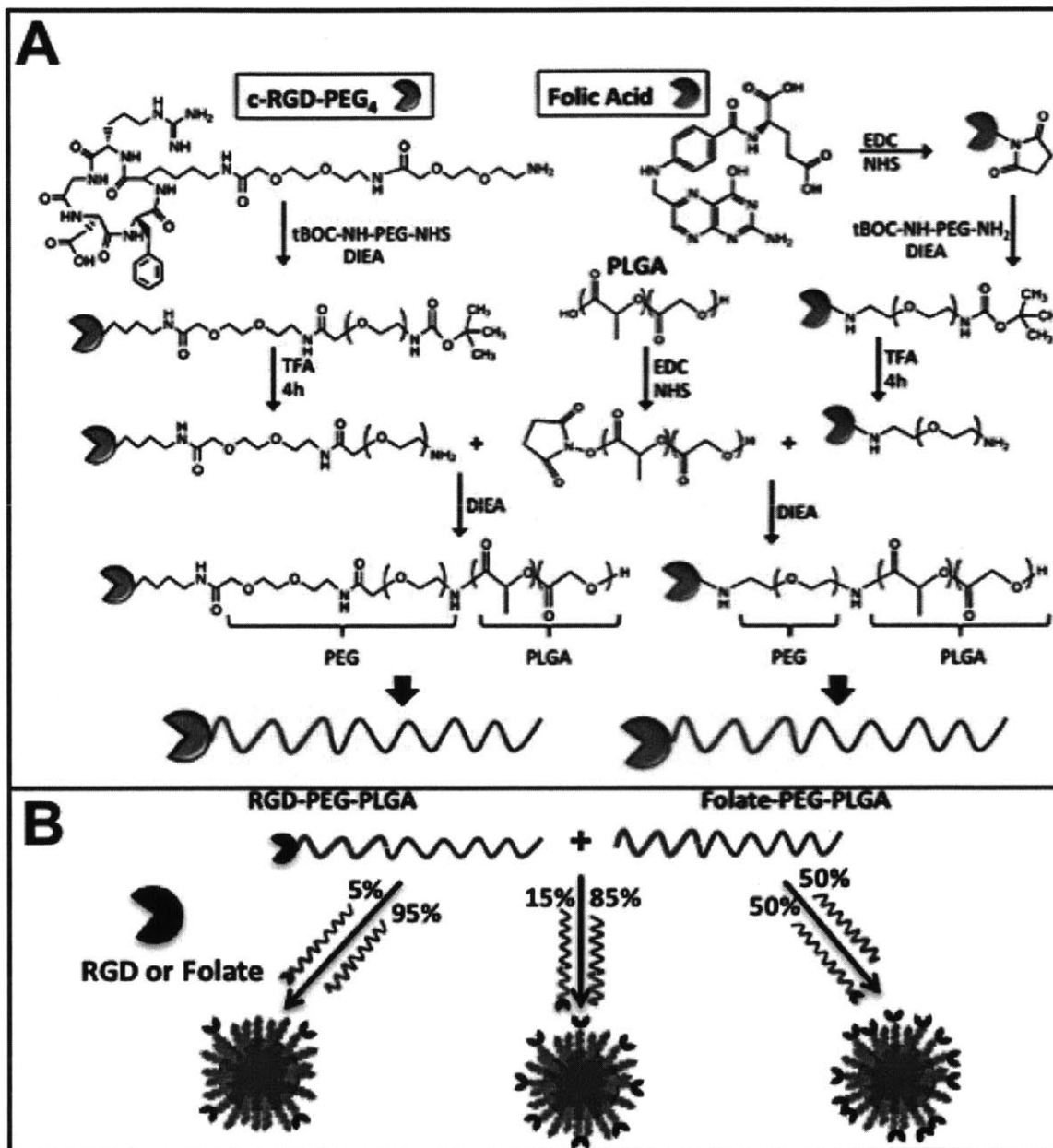


Figure 4.1. Polymer synthesis and Nanoparticle design.

(A) Synthesis of PLGA-PEG-RGD and PLGA-PEG-Folate. (B) Preparation of targeted NPs with different surface ligand densities by mixing PLGA-mPEG with functionalized PLGA-PEG-TL.

4.3. Synthesis of RGD- and folate-targeted NPs

RGD and folate-targeted NPs were formulated by dissolving PLGA-PEG-RGD or PLGA-PEG-Folate copolymers with PLGA-mPEG in acetonitrile followed by precipitation in water. Ligand density was varied by using different percentages of TL-conjugated polymers in the total polymer formulation (Figure 4.1B). In principle, the resulting NPs are composed of a PLGA hydrophobic core, in which hydrophobic drugs can be encapsulated, and a PEG hydrophilic corona-like shell decorated with targeting moieties. The single-step synthesis eliminates conjugation steps after particle preparation and enhances batch-to-batch reproducibility. Prepared targeted NPs were characterized using DLS to measure size and surface zeta potential, and TEM to observe NP morphology and confirm size.

For NP-RGD it was observed that as the amount of PLGA-PEG-RGD was increased in the formulation, the surface zeta potential remained close to neutral, which was expected since PLGA-mPEG has a charge-neutral methoxy end group and RGD in PLGA-PEG-RGD is also neutral at a pH of 7.4²³ (Figure 4.2A). A similar effect was observed for NP-Folate (Figure 4.2B). From DLS measurements, NP-RGD had a constant size of ~50 nm for formulations with 0%, 7%, and 22% PLGA-PEG-RGD. For formulations with 50%, and 74% of PLGA-PEG-RGD a gradual size increase of the NP was observed to 66 nm and 73 nm, respectively (Figure 4.2C). For NP-Folate, as the amount of PLGA-PEG-Folate was increased, size increase of NPs was observed for each formulation: 50 nm at 0%, 60 nm at 7%, 76 nm at 22%, 96 nm at 50% and 122 nm at 74% of PLGA-PEG-Folate (Figure 4.2D). Considering that both functionalized polymers PLGA-PEG-RGD and PLGA-PEG-Folate had the similar molecular weight according to GPC (

Mn = 50,005 Da and 49,551 Da, respectively) and the PLGA-mPEG of same MW was used for both NP formulations, this disparity in size for NP-Folate suggests that the effect is due to the differences between folate and RGD (i.e. presence of folate affects self-assembly). TEM images of both targeted NPs at a composition of 7% TL-conjugated polymer showed homogenous populations of NPs with minimal particle-particle aggregation (Figure 4.2E for NP-RGD and Figure 4.2F for NP-Folate).

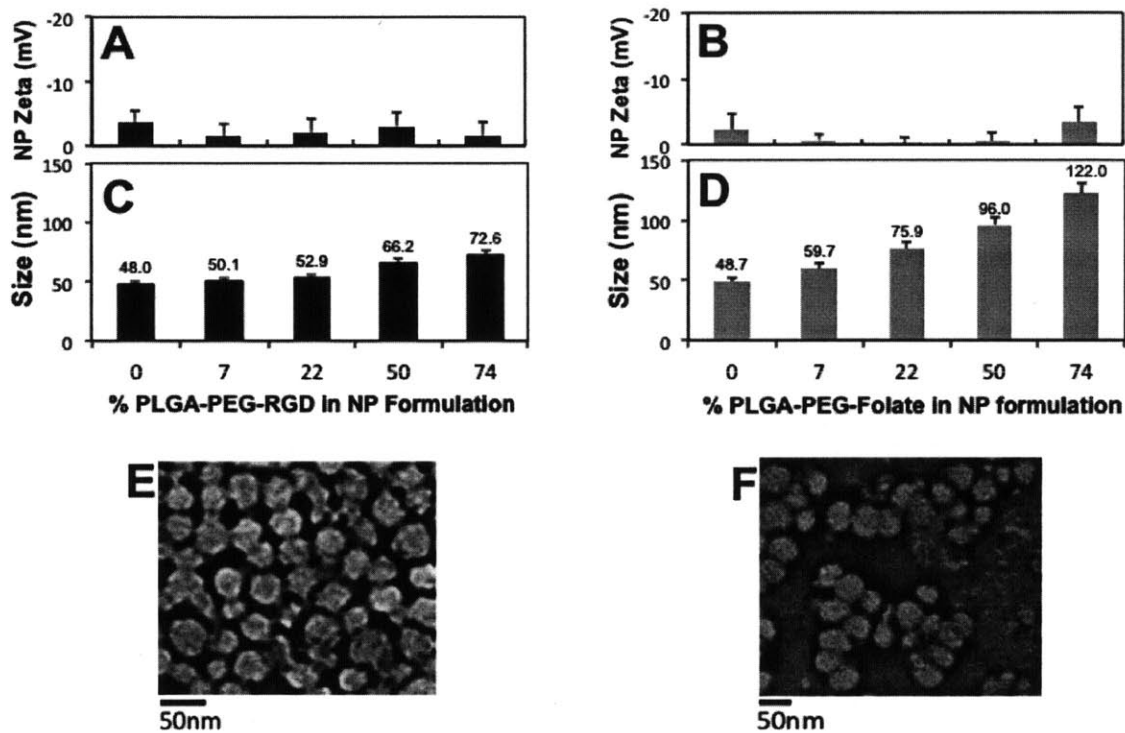


Figure 4.2 Characterization of targeted NP-RGD and NP-Folate.

Zeta Potential (A,B) Size (C, D) and TEM micrographs (E,F). Error bars represent standard deviation of n = 3 samples.

4.4. NP-RGD and NP-Folate ligand densities

To investigate the effect of targeting ligand hydrophobicity on the surface composition of NPs, we determined the percentage of the initial RGD or Folate in the form of PLGA-PEG-RGD

and PLGA-PEG-folate present on the surface of the NP in solution. For the case of NP-RGD we used the Lava Prep Peptide assay, a fluorescence-based method capable of detecting lysine, arginine, and histidine on peptides. For NP-Folate we first incubated the NPs with folate antibodies, followed by a washing step to remove excess antibody. Finally, we used Low BCA protein assay to determine the amount of antibody (and hence the corresponding amount of folate) on the NP surface. For the case of NP-RGD, all of the RGD present in the form of PLGA-PEG-RGD was detected on the NP surface (Figure 4.3A). For the cases of 75% and 100% RGD, the average fraction of starting RGD presented on the NP surface appeared to be 0.93 and 0.89, respectively. We believe that at large percentages of PLGA-PEG-RGD there might be an overlap of RGD molecules that result on the NP surface which may limit the detection accuracy of the assay, though for percentages of PLGA-PEG-RGD below 75% this ligand overlap may not occur. In contrast, for NP-Folate a maximum of 21% of the folate in the form of PLGA-PEG-Folate was detected on the NP surface for all formulations (Figure 4.3B). Although the accuracy of this assay may be compromised at high concentrations of PLGA-PEG-Folate due to steric hindrance of antibodies on the NP surface, results were found to be reliable for PLGA-PEG-Folate percentages below 74% at the given NP sizes, since others have detected ~ 4 times the number of antibodies we found on NPs of similar size²⁴.

From these results, we hypothesize that the poor water solubility of folate ligands causes interactions of folate and PLGA when PLGA-PEG-Folate self-assembles into a NP, resulting in a significant fraction of folate buried in the core of the NP. Conversely, because RGD has high water solubility, it interacts minimally with PLGA and has minimum thermodynamic drive to enter the hydrophobic core of the NP. The hypothesis that a significant fraction of folate molecules from PLGA-PEG-Folate result in the NP core, may explain the larger NP size

observed for higher fractions of PLGA-PEG-Folate. The low water solubility of folate may present a lower barrier to polymer and NP aggregation during self-assembly of the NPs, resulting in larger NPs with cores that are more loosely packed due to inclusion of PEG-Folate blocks of PLGA-PEG-Folate into the NP core. A similar increase size of NPs formed by nanoprecipitation was observed previously when PLGA was added to PLGA-PEG prior to nanoprecipitation ²⁵.

Knowing the size and size distribution of the targeted NPs and assuming an estimated NP density of 1.27 mg/mL ²⁶, we calculated the ligand density (number of ligands per mm² of NP surface) and the number of ligands per NP. Figures 4.3C and 4.3D show the theoretical, or expected, ligand densities calculated assuming 100% of ligands used in NP formulation are presented on the particle surface, as well as the experimentally determined amount of targeting ligands detected on the particle surface. For the case of NP-RGD, as the amount of PLGA-PEG-RGD was increased, the NP ligand density increased, and the observed ligand densities correlated well with the theoretical calculations. For NP formulations with 5%, 10%, 16%, 22%, 50%, 76% and 100% of PLGA-PEG-RGD the average number of RGD molecules on the surface of the NP were calculated to be 45, 97, 144, 230, 1030, 2270, and 3731, respectively (Figure 4.3E). Similarly, for the case of NP-Folate, as the amount of PLGA-PEG-Folate was increased, the NP ligand density also increased but the theoretical ligand densities did not correlate well the experimentally determined values. With 7%, 22%, 50%, and 74% of PLGA-PEG-Folate in the initial formulations, NPs were expected to have 107, 632, 2707, and 12127 ligands on their surface; however, only 23, 89, 368, and 1874 ligands, respectively, were detected on the surface (Figure 4.3F). The reduced presence of folate on the surface of the particle may have potential repercussions on the targeting capabilities of these NPs, which needs to be accounted for future experimental design. These results highlight the importance of considering the chemical

properties of targeting ligands, such as solubility, as factors that may affect the single-step self-assembly of targeted NPs.

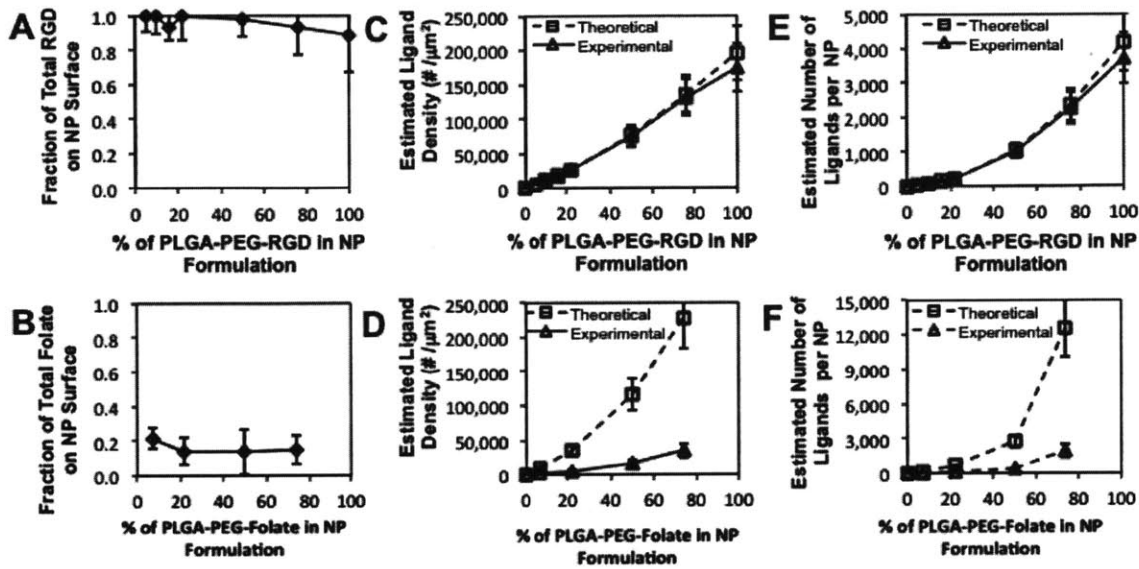


Figure 4.3. Quantification of targeted NP surface composition.

(A) Fraction of initial RGD that resulted on the NP surface. (B) Fraction of initial folate that resulted on the NP surface. (C) Estimated ligand Densities and (E) estimated number of ligands per NP of NP-RGD as a function of the percentage of PLGA-PEG-RGD in formulation. (D) Estimated ligand Densities and (F) estimated number of ligands per NP of NP-Folate as a function of the percentage of PLGA-PEG-Folate in formulation. Theoretical (\square) and experimental (Δ). Error bars represent standard deviation in $n = 8$ samples for NP-RGD and $n = 4$ samples for NP-Folate.

4.5. Cellular binding and uptake of targeted nanoparticles

To examine the effect of ligand solubility on NP self-assembly and surface composition, recognition of NPs by macrophages and their targeting capabilities to cell models with over-expressed ligand receptors was investigated *in vitro*. Phagocytosis of NPs by macrophages depends both on the size and the surface characteristics of the particle²⁷. For instance, hydrophobic surfaces induce opsonization of NPs, which promotes NP phagocytosis^{27, 28}.

Conversely, PEG-functionalized and hydrophilic surfaces reduce NP uptake by macrophages²⁹.

. We investigated the binding and uptake of RGD- and Folate-targeted NPs by macrophages as the fraction of RGD or folate biofunctional copolymer was varied. Flow cytometry was used to measure the association of NPs with macrophages, with 2.5% PLGA-Alexa488 added to the NP formulations as a fluorescent reporter. In the case of NP-RGD, it was observed that as the amount of PLGA-PEG-RGD was increased, there was no increase in uptake by macrophages when compared to non-targeted (i.e. fully PEG-functionalized) NPs, with the exception of NPs composed of 74% PLGA-PEG-RGD, which showed an almost 3-fold increase in uptake (Figure 4A). Although RGD is not known to be immunogenic³⁰, the disruption of the outer layer of the PEG shell at high RGD surface densities might induce an increase in phagocytosis. In contrast, for the case of NP-Folate, as the PLGA-PEG-Folate was increased, an augment in binding and uptake by macrophages was observed. Specifically, for NPs composed of 7%, 22%, 50% and 74% PLGA-PEG-Folate, a 2.0, 3.8, 4.7, and 8.5-fold increase in phagocytosis was observed, respectively (Figure 4.4B). It has been shown that NPs of larger size are more readily taken up by macrophages³¹, and hence the observed increase in macrophage uptake could be due an increase in NP size. Alternatively, this increase in uptake may be due to the low hydrophilicity of folate, which may induce opsonization of the NP surface. Finally, some reports have shown that NP-Folate target activated macrophages since they have over-expressed folate receptors^{22, 32}.

We determined the targeting capabilities of the nanoparticles with RGD and folate at different densities. We measured the binding and uptake of NP-RGD by HUVEC cells, which was taken as a model cell line with integrin- α 3 receptor over-expressed on the cell membrane. Similarly, binding and uptake of NP-Folate was investigated using KB cells, used as a model cell line with folate receptor over-expressed on the cell membrane. Flow cytometry was used to

measure the association of NPs with HUVEC and KB cells, with 2.5% PLGA-Alexa488 added to the NP formulations as a fluorescent reporter. Increase in the amount of PLGA-PEG-RGD in the NP formulation (which correlates with a higher number of RGD molecules per NP) resulted in a corresponding increase in fluorescence associated with HUVEC cells up to ~200-fold when compared to non-targeted NPs (Figure 4.4C). The increase in RGD molecules on the NP surface may induce multivalent interactions with the integrin receptors in HUVEC cells leading to increased NP binding and uptake. On the other hand, for the case of NP-Folate, when the amount of PLGA-PEG-Folate was increased from 0% to 7%, to 22%, only marginal increase in uptake by KB cells was observed (Figure 4.4D). Only at 50% and 74% of PLGA-PEG-Folate was a substantial increase in uptake observed, with increase in fluorescence associated with the cells of approximately 4- and 9-fold, respectively, compared to non-targeted NPs. As mentioned before, we hypothesize that during self-assembly of PLGA-PEG-Folate and PLGA-mPEG into a NP, only ~20% of the folate ends up on the NP surface (Figure 4.3B) and the rest is embedded in the NP core due to interactions with PLGA. Thus, the amount of folate on the surface of the NPs may not be sufficient to significantly increase the uptake by KB cells for formulations with 7% and 22% of PLGA-PEG-Folate. The NP surface folate concentration was sufficient to elicit a significant increase in uptake by KB cells only when > 50% PLGA-PEG-Folate was used in NP formulation.

From these results one can determine optimal NP candidates for future experiments. For the case of NP-RGD, formulations composed of up to 50% PLGA-PEG-RGD could be used since they experienced marginal phagocytosis compared to non-targeted NPs and a ~70-fold increase in fluorescence when exposed to HUVEC cells. In contrast, for NP-Folate only those formulations with ~50% PLGA-PEG-Folate could be used since below this percentage only

modest targeting effects were observed and above this percentage increased phagocytosis was observed. Microscopy images presented in figures 4.4E and 4.4F show that non-targeted NPs do not enter, or minimally enter, the cell while targeted NP-RGD and NP-Folate composed 50% TL-conjugated polymer readily enter HUVEC cells and KB cells, respectively. NP formulations with narrower ranges of the fraction of TL-conjugated biopolymer together with other *in vitro* experiments that investigate complement activation³³, cell cytotoxicity³⁴, among other factors³⁵, could be carried out to narrow the window of optimal NP candidates for *in vivo* experiments.

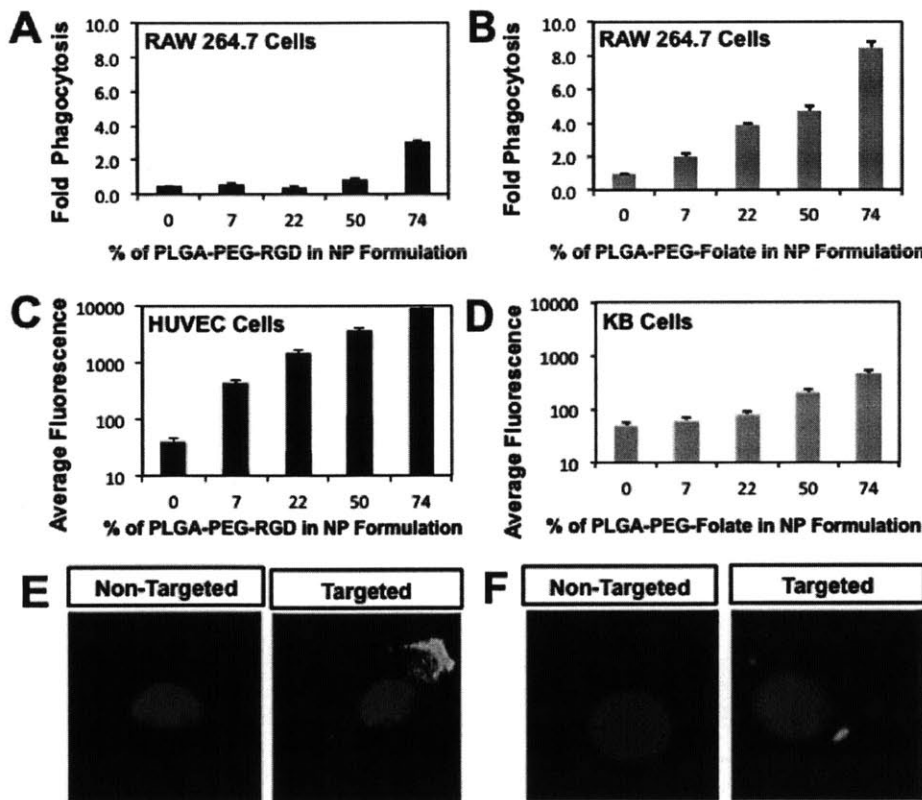


Figure 4.4. Cellular binding and uptake of targeted NPs as a function of % of functionalized PLGA-PEG added in the NP formulation.

(A) RGD targeted PLGA-PEG NPs and (B) Folate-targeted PLGA-PEG NPs. (C) Association of NP-RGD with HUVEC cells. (D) Association of NP-Folate with KB cells. (E) Representative images of non-targeted and NP-RGD (at 50% of PLGA-PEG-RGD) uptake by HUVEC cells.

(F) Representative images of non-targeted and NP-Folate (at 50% PLGA-PEG-Folate) uptake by KB cells. Error bars represent standard deviation in n = 3 samples.

4.6. Conclusion

In conclusion, we synthesized PLGA-PEG copolymers functionalized with either folic acid (a ligand with poor water solubility) or RGD peptide (a ligand with high water solubility), for single-step preparation of targeted polymeric nanoparticles. By mixing PLGA-PEG-RGD or PLGA-PEG-Folate with PLGA-mPEG at different ratios we were able to prepare NPs with varying surface ligand densities. The surface of the targeted NPs was characterized, demonstrating that all of the RGD included in the form of PLGA-PEG-RGD was present on the surface of the NP-RGD while only ~20% of the folate in the form PLGA-PEG-Folate was found on the NP-Folate surface. Uptake of targeted NPs by macrophages was investigated showing that NP-Folate was increasingly taken up as the amount of PLGA-PEG-Folate in the formulation was increased, while NP-RGD experienced minimum phagocytosis even at 50% PLGA-PEG-RGD. Finally, we studied the association of NP-RGD with HUVEC cells and NP-Folate with KB cells showing that as the concentration of PLGA-PEG-RGD in the NP-RGD formulation was increased a corresponding increase in uptake was observed, while NP-Folate only showed significant targeting at ~50% PLGA-PEG-Folate. These studies provide insight into the behavior of targeted NPs prepared in a single-step with TLs of different solubilities and show an *in vitro* experimental design for finding NPs with favorable targeting ligand density.

4.7. Materials and methods

Materials: Poly(D,L-lactide-co-glycolide)-co-Poly(ethylene glycol) with terminal methoxy groups (PLGA_{27K}-mPEG_{5K}) was obtained from Boehringer Ingelheim (Ingelheim am Rhein, Germany). Poly(D,L-lactide-co-glycolide) (50/50) with terminal carboxylate groups (PLGA, inherent viscosity 0.67 dL/g, MW ~ 45 kDa) was obtained from Lactel (Pelham, AL, USA). tBOC-NH-PEG-NH₂ (MW 5000) and tBOC-NH-PEG-NHS, (MW 5000) were purchased from Laysan Bio, Inc (Arab, AL, USA). cRGD-PEG₄ peptide was obtained from Peptides International (Louisville, KY, USA) and Folic Acid from Sigma-Aldrich (St. Louis, MO, USA). Molecular biology buffers and tissue culture reagents were purchased from Invitrogen (Carlsbad, CA, USA). KB cell line was obtained from American Type Culture Collection (Manassas, VA, USA), and HUVEC cell line together with its growth medium was purchased from Lonza, Inc (Allendale, NJ, USA).

Synthesis of PLGA-PEG-RGD: The synthesis of PLGA_{45K}-PEG_{5K}-RGD was accomplished first by the conjugation of a modified cyclic RGD to PEG followed by the conjugation of the resultant RGD-PEG to PLGA. First, cRGD-PEG₄ (Arg-Gly-Asp-D-Phe-Lys-PEG₄) (8 mg, 8.94 mmol) was dissolved in 400 mL of dimethylformamide (DMF) and reacted with tBOC-NH-PEG-NHS (22 mg, 4.47 mmol) and N,N-Diisopropylethylamine (DIEA, 10 mL) for 12 h. The reaction product was dialyzed 24 h in water to remove unreacted RGD. The resultant tBOC-PEG-RGD was lyophilized and reconstituted in 400 mL of *trifluoroacetic acid* (TFA) to remove the protecting group. After 4 h of reaction, product was dried under vacuum and dissolved in 200 mL of DMSO. Concurrently, PLGA-COOH (100 mg, 2.22 mmol) was reacted with N-hydroxysuccinimide (NHS) in the presence of 1-Ethyl-3-[3-dimethylaminopropyl] carbodiimide (EDC) in dichloromethane (DCM) for 2 h. PLGA-NHS was dried under vacuum and dissolved

in 300 mL of DMSO. Finally, PEG-RGD and PLGA-NHS in DMSO were mixed with DIEA, allowed to react for 24 h, precipitated in ice cold methanol, and dried under vacuum. PLGA-PEG-RGD was characterized with GPC to confirm the presence of the triblock PLGA-PEG-RGD. To verify conjugation of PEG to RGD Maldi-TOF was used, and it showed that only PEG-RGD was present while free RGD was absent (see supporting information).

Synthesis of PLGA-PEG-Folate. The synthesis of PLGA_{45K}-PEG_{5K}-Folate was accomplished first by the conjugation of an activated Folate-NHS to PEG followed by the conjugation of the resultant Folate-PEG to PLGA. First, Folic acid (60 mg, 0.14 mmol) was dissolved in 2mL of DMF and reacted with NHS in the presence of EDC for 12 h. Folate-NHS was precipitated in a mixture of 30/70 acetone/diethyl ether and dried under vacuum. Dry Folate-NHS was dissolved in 500 mL of DMSO and reacted with tBOC-NH-PEG-NH₂ (92.4 mg, 28 mmol) for 12 h in the presence of DIEA. The reaction product was then precipitated under cool ether, reconstituted in an aqueous solution of NaOH and dialyzed for 48 h. The resultant tBOC-PEG-Folate was lyophilized and reconstituted in 700 mL of TFA to remove the protecting group. After 4 h of reaction, the solution was dried under vacuum and then dissolved in 500 mL of DMSO. Concurrently, PLGA-COOH (420 mg, 9.33 mmol) was reacted with NHS under the presence of EDC in DCM for 2 h. PLGA-NHS was dried under vacuum and dissolved in 500 mL of DMSO. Finally, PEG-folate and PLGA-NHS in DMSO were mixed and allowed to react for 24 h. The final product was precipitated in ice cold methanol and dried under vacuum. PLGA-PEG-Folate was characterized with NMR to verify the conjugation of PLGA to PEG, and GPC to confirm the presence of PLGA-PEG-Folate. To verify conjugation of PEG to folate Maldi-TOF was used, and it showed that only PEG-folate was present while free folate was absent. Finally to quantify the amount of PLGA-PEG-Folate compared to PEG-folate, UV-VIS was used and it was found

that 98% of the final reaction product was PLGA-PEG-Folate and 2% PEG-Folate (see appendix 3)

Synthesis of PLGA-Alexa-488. The synthesis of PLGA_{45K}-Alexa488 was accomplished by the conjugation of an activated PLGA-COOH with Alexa-488 Cadaverin through EDC/NHS conjugation. First, 1mg of Alexa-488 was dissolved in 1 mL of DMF. Concurrently, PLGA-COOH (50 mg, 1.1 mmol) was mixed with EDC and NHS in 500 mL of DMF. Finally, PLGA solution was reacted with Alexa-488 solution for 16 h at room temperature. The reaction product was precipitated in ice cold methanol and dried under vacuum.

Synthesis and Characterization of NPs. NPs were prepared by the nanoprecipitation method^{20, 21}. In brief, PLGA-mPEG was mixed with a predefined amount of PLGA-PEG-Folate or PLGA-PEG-RGD and PLGA-Alexa488 in acetonitrile to a final polymer concentration of 10 mg/mL. For all experiments the weight percent of PLGA-Alexa488 in the polymer mixture was fixed to 2.5%. At this concentration, PLGA-Alexa488 did not affect the size and zeta potential of the NPs and was readily detected by FACS. For each NP formulation, 200 mL of the polymer mixture was added drop-wise to water with constant stirring, giving a final NP concentration of 1 mg/ml. The NPs were stirred for 2 h, and the remaining organic solvent was removed by washing the NPs three times using an Amicon centrifugation filtration membrane. *Particle sizing* was performed using dynamic light scattering (DLS) with a Zetasizer Nano ZS instrument (Malvern Instruments Ltd., U.K.). For each measurement, 100 μ L or more of the sample was loaded in a disposable low-volume cuvette. The NP surface *zeta potential* was measured using the same instrument used for the size measurements. For each measurement, particles were washed with water and reconstituted in 1 mL of 1x PBS (0.5 mg/mL). *TEM* experiments were carried out on a JEOL 2011 instrument at an acceleration voltage of 200 kV. The TEM sample was prepared by

depositing 10 μ L of the NP suspension (1.0 mg/mL) onto a 200-mesh carbon-coated copper grid. Samples were blotted away after 30 min incubation and grids were negatively stained for 20 min at room temperature with sterile-filtered 2% (w/v) uranyl acetate aqueous solution.

Quantification of RGD and Folate on Nanoparticle Surface Detection and quantification of RGD on the surface of the NP was accomplished using the Lava Prep Fluorescence-based Peptide Quantification Kit (Gel Company Inc, San Francisco, CA, USA). Briefly, NP-RGD were prepared and washed three times with DI water to a final concentration of 1mg/mL. Then, 100 mL of NP solution was mixed with 100 mL of the assay working solution and incubated for 60 minutes under dark. Fluorescence of the resulting solution was measured using a PerkinElmer plate reader VICTOR3 (Waltham, MA, USA) according to manufacturer's instructions. Using a calibration curve of free cRGD-PEG₄, the amount of RGD present in solution was determined. Each assay was repeated 3 times (each with n = 8 samples) and the average value was taken as the representative.

Detection and quantification of folate on the NP surface was accomplished first by incubating NP-Folate with folate antibodies and then determining the amount of antibody using the Low Protein BCA Assay (Lamda Biotech Inc, St. Louis, MO, USA). Briefly, NP-Folate was prepared and washed three times with DI water and re-suspended in PBS to a final concentration of 1 mg/mL. Then, 5 mL of NP solution was mixed with 95 mL of excess folate antibody in PBS, and the resultant solution incubated for 2 h with slow shaking. After 2 h, excess antibody was removed by washing the NP solution 3 times using a 300 kDa cutoff centrifugal filter. The final product was re-suspended in 100 mL of PBS followed by the addition of 100 mL of BCA working solution. The resultant solution was heated at 60 °C for 30 minutes and analyzed using a UV spectrophotometer according to the manufacturer's instructions. Using a calibration curve of

free folate antibody, the amount of folate present in the NP solution was determined. Each assay was repeated 5 times (each with $n = 4$ samples) and the average value was taken as the representative. Low BCA assays were done on free antibody solutions before and after centrifugal filtration to verify that no antibody remained left on the filter and that the initial amount was recovered after filtration.

NP Binding and Uptake by RAW264.7, KB and HUVEC cells RAW 264.7 cells were cultured in DMEM medium with 10% fetal bovine serum, 50 units/mL penicillin and 50 mg/mL streptomycin. KB cells were cultured in Folate-free RPMI medium with 10% fetal bovine serum, 50 units/mL penicillin and 50 mg/mL streptomycin. HUVEC cells were cultured in EGM-2 BulleKit medium. All cells were cultured at 37 °C and 5% CO₂. Cells were seeded at a density of 50,000 cells per well on a 24-well plate. After 24 h, the cell medium was removed and replaced with NPs dissolved in the same medium at a concentration of 1 mg/mL. Cells and NPs were incubated for 4 h for the case of RAW 264.7 and HUVEC cells and 6 h for case of KB cells followed by three washes with 1% BSA solution in PBS to remove excess NPs. RAW264.7 cells were removed from the plate using a cell scraper and centrifuged, while KB and HUVEC cells were treated with trypsin, removed from the plate, and centrifuged. The resultant cell pellets were reconstituted in 250uL of PBS and placed on a 96-well plate for FACS analysis. Flow cytometry analysis was performed on a BD Biosciences LSR II with High-Throughput sampler (HTS) option, with 10,000 cells were collected for each measurement.

Microscopy of Cells. For fluorescence microscopy studies, KB or HUVEC cells were seeded on a four-well chamber slide with 20,000 cells/well and incubated at 37°C and 5% CO₂ for 24 h. Next, the cells were incubated in fresh complete medium with NPs. After incubation, cells were washed three times in PBS and fixed in 4% paraformaldehyde at room temperature. For imaging,

slides were mounted with a coverslip using H-1000 Vectorshield mounting medium with DAPI.

Fluorescence imaging was carried out using a Zeiss Fluorescence Microscope.

4.8. References

1. Riehemann, K.; Schneider, S. W.; Luger, T. A.; Godin, B.; Ferrari, M.; Fuchs, H., Nanomedicine--challenge and perspectives. *Angew Chem Int Ed Engl* **2009**, *48* (5), 872-97.
2. Mamo, T.; Moseman, E. A.; Kolishetti, N.; Salvador-Morales, C.; Shi, J.; Kuritzkes, D. R.; Langer, R.; von Andrian, U.; Farokhzad, O. C., Emerging nanotechnology approaches for HIV/AIDS treatment and prevention. *Nanomedicine (Lond)* **2010**, *5* (2), 269-85.
3. Mulder, W. J.; Fayad, Z. A., Nanomedicine captures cardiovascular disease. *Arterioscler Thromb Vasc Biol* **2008**, *28* (5), 801-2.
4. Farokhzad, O. C., Nanotechnology for drug delivery: the perfect partnership. *Expert Opin Drug Deliv* **2008**, *5* (9), 927-9.
5. Davis, M. E.; Chen, Z. G.; Shin, D. M., Nanoparticle therapeutics: an emerging treatment modality for cancer. *Nat Rev Drug Discov* **2008**, *7* (9), 771-82.
6. Gref, R.; Minamitake, Y.; Peracchia, M. T.; Trubetskoy, V.; Torchilin, V.; Langer, R., Biodegradable long-circulating polymeric nanospheres. *Science* **1994**, *263* (5153), 1600-3.
7. Davis, M. E.; Zuckerman, J. E.; Choi, C. H.; Seligson, D.; Tolcher, A.; Alabi, C. A.; Yen, Y.; Heidel, J. D.; Ribas, A., Evidence of RNAi in humans from systemically administered siRNA via targeted nanoparticles. *Nature* **2010**, *464* (7291), 1067-70.
8. Alexis, F.; Basto, P.; Levy-Nissenbaum, E.; Radovic-Moreno, A. F.; Zhang, L.; Pridgen, E.; Wang, A. Z.; Marein, S. L.; Westerhof, K.; Molnar, L. K.; Farokhzad, O. C., HER-2-targeted nanoparticle-affibody bioconjugates for cancer therapy. *ChemMedChem* **2008**, *3* (12), 1839-43.
9. Danhier, F.; Lecouturier, N.; Vroman, B.; Jerome, C.; Marchand-Brynaert, J.; Feron, O.; Preat, V., Paclitaxel-loaded PEGylated PLGA-based nanoparticles: in vitro and in vivo evaluation. *J Control Release* **2009**, *133* (1), 11-7.
10. Pan, J.; Liu, Y.; Feng, S. S., Multifunctional nanoparticles of biodegradable copolymer blend for cancer diagnosis and treatment. *Nanomedicine (Lond)* **2010**, *5* (3), 347-60.
11. Pirollo, K. F.; Chang, E. H., Does a targeting ligand influence nanoparticle tumor localization or uptake? *Trends Biotechnol* **2008**, *26* (10), 552-8.
12. Kolishetti, N.; Dhar, S.; Valencia, P. M.; Lin, L. Q.; Karnik, R.; Lippard, S. J.; Langer, R.; Farokhzad, O. C., Engineering of self-assembled nanoparticle platform for precisely controlled combination drug therapy. *Proc Natl Acad Sci U S A* **2010**, *107* (42), 17939-44.
13. Gu, F.; Zhang, L.; Teply, B. A.; Mann, N.; Wang, A.; Radovic-Moreno, A. F.; Langer, R.; Farokhzad, O. C., Precise engineering of targeted nanoparticles by using self-assembled biointegrated block copolymers. *Proc Natl Acad Sci U S A* **2008**, *105* (7), 2586-91.
14. Farokhzad, O. C.; Langer, R., Impact of nanotechnology on drug delivery. *ACS Nano* **2009**, *3* (1), 16-20.

15. Wu, Z.; Li, X. X.; Hou, C. Y.; Qian, Y., Solubility of Folic Acid in Water at pH Values between 0 and 7 at Temperatures (298.15, 303.15, and 313.15) K. *Journal of Chemical and Engineering Data* **2010**, *55* (9), 3958-3961.
16. Desgrosellier, J. S.; Cheresh, D. A., Integrins in cancer: biological implications and therapeutic opportunities. *Nat Rev Cancer* **2010**, *10* (1), 9-22.
17. Murphy, E. A.; Majeti, B. K.; Barnes, L. A.; Makale, M.; Weis, S. M.; Lutu-Fuga, K.; Wrasidlo, W.; Cheresh, D. A., Nanoparticle-mediated drug delivery to tumor vasculature suppresses metastasis. *Proc Natl Acad Sci U S A* **2008**, *105* (27), 9343-8.
18. Low, P. S.; Antony, A. C., Folate receptor-targeted drugs for cancer and inflammatory diseases. *Adv Drug Deliv Rev* **2004**, *56* (8), 1055-8.
19. Patil, Y. B.; Toti, U. S.; Khair, A.; Ma, L.; Panyam, J., Single-step surface functionalization of polymeric nanoparticles for targeted drug delivery. *Biomaterials* **2009**, *30* (5), 859-66.
20. Avgoustakis, K., Pegylated poly(lactide) and poly(lactide-co-glycolide) nanoparticles: preparation, properties and possible applications in drug delivery. *Curr Drug Deliv* **2004**, *1* (4), 321-33.
21. Cheng, J.; Teply, B. A.; Sherifi, I.; Sung, J.; Luther, G.; Gu, F. X.; Levy-Nissenbaum, E.; Radovic-Moreno, A. F.; Langer, R.; Farokhzad, O. C., Formulation of functionalized PLGA-PEG nanoparticles for in vivo targeted drug delivery. *Biomaterials* **2007**, *28* (5), 869-76.
22. Sudimack, J.; Lee, R. J., Targeted drug delivery via the folate receptor. *Adv Drug Deliv Rev* **2000**, *41* (2), 147-62.
23. Ghandehari, H.; Sharan, R.; Rubas, W.; Killing, W. M., Molecular modeling of arginine-glycine-aspartic acid (RGD) analogs: relevance to transepithelial transport. *J Pharm Pharm Sci* **2001**, *4* (1), 32-41.
24. Jiang, W.; Kim, B. Y.; Rutka, J. T.; Chan, W. C., Nanoparticle-mediated cellular response is size-dependent. *Nat Nanotechnol* **2008**, *3* (3), 145-50.
25. Karnik, R.; Gu, F.; Basto, P.; Cannizzaro, C.; Dean, L.; Kyei-Manu, W.; Langer, R.; Farokhzad, O. C., Microfluidic platform for controlled synthesis of polymeric nanoparticles. *Nano Lett* **2008**, *8* (9), 2906-12.
26. Vauthier, C.; Schmidt, C.; Couvreur, P., Measurement of the density of polymeric nanoparticulate drug carriers by isopycnic centrifugation. *J Nanoparticle Res* **1999**, *1*, 411-418.
27. Owens, D. E., 3rd; Peppas, N. A., Opsonization, biodistribution, and pharmacokinetics of polymeric nanoparticles. *Int J Pharm* **2006**, *307* (1), 93-102.
28. Alexis, F.; Pridgen, E.; Molnar, L. K.; Farokhzad, O. C., Factors affecting the clearance and biodistribution of polymeric nanoparticles. *Mol Pharm* **2008**, *5* (4), 505-15.
29. van Vlerken, L. E.; Vyas, T. K.; Amiji, M. M., Poly(ethylene glycol)-modified nanocarriers for tumor-targeted and intracellular delivery. *Pharm Res* **2007**, *24* (8), 1405-14.
30. Gaillard, C.; Duval, M.; Dumortier, H.; Bianco, A., Carbon nanotube-coupled cell adhesion peptides are non-immunogenic: a promising step toward new biomedical devices. *J Pept Sci* **2010**, *17* (2), 139-42.
31. Epstein-Barash, H.; Gutman, D.; Markovsky, E.; Mishan-Eisenberg, G.; Koroukhov, N.; Szebeni, J.; Golomb, G., Physicochemical parameters affecting liposomal bisphosphonates bioactivity for restenosis therapy: internalization, cell inhibition, activation of cytokines and complement, and mechanism of cell death. *J Control Release* **2010**, *146* (2), 182-95.

32. Turk, M. J.; Waters, D. J.; Low, P. S., Folate-conjugated liposomes preferentially target macrophages associated with ovarian carcinoma. *Cancer Lett* **2004**, *213* (2), 165-72.
33. Aggarwal, P.; Hall, J. B.; McLeland, C. B.; Dobrovolskaia, M. A.; McNeil, S. E., Nanoparticle interaction with plasma proteins as it relates to particle biodistribution, biocompatibility and therapeutic efficacy. *Adv Drug Deliv Rev* **2009**, *61* (6), 428-37.
34. Dobrovolskaia, M. A.; McNeil, S. E., Immunological properties of engineered nanomaterials. *Nat Nanotechnol* **2007**, *2* (8), 469-78.
35. Dobrovolskaia, M. A.; Aggarwal, P.; Hall, J. B.; McNeil, S. E., Preclinical studies to understand nanoparticle interaction with the immune system and its potential effects on nanoparticle biodistribution. *Mol Pharm* **2008**, *5* (4), 487-95.

Chapter 5 - Next Generation Nanoparticles: Synthesis of Nanoparticles Encapsulating Multiple Drugs.

5.1. Introduction

Combination chemotherapy has become a cornerstone in treating diverse types of cancer, having proved to be more effective than single agents against both metastatic cancer and in patients at high risk of relapse after primary surgical treatment ¹. Several combination regimens have been approved and adopted in the clinic with the aim of enhancing therapeutic efficacy, decreasing dosage at equal or increased levels of efficacy, and reducing drug resistance ². The use of multiple drugs with different molecular targets can raise the molecular barriers that need to be overcome for cancer cell resistance, thereby more effectively mitigating the cancer cell survival. This line of reasoning has led to the development of curative combination chemotherapy regimens (whereas single agent therapy was not) for germ cell tumors, lymphomas and leukemias. In addition, the application of multiple drugs targeting the same cellular pathways can function synergistically for higher therapeutic efficacy and target selectivity ³.

Although the benefits of combination chemotherapy are very attractive, the reality is that for the vast majority of drug combinations still suffer from several disadvantages, including (1) dissimilar pharmacokinetics and tissue distribution of each drug arising from differences in their disparate physicochemical properties, and (2) more serious side effects because each drug is likely to have a different toxicity profile. These disadvantages make dosing and scheduling of each component of the combination a challenging task. As a consequence, special efforts from the scientific and medical communities have been focused on developing strategies to overcome the disadvantages of combination chemotherapy while retaining the benefits to realize its full potential— an example being the introduction into the clinic of the first liposomal formulations containing combinations of different chemotherapeutic agents by Celator Pharmaceuticals ⁴.

Cisplatin and irinotecan are two established drugs routinely used for treating various types of cancer. Cisplatin is a platinum-based drug that binds to and forms adducts with DNA, ultimately triggering apoptosis ⁵⁻⁷. Irinotecan is semisynthetic drug of camptothecin that inhibits topoisomerase I, ultimately blocking both DNA replication and transcription ⁸. The combination of irinotecan and cisplatin (I&C) displays synergy or supra-additive effects when exposed to cultured human tumor cells, human xenograft tumor models and cancer cells freshly isolated from colorectal patients ⁹. In addition, an I&C combination in a Japanese based randomized phase III trial in 2002 showed the regimen resulted in increased overall survival in small cell lung cancer (SCLC) patients when compared to historical controls treated with the conventional regimen of etoposide and cisplatin (E&P) ¹⁰. This study was stopped early due to the positive results after an interim analysis of only 154 patients. In 2006, a phase III trial showed that I&C combination (given in a slightly modified schedule with attenuated cisplatin doses to mitigate toxicities) showed this regimen was as effective as E&P in SCLC ¹¹ and was associated with less

hematological toxicities but more diarrhea. As such a formulation which can provide the same dose intensity as the Japanese study with less toxicity has great potential to show improved efficacy compared with standard dose E&P. Recently, a preclinical study showed that not only was the combination of irinotecan and cisplatin important for achieving enhanced cytotoxicity, but the ratio in which they were administered also played a key role in determining therapeutic efficacy⁹. An optimal ratio of drugs resulted in greater synergy and that ratio varied depending on cell type⁹. Currently, two important aspects that need to be investigated for I&C combination are (i) actively targeting the drug combination to a specific diseased cell type and (ii) delivering both drugs on the same delivery vehicle to create an over-lapping pharmacological profile mediated by the controlled release properties of the vehicle, while ensuring their entry into the cell at a well-defined ratio. Because targeting combined with synchronized and sustained delivery may potentiate the synergistic toxicity of I&C, an enabling technology is needed to test this hypothesis.

Targeted polymeric nanoparticles (NPs) can encapsulate, traffic, and deliver chemotherapeutic agents in a controlled fashion to specific diseased tissues, thereby providing a tremendous potential in the fight against cancer¹². In different animal models and in humans, such NPs have demonstrated improved drug pharmacokinetics, biodistribution, cell- or tissue-specific targeting, and tolerability, resulting in an increase of the therapeutic index of several drugs known to have limited efficacy and/or high toxicity¹³⁻¹⁵. These advantages have driven researchers to implement targeted NPs for the co-encapsulation and co-delivery of two or more drugs in a single NP in order to match the pharmacokinetics and biodistribution of drugs having different chemical and physical properties¹⁶. Recently, we reported the co-encapsulation of cisplatin and docetaxel, two drugs with quite different chemical properties, in PSMA-targeted

polymeric NPs and demonstrated controlled release of both drugs to PSMA-expressing prostate cancer cells¹⁷. This task was accomplished by conjugating a hydrophilic cisplatin prodrug to the backbone of polylactic acid (PLA) to facilitate its incorporation into the hydrophobic NP core¹⁷. Extension of this technology to the co-encapsulation of cisplatin and irinotecan presents an attractive option for targeting I&C therapy with controlled and synchronized delivery of each drug for improved synergism.

In the present work we report poly(D,L-lactide-co-glycolide)-co-poly(ethylene glycol) (PLGA-PEG)-based targeted NPs with both irinotecan and cisplatin encapsulated in the same targeted NP. Incorporation of cisplatin into the NP core was accomplished by conjugating a cisplatin prodrug to the backbone of PLA (PLA-cisplatin) while irinotecan was encapsulated during the self-assembly process of the NP. These NPs were targeted to prostate cancer cells over-expressing PSMA receptor using the small molecule S,S-2-[3-[5-amino-1-carboxypentyl]-ureido]-pentanedioic acid (PSMA Ligand; LIG), previously reported to bind to PSMA receptors and currently in clinical development as a component of a cancer-imaging agent^{18, 19}. The targeted NPs were prepared in a single step by conjugating LIG to the end of PEG in PLGA-PEG (PLGA-PEG-LIG), then mixing it with unmodified PLGA-PEG, PLA-cisplatin, and free irinotecan followed by self-assembly through the nanoprecipitation method in microfluidic devices^{20, 21}. Targeted NPs were characterized with respect to size and drug encapsulation, and selective uptake by PSMA-expressing cells was evaluated. Synergistic performance of the dual drug targeted NPs in PSMA-expressing LNCaP cells was determined at a fixed drug ratio by comparing the cytotoxicity of dual drug targeted NPs to that of NPs encapsulating the same amount of single drugs. Finally, the combination index (CI) was used to quantify the extent of synergism under such conditions.

5.2. Irinotecan and cisplatin in targeted polymeric nanoparticles

The binding, uptake and synergistic mechanism of cellular cytotoxicity of targeted I&C NPs is schematically presented (Figure 5.1). NPs comprise of a PLGA core in which both drugs are incorporated and a PEG shell modified with LIG molecules that target PSMA. As NPs reach the cell surface, multivalent interactions between LIG and the extracellular domain of over-expressed PSMA receptors result in endocytosis²³. Through competition assays and microscopy, previous studies have shown that endocytosis of LIG-targeted NPs is inhibited in the presence of free LIG and that LIG- (and LIG analogs) targeted NPs localized both in the cytoplasm and cell nucleus after being internalized²³⁻²⁶. Once inside, NPs release both drugs in a controlled and sustained fashion¹⁷. In the nucleus, irinotecan inhibits DNA-topoisomerase I complexes, while cisplatin forms DNA cross-links. The end result of both events is cell cycle arrest, transcription inhibition⁷, and apoptosis²⁷. Several studies have suggested that irinotecan acts synergistically with cisplatin by inducing an increase in the lifetime of Pt-DNA adducts resulting in enhanced cytotoxicity²⁷. However, the exact mechanism has not yet been determined.

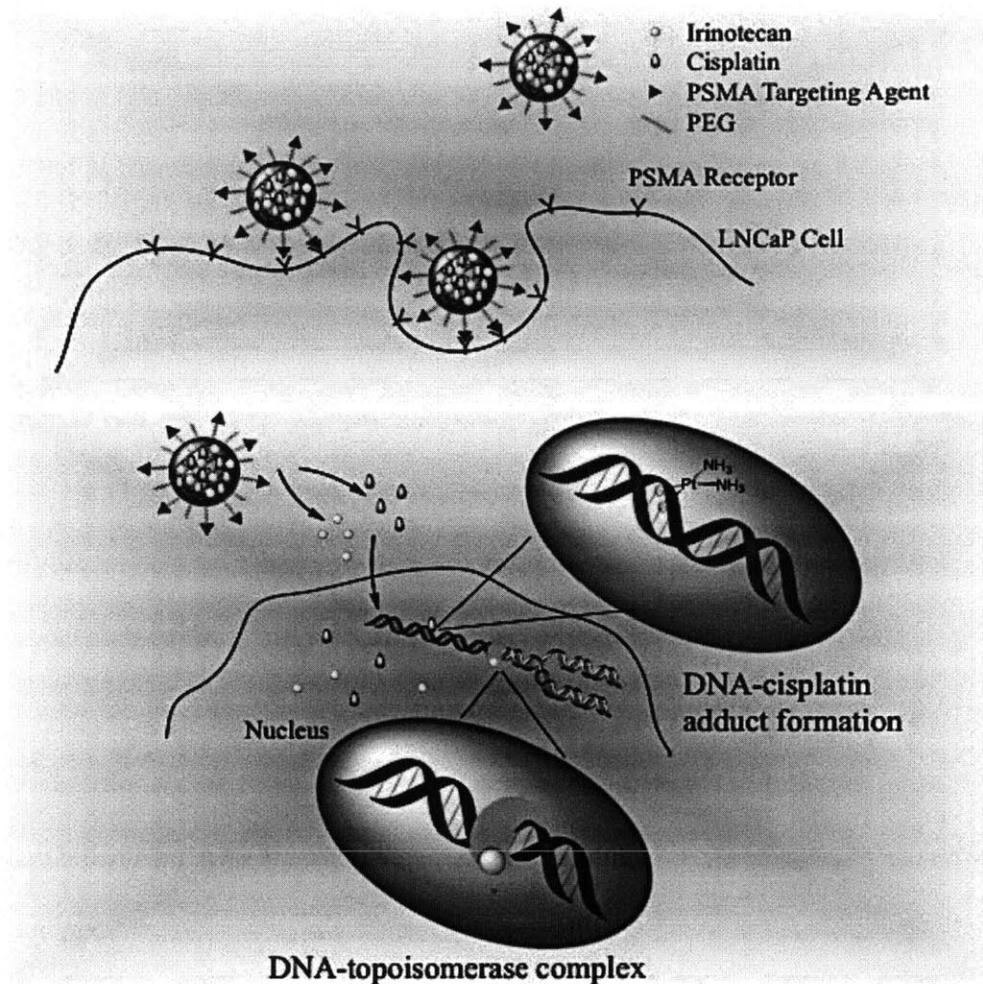
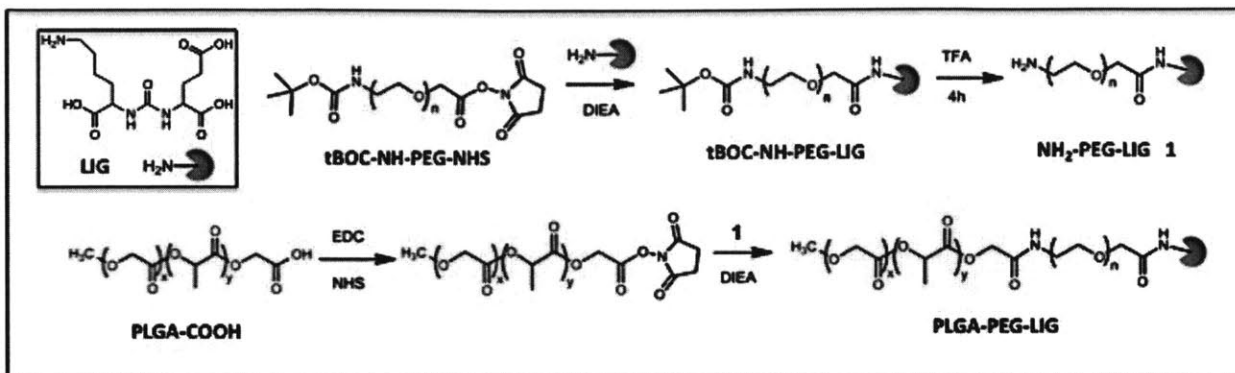
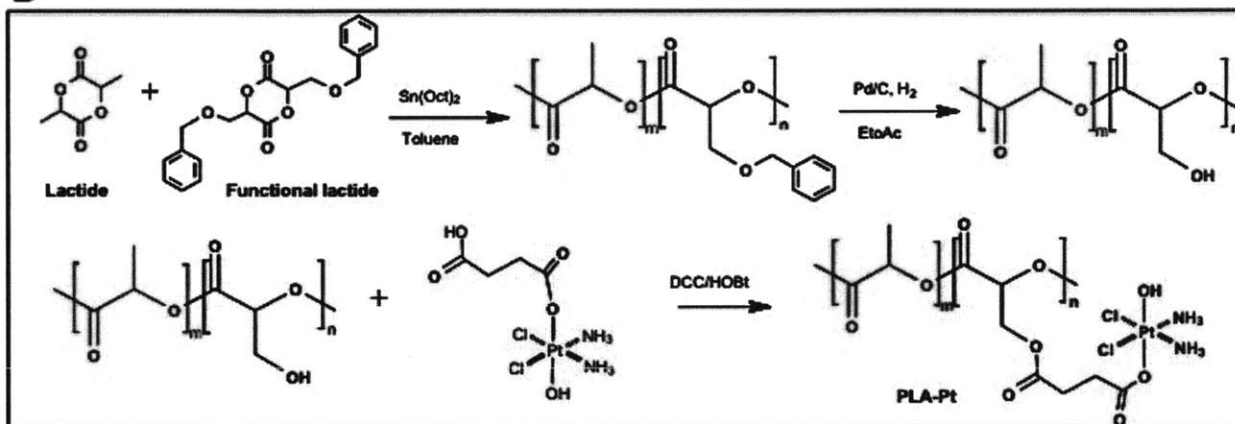


Figure 5.1. Strategy of co-encapsulation of irinotecan and cisplatin in a single nanoparticle targeted to PSMA receptors in prostate cancer cells.
Once internalized, NPs co-deliver irinotecan and cisplatin to enable synergistic toxicity.

5.3 PLGA-PEG-LIG and PLA-Pt polymer synthesis

To minimize the number of steps in the synthesis of targeted NPs, we prepared a ligand-conjugated PLGA-PEG copolymer (Figure 5.2A). LIG is a urea-based small molecule that is not subject to supply, stability and analytical challenges associated with macromolecule-based targeting ligands, such as aptamers or antibodies²⁸. It contains a free primary amine that can be

used to anchor LIG to the NP surface without affecting the targeting capabilities of the molecule. LIG was allowed to react with succinimide-modified tBOC-NH-PEG-NHS, which after deprotection was conjugated to a succinimide-modified PLGA. The functionalized PLGA-PEG-LIG contains necessary components for forming and targeting the NPs, enabling their single step self-assembly and simplifying the optimization and potential scale up²⁹. To co-deliver irinotecan and cisplatin, two therapeutic agents with different chemical properties (hydrophobic and hydrophilic, respectively), we synthesized a modified PLA polymer with reactive hydroxyl functional groups to enable conjugation of a platinum prodrug to the polymer backbone (Figure 5.2B). Previous work demonstrated that this platinum prodrug can be cleaved from the backbone of the polymer and reduced to cisplatin intracellularly, which then forms the *cis*-diammineplatinum(II) 1,2-d(GpG) cross-links on nuclear DNA, the principal adduct made by cisplatin^{17, 30}. AAS of PLA-cisplatin confirmed that ~2.5% by weight of platinum was conjugated to the polymer.

A**B****Figure 5.2. Polymer synthesis.****(A)** Synthesis of PLGA-PEG-LIG. **(B)** Synthesis of PLA-cisplatin

5.4. Microfluidic synthesis of nanoparticles.

The targeted NPs presented here comprise four different components that self-assemble in a single mixing step into a drug-loaded core-shell nanostructure containing targeting moieties on the surface. These components are: (i) PLGA-PEG block copolymer that forms the core-shell structure, (ii) PLGA-PEG-LIG that self-assembles together with PLGA-PEG and orients LIG toward the NP surface, (iii) PLA-cisplatin prodrug that assembles in the hydrophobic NP core by hydrophobic-hydrophobic interactions of PLGA and PLA, (iv) irinotecan, which partitions into the hydrophobic core based on its physicochemical properties. NPs were prepared in

microfluidic channels by a rapid mixing strategy called hydrodynamic flow focusing (HFF)^{21,31} (Figure 5.3A). In this method, polymers and drugs are mixed in acetonitrile and run in a stream that becomes horizontally focused into a very thin stream when it encounters two streams of water running at a flow rate 10 times higher (Figure 5.3B). Upon focusing, nanoprecipitation occurs through mixing of the aqueous and organic streams inducing NP self-assembly. This method ensures controlled precipitation and rapid mixing, which results in reproducible, monodisperse NPs with smaller size and higher drug loading than NPs prepared through conventional bulk methods²¹. Figure 5.3C shows the characterization of the NPs by DLS, resulting in an average size of 55 nm and a polydispersity of 0.04, indicative of relatively monodisperse particles. A TEM image of these NPs reveals an average size of ~55 nm, which matches that obtained from DLS (Figure 5.3D). By assuming both an average NP density of 1.27 g/mL³² and that all PLGA-PEG-LIG self-assembles into a NP with LIG molecules on the NP surface²⁹, we compute that NPs with average diameter of 55 nm and comprising 25% by weight of PLGA-PEG-LIG will have an average of 252 LIG molecules per NP.

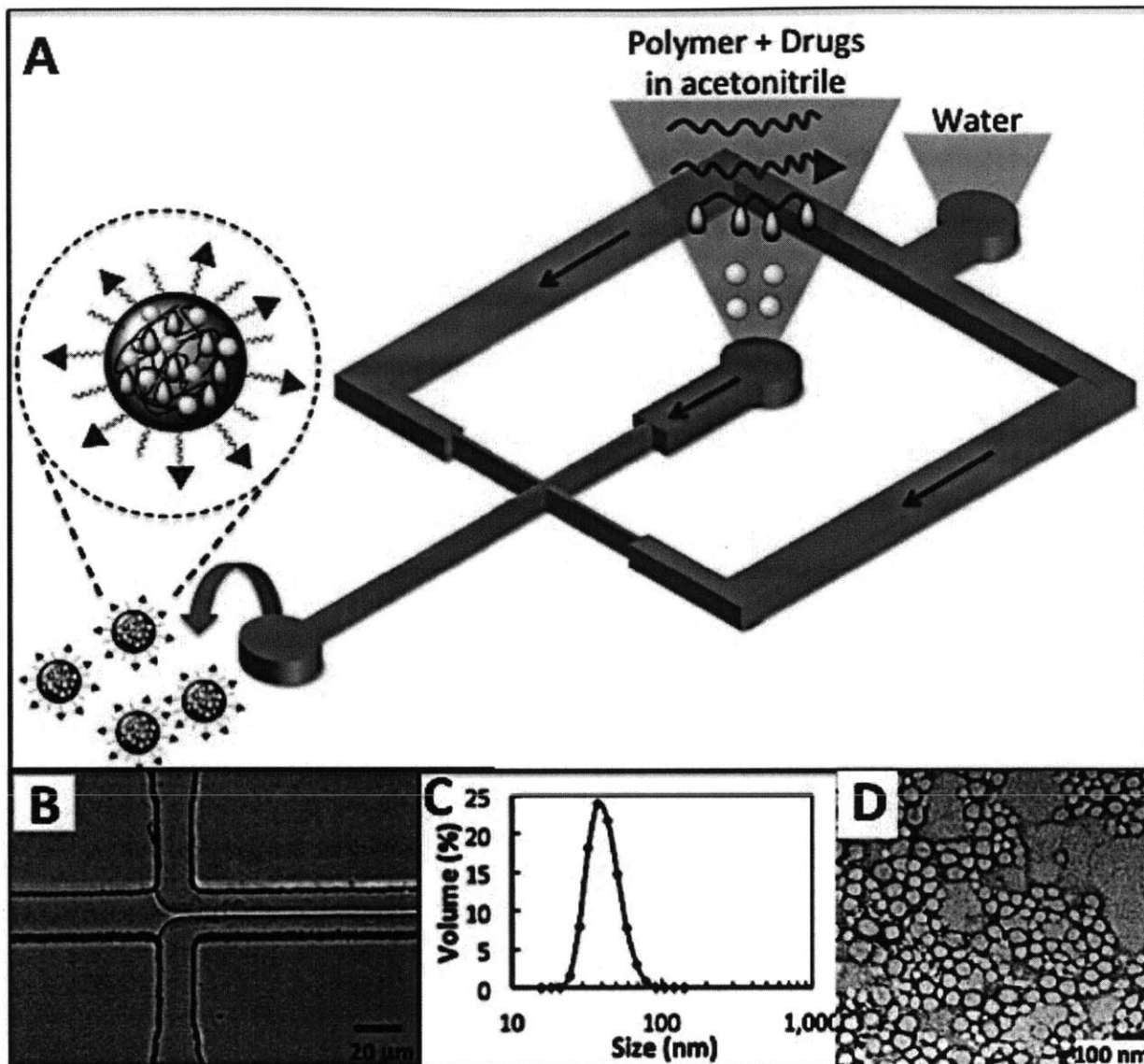


Figure 5.3. Single-step synthesis of targeted nanoparticles in microfluidic devices using hydrodynamic flow focusing.

(A) Schematic of nanoparticles synthesis. (B) Visualization of flow focusing in a microfluidic channel during operation. Acetonitrile flow rate = 5 mL/min and water flow rate = 50 mL/min. (C) Size distribution of targeted nanoparticles by volume. Average size = 55 nm. Polydispersity index = 0.04. (D) TEM image of nanoparticles stained with 1% solution of uranyl acetate. Average size = 55 nm.

5.5. Characterization of nanoparticles encapsulating cisplatin and irinotecan

To evaluate the effect on NP size of incorporating multiple drugs, we measured the size and stability of NPs encapsulating only irinotecan (NP_I), only cisplatin (NP_C), and both irinotecan and cisplatin (NP_{I&C}) (Figure 5.4A and 5.4B). In addition, we determined the drug loading, encapsulation efficiency (EE), and release kinetics of each drug in the NPs (Figure 5.4C and 5.4D). Interestingly, the size of all three NPs was similar with average diameter of approximately 55 ± 4 nm, which remained stable for a period of 24 h. This consistency in NP size is presumably a consequence of the rapid mixing environment enabled by the microfluidic devices, which ensures complete mixing of precursors in water at a time scale smaller than the NP self-assembly and results in the formation of a relatively uniform population of NPs³³. Cisplatin was encapsulated with very high efficiency (>80%) owing to the hydrophobic-hydrophobic interaction between PLGA and the PLA backbone. Irinotecan exhibited EE and drug loading values of 10% and 0.5%, respectively, after self-assembly with PLGA-PEG. However, when irinotecan was mixed with both PLGA-PEG and PLA-cisplatin, its EE and drug loading increased to 44% and 2.2%, respectively (Figure 5.4C). This increase may be a consequence of the increased hydrophobicity of the NP core due to the hydrophobic PLA polymer that favors encapsulation of the hydrophobic irinotecan (as shown previously for a similar system of free PLGA and docetaxel²¹). This formulation resulted in an irinotecan to cisplatin mol ratio of 1.5:1 and was used for the all experiments in this study. From the kinetics it was found that encapsulated irinotecan was released at a faster rate than covalently conjugated cisplatin prodrug, which is expected and agrees well with a previous report on a similar system¹⁷. Through this NP platform the encapsulation and release rate of irinotecan or other

encapsulated drugs can be modulated by varying the molecular weight of the PLGA in PLGA-PEG, the concentration of PLGA-PEG in the organic solution and the initial loading wt.% of irinotecan^{20, 34}, while for cisplatin variation of the MW of PLA in PLA-cisplatin, and the number of cisplatin molecules in PLA-cisplatin allow for controlling its encapsulation and release. Considering different types of cancer may benefit from different drug ratios and release rates⁹, the ability to control the encapsulation and release rate is an advantage that would potentially allow for tuning the payload according to the therapeutic need of each type of cancer.

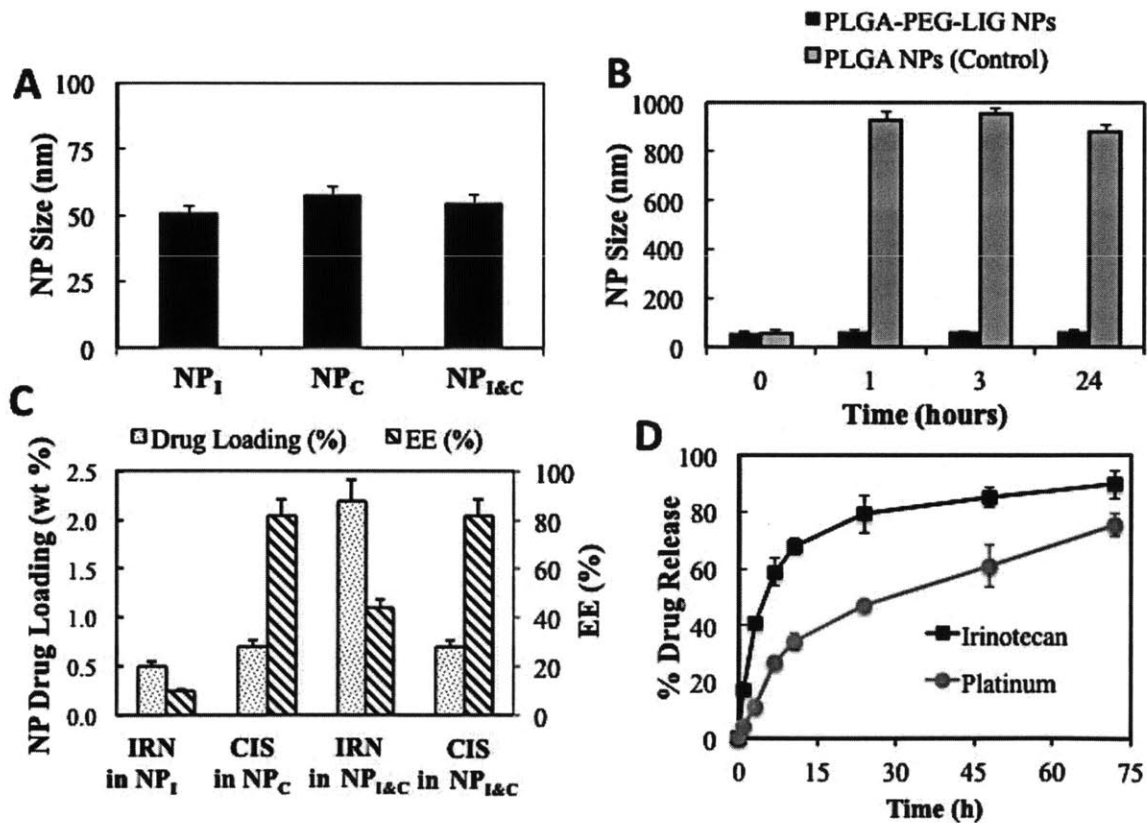


Figure 5.4. Characterization of nanoparticles containing either irinotecan (NP_I) or cisplatin (NP_C) prodrug or both (NP_{I&C}). (A) Size (B) Size stability over time in 10% serum (PLGA NPs were used as a positive control), (C) Drug loading and encapsulation efficiency, and (D) drug release kinetics in PBS at 37°C.

5.6. Cell targeting of nanoparticles decorated with LIG

Next we tested the targeting capabilities of the PSMA-targeted NPs *in vitro*. To enable analysis of NP uptake by flow cytometry, 2.5% by weight of the fluorescent probe PLGA-Alexa 488 was added to the organic stream containing both drugs and polymers. In a previous work we showed that this amount was low enough so as not to affect the NP physicochemical properties but high enough to be detected readily by FACS at very low NP concentrations²⁹. To test the targeting capabilities of our NPs, we incubated them with PSMA-overexpressing LNCaP cells for 4 h, trypsinized them to remove any bound NPs on the cell surface, and measured the fluorescence intensity of 10,000 cells (Figure 5.5A). Cells treated with PSMA-targeted NPs exhibited 8-fold more fluorescence compared to those treated with non-targeted NPs. FACS fluorescence histograms show that NP uptake by cells occurred uniformly across all the cells rather than by a few cells engulfing most of NPs (Figure 5.5B). Previous studies have demonstrated that LIG- (and LIG analogs) targeted nanoparticles enter the cell through endocytosis and localize both in the cytoplasm and cell nucleus²³⁻²⁵. It is therefore likely that these NPs are escaping the endosome and reaching other cell compartments, including nucleus. The exact mechanism will be explored in future studies. These results indicate that our dual-drug targeted NPs can selectively target cells over-expressing PSMA receptors and that they can enter the cells more readily than non-targeted NPs.

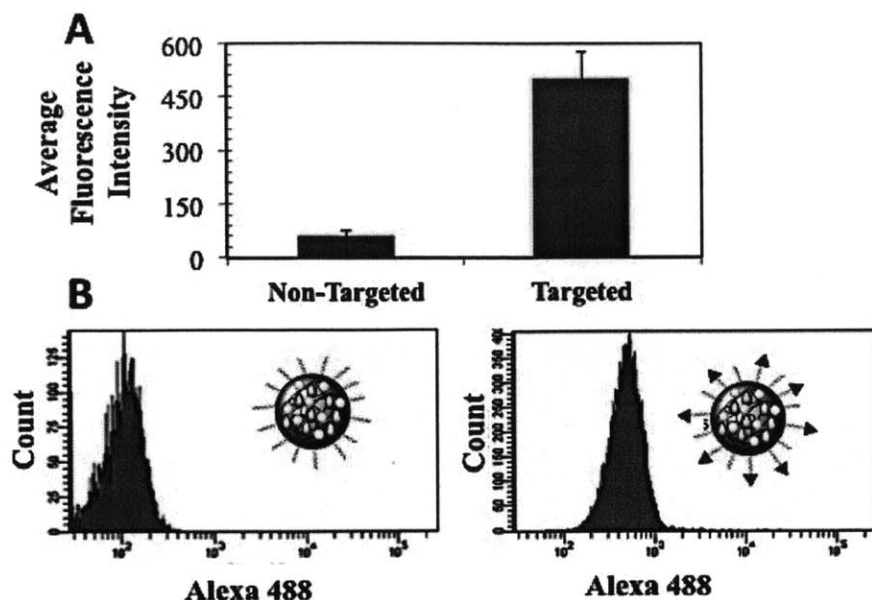


Figure 5.5. Uptake of PSMA-targeted NPs in LNCaP cells overexpressing PSMA receptors compared to non-targeted NPs.

The NPs contain the fluorescent reporter Alexa 488 conjugated to PLGA (PLGA-Alexa 488). (A) Average fluorescence of 10,000 cells obtained by FACS. (B) FACS histograms of fluorescence intensity.

5.7. Synergistic cytotoxicity of irinotecan-cisplatin nanoparticles

Finally, we carried out cytotoxicity studies *in vitro* to assess the synergy of cisplatin and irinotecan in LNCaP cells. Targeted NP_I, NP_C, and NP_{I&C} were exposed to LNCaP cells at different concentrations while keeping the same incubation volumes. The cytotoxicities were evaluated using 3-(4,5-dimethylthiazol-2-yl)-2,5-diphenyltetrazolium bromide (MTT) assay. Based on the concentration of drugs in each NP we created dose-response curves and determined the IC₅₀ values for each NP formulation (Figure 5.6A). NP_{I&C} was 3.6 times and 10.6 more toxic than NP_C, and NP_I, respectively, after 12 h of exposure to LNCaP cells. Whereas these results suggest that NP_{I&C} is more cytotoxic than the single-drug NPs, it does not assess whether this effect is synergistic or simply additive. To determine synergism of the dual-drug NPs, we used

the Talay and Chou method³⁵ and calculated a combination index (CI) at ED₈₀, as previously reported by others for a similar system⁹. In this method a CI ~1 indicates additivity, CI >1 indicates an antagonism and CI <1 indicates synergism. Remarkably, NP_{I&C} had a CI of 0.20, which falls in the range of strong synergism³⁵. These results demonstrate that PSMA-targeted NP_{I&C} exhibit synergistic cytotoxicity against prostate cancer cells under the investigated experimental conditions. All previous work on cisplatin/irinotecan combinations was carried out with either free drugs or each drug encapsulated in a separate liposome, the present investigation being the first for this combination that has been evaluated (1) by encapsulating both agents in the same vehicle and (2) with a nanoparticle targeted to a specific cell type. Finally, although the initial drug ratio of irinotecan/cisplatin in the targeted NP was fixed at 1.5, differences in release kinetics of each drug may alter the actual ratio that reaches the cell nucleus. In fact, investigating the performance of targeted NPs containing different initial drug ratios and/or varying drug release kinetics could potentially result in finding formulations with even greater synergism.

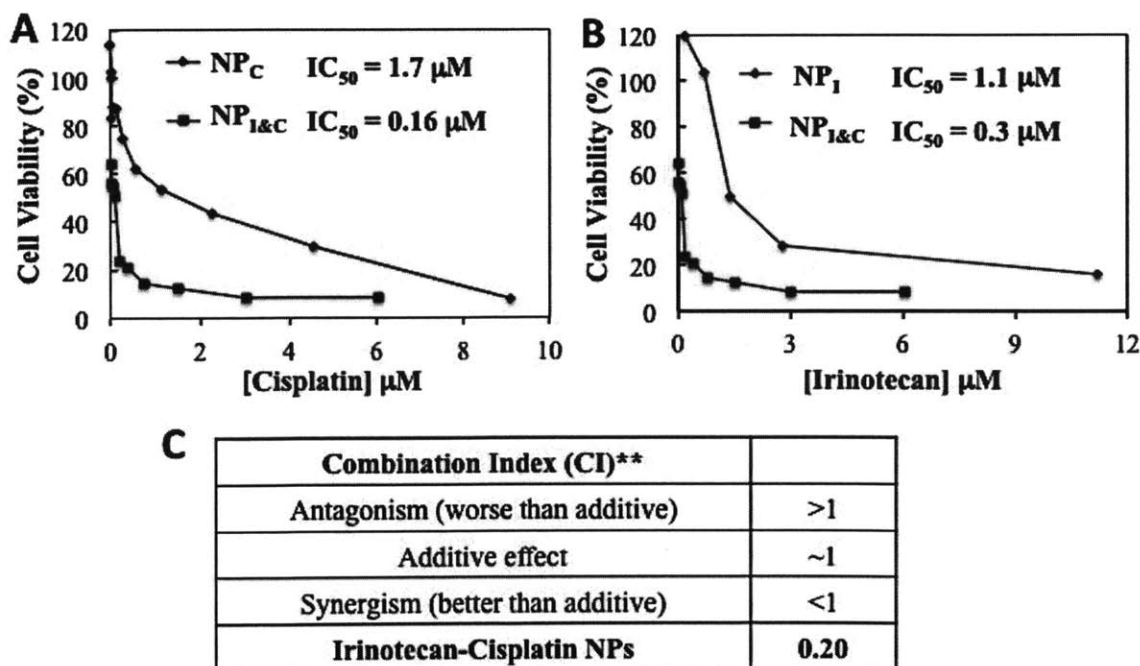


Figure 5.6. Cytotoxicity of nanoparticles with irinotecan and cisplatin.

Cytotoxicity of I&C targeted NPs ($NP_{I\&C}$) in LNCaP cells compared irinotecan targeted NPs (NP_I) (A) and cisplatin targeted NPs (NP_C) (B). Dual-drug NPs had an IC_{50} 10.6 times and 3.6 times lower than cisplatin and irinotecan NPs, respectively. (C) Combination index determined by Talay and Chou method at ED_{80} . According to the metric 0.20 corresponds to strong synergism. The NPs used had a final irinotecan to cisplatin ratio of 1.5:1 by mole.

5.8. Conclusion

In summary, we have devised a novel strategy for trafficking and delivering irinotecan and cisplatin to a specific cell population by encapsulating both drugs in one NP and targeting the NPs to specific cells with a small molecule targeting agent. Although the two drugs have different chemical and physical properties, they were successfully incorporated into the same NP by conjugating the more hydrophilic drug, cisplatin, to the backbone of a PLA-based polymer and encapsulating the more hydrophobic irinotecan in a conventional fashion through nanoprecipitation. NPs prepared with the use of a single-step in microfluidic device exhibited an average size of 55 ± 4 nm that remained essentially unchanged before and after the addition of both drugs. The low polydispersity index of ~ 0.04 is indicative of a relatively monodisperse population, presumably arising from the rapid mixing environment offered by the microfluidic devices. Specific uptake of targeted NPs by LNCaP cells overexpressing the PSMA receptor was demonstrated by the 8-fold increase in fluorescence associated with targeted NPs compared to non-targeted NPs. Finally synergistic cytotoxicity of irinotecan-cisplatin targeted NPs in LNCaP cells was assessed by a CI of 0.20, which is characteristic of strong synergism. From these results we anticipate that by implementing a two-drugs-in-one-NP strategy together with active targeting to specific cell receptors, combination chemotherapy with irinotecan and cisplatin could potentially be implemented, even in cancers that have traditionally exhibited poor

therapy response, such as prostate cancer³⁶. In addition, a single-step synthesis of NPs composed of approved drugs and clinically validated biomaterials may accelerate translation of such novel therapeutics to the clinic.

5.9. Materials and methods

Materials. Poly(D,L-lactide-co-glycolide)-co-Poly(ethylene glycol) was purchased from Boehringer Ingelheim (Ingelheim am Rhein, Germany). Poly(D,L-lactide-co-glycolide) (50/50) with terminal carboxylate groups (PLGA, inherent viscosity 0.67 dL/g, MW ~ 45 kDa) was purchased from Lactel (Pelham, AL, USA) and tBOC-NH-PEG-NH₂ (MW 5000) and tBOC-NH-PEG-NHS, (MW 5000) were purchased from Laysan Bio, Inc (Arab, AL, USA). MTT reagent was procured from Sigma-Aldrich (St. Louis, MO, USA). LNCaP cell line was obtained from American Type Culture Collection (Manassas, VA, USA).

Synthesis of PLGA-PEG-LIG. The synthesis of PLGA-PEG-LIG (PLGA MW 45K and PEG MW 5K) was achieved by first conjugating LIG to PEG followed by conjugation of the resultant LIG-PEG to PLGA. LIG (3.9 mg, 8.9 μmol) was dissolved in 400 μL of dimethylformamide (DMF) and allowed to react with tBOC-NH-PEG-NHS (22 mg, 4.5 μmol) in the presence of *N,N*-diisopropylethylamine (DIEA, 10 μL) for 12 h. The reaction product was dialyzed for 24 h in water to remove unreacted LIG, then lyophilized, and finally resuspended in 400 μL of trifluoroacetic acid (TFA) to remove tBOC. After 4 h, PEG-LIG was dried and dissolved in 200 μL of DMSO. In parallel, PLGA-COOH (100 mg, 2.2 μmol) was allowed to react with *N*-hydroxysuccinimide (NHS) in the presence of 1-ethyl-3-[3-dimethylaminopropyl] carbodiimide (EDC) in dichloromethane (DCM) for 2 h. The resulting PLGA-NHS was dried and dissolved in 300 μL of DMSO. Finally, PEG-LIG and PLGA-NHS in DMSO were mixed with DIEA,

allowed to react for 24 h, precipitated in cold methanol, and dried under vacuum. PLGA-PEG-LIG was characterized by gel permeation chromatography (GPC) to confirm the synthesis of PLGA-PEG-LIG.

Synthesis of PLA-Cisplatin. First, PLA-OBn was synthesized via ring opening polymerization reaction by dissolving a toluene-functionalized cyclic lactide monomer and simple lactide monomer in a toluene solution containing benzyl alcohol (initiator) and Tin catalyst. The solution was refluxed at 120 °C for 10 h. Then, the hydroxyl functionalized biodegradable polylactide polymer (PLA-OH) was obtained by benzyl deprotection using a Pd/C catalyst at 50 psi pressure for 8 h. Finally, succinic acid-derivative platinum (IV) (cisplatin prodrug) was dissolved in anhydrous DMF and added with excess equivalents of N-hydroxybenzotriazole (HOBT), N,N'-dicyclohexylcarbodiimide (DCC) and stirred at room temperature for 30 min. To this reaction mixture a solution of PLA-OH polymer in dichloromethane was added and stirred at room temperature for 12 hours, followed by precipitation in diethyl ether.

Synthesis and Characterization of NPs. NP synthesis was carried out in microfluidic devices made of PDMS. The device had one inlet each for water and precursors streams, and one outlet. The water stream was split into two in order to achieve two water streams at the flow focusing junction. The mixing channel was 20 mm wide, 60 mm high and 1 cm long and formed nanoparticles by focusing in two dimensions. The 2.5 mL and 0.5 mL gastight syringes used for aqueous and organic streams, respectively, were mounted on syringe pumps to control flow through the device. NPs were prepared by nanoprecipitation. Briefly, 250 mL of PLGA-PEG at 10 mg/mL in acetonitrile was mixed with 250 mL of PLGA-PEG-LIG and 500 mL of PLA-cisplatin both at 10 mg/mL in acetonitrile. Irinotecan was mixed with the polymers to reach an initial drug loading of 5%, corresponding to a concentration of 0.5 mg/mL. The organic stream

(polymers and drugs) was run at 5 mL/min while maintaining a total aqueous flow rate of 50 mL/min. NPs were collected at the outlet stream and washed three times with water using Amicon centrifugation filtration membrane to remove excess drugs and organic solvents. Dynamic light scattering (DLS) was used to determine particle size and size distribution, using a Zetasizer Nano ZS instrument (Malvern Instruments Ltd., U.K.). Particle visualization was carried out through TEM (JEOL 2011 instrument at an acceleration voltage of 200 kV.) The sample was prepared by depositing 10 μ L of the NP solution onto a 300-mesh carbon-coated copper grid. After 30 min incubation samples were blotted away and grids were negatively stained for 20 min with 1% (w/v) uranyl acetate aqueous solution. The stability of NPs was evaluated by suspending freshly made NPs in a PBS solution containing 10% serum and measuring the size of the particles at different time points over a period of 24 h. PLGA NPs were used as a control since they are known to aggregate over time²⁰. Drug loading and encapsulation efficiency (EE) were determined by quantifying the amount of drug in NP. To evaluate drug loading, NPs were dissolved in a 50/50 acetonitrile/water solution immediately after synthesis and vortexed for several hours to induce NP dissociation. The amount of platinum inside the NPs was quantitated by flameless atomic absorption spectroscopy (AAS), from which the load of cisplatin was computed. Irinotecan was detected using spectrophotometry on a TECAN 1000 plate reader at a wavelength of 385 nm. A calibration curve with known concentrations of irinotecan was prepared, and the amount of irinotecan encapsulated in the NPs was calculated accordingly. In vitro release kinetics of irinotecan and cisplatin were determined by dialyzing 100 mL aliquots of NPs in mini dialysis cassettes with a MW cutoff of 10 kDa against a 4-liter bath of PBS at 37°C. Three aliquots were removed at different time points over a period of 72

hours and the amount of irinotecan and cisplatin remaining inside the NPs were measured as described above.

NP Uptake by LNCaP cells. LNCaP cells were cultured in RPMI 1640 medium with 10% fetal bovine serum, 50 units/mL of penicillin, and 50 mg/mL of streptomycin. Cells were seeded at a density of 50,000 cells per well on a 24-well plate for 24 h. Subsequently, the cell medium was replaced with NPs dissolved in the same medium at a concentration of 1 mg/mL and incubated for 4 h followed by three washes with 1% BSA solution in PBS to remove excess NPs. LNCaP cells were treated with trypsin, removed from the plate, centrifuged, and were reconstituted in 250 mL of PBS. Immediately after cells were analyzed through flow cytometry analysis on a BD Biosciences LSR II with high-throughput sampler (HTS) option in a 96-well plate, with 10,000 cells collected for each measurement (n = 4 per formulation).

In vitro NP Cytotoxicity (MTT Assay). The cytotoxicity of NPs was investigated through the MTT assay. First, cells were seeded on a 96-well plate in 100 μ L of cell medium and incubated for 24 h. Then, the medium was replaced with NP suspension at varying concentrations and incubated for 12 h at 37 °C. The medium was changed after 12 h, and the cells were incubated for 48 h. Subsequently, 20 μ L of MTT (5 mg/mL in PBS) were added to the cells and allowed for incubation for 5 h. After removing the medium the cells were lysed by adding 100 μ L of DMSO, and the absorbance of the purple formazan was recorded at 550 nm using plate reader.

5.10. References

1. Chabner, B. A.; Roberts, T. G., Jr., Timeline: Chemotherapy and the war on cancer. *Nat Rev Cancer* **2005**, *5* (1), 65-72.
2. Jia, J.; Zhu, F.; Ma, X.; Cao, Z.; Li, Y.; Chen, Y. Z., Mechanisms of drug combinations: interaction and network perspectives. *Nat Rev Drug Discov* **2009**, *8* (2), 111-28.

3. Lehar, J.; Krueger, A. S.; Avery, W.; Heilbut, A. M.; Johansen, L. M.; Price, E. R.; Rickles, R. J.; Short, G. F., 3rd; Staunton, J. E.; Jin, X.; Lee, M. S.; Zimmermann, G. R.; Borisy, A. A., Synergistic drug combinations tend to improve therapeutically relevant selectivity. *Nat Biotechnol* **2009**, *27* (7), 659-66.
4. Mayer, L. D.; Harasym, T. O.; Tardi, P. G.; Harasym, N. L.; Shew, C. R.; Johnstone, S. A.; Ramsay, E. C.; Bally, M. B.; Janoff, A. S., Ratiometric dosing of anticancer drug combinations: controlling drug ratios after systemic administration regulates therapeutic activity in tumor-bearing mice. *Mol Cancer Ther* **2006**, *5* (7), 1854-63.
5. Kelland, L., The resurgence of platinum-based cancer chemotherapy. *Nat Rev Cancer* **2007**, *7* (8), 573-84.
6. Wang, D.; Lippard, S. J., Cellular processing of platinum anticancer drugs. *Nat Rev Drug Discov* **2005**, *4* (4), 307-20.
7. Jung, Y.; Lippard, S. J., Direct cellular responses to platinum-induced DNA damage. *Chem Rev* **2007**, *107* (5), 1387-407.
8. Garcia-Carbonero, R.; Supko, J. G., Current perspectives on the clinical experience, pharmacology, and continued development of the camptothecins. *Clin Cancer Res* **2002**, *8* (3), 641-61.
9. Tardi, P. G.; Dos Santos, N.; Harasym, T. O.; Johnstone, S. A.; Zisman, N.; Tsang, A. W.; Bermudes, D. G.; Mayer, L. D., Drug ratio-dependent antitumor activity of irinotecan and cisplatin combinations in vitro and in vivo. *Mol Cancer Ther* **2009**, *8* (8), 2266-75.
10. Noda, K.; Nishiwaki, Y.; Kawahara, M.; Negoro, S.; Sugiura, T.; Yokoyama, A.; Fukuoka, M.; Mori, K.; Watanabe, K.; Tamura, T.; Yamamoto, S.; Saijo, N.; Japan Clinical Oncology, G., Irinotecan plus cisplatin compared with etoposide plus cisplatin for extensive small-cell lung cancer. *N Engl J Med* **2002**, *346* (2), 85-91.
11. Hanna, N.; Bunn, P. A., Jr.; Langer, C.; Einhorn, L.; Guthrie, T., Jr.; Beck, T.; Ansari, R.; Ellis, P.; Byrne, M.; Morrison, M.; Hariharan, S.; Wang, B.; Sandler, A., Randomized phase III trial comparing irinotecan/cisplatin with etoposide/cisplatin in patients with previously untreated extensive-stage disease small-cell lung cancer. *J Clin Oncol* **2006**, *24* (13), 2038-43.
12. Peer, D.; Karp, J. M.; Hong, S.; Farokhzad, O. C.; Margalit, R.; Langer, R., Nanocarriers as an emerging platform for cancer therapy. *Nat Nanotechnol* **2007**, *2* (12), 751-60.
13. Shi, J.; Xiao, Z.; Kamaly, N.; Farokhzad, O. C., Self-Assembled Targeted Nanoparticles: Evolution of Technologies and Bench to Bedside Translation. *Acc Chem Res* **2011**.
14. Hrkach, J.; Von Hoff, D.; Ali, M.; Andrianova, E.; Auer, J.; Campbell, T.; de Witt, D.; Figa, M.; Figueiredo, M.; Horhota, A.; Low, S.; McDonnell, K.; Peeke, E.; Retnarajan, B.; Sabnis, A.; Schnipper, E.; Song, J.; Song, Y. H.; Summa, J.; Tompsett, D.; Troiano, G.; van Geen, T.; Wright, J.; LoRusso, P.; Kantoff, P. W.; Bander, N. H.; Sweeney, C. J.; Farokhzad, O. C.; Langer, R.; Zale, S., Preclinical Development and Clinical Translation of a PSMA-Targeted Docetaxel Nanoparticle with a Differentiated Pharmacological Profile. *Sci Transl Med* **2012**, *4*.
15. Kamaly, N.; Xiao, Z.; Valencia, P. M.; Radovic-Moreno, A. F.; Farokhzad, O. C., Targeted polymeric therapeutic nanoparticles: design, development and clinical translation. *Chem Soc Rev* **2012**, *41* (7), 2971-3010.
16. Hu, C.; Aryal, S.; Zhang, L., Nanoparticle-assisted combination therapies for effective cancer treatment. *Therapeutic Delivery* **2010**, *1* (2), 323-334.
17. Kolishetti, N.; Dhar, S.; Valencia, P. M.; Lin, L. Q.; Karnik, R.; Lippard, S. J.; Langer, R.; Farokhzad, O. C., Engineering of self-assembled nanoparticle platform for precisely controlled combination drug therapy. *Proc Natl Acad Sci U S A* **2010**, *107* (42), 17939-44.

18. Maresca, K. P.; Hillier, S. M.; Femia, F. J.; Keith, D.; Barone, C.; Joyal, J. L.; Zimmerman, C. N.; Kozikowski, A. P.; Barrett, J. A.; Eckelman, W. C.; Babich, J. W., A series of halogenated heterodimeric inhibitors of prostate specific membrane antigen (PSMA) as radiolabeled probes for targeting prostate cancer. *J Med Chem* **2009**, *52* (2), 347-57.
19. Hillier, S. M.; Maresca, K. P.; Femia, F. J.; Marquis, J. C.; Foss, C. A.; Nguyen, N.; Zimmerman, C. N.; Barrett, J. A.; Eckelman, W. C.; Pomper, M. G.; Joyal, J. L.; Babich, J. W., Preclinical evaluation of novel glutamate-urea-lysine analogues that target prostate-specific membrane antigen as molecular imaging pharmaceuticals for prostate cancer. *Cancer Res* **2009**, *69* (17), 6932-40.
20. Cheng, J.; Teply, B. A.; Sherifi, I.; Sung, J.; Luther, G.; Gu, F. X.; Levy-Nissenbaum, E.; Radovic-Moreno, A. F.; Langer, R.; Farokhzad, O. C., Formulation of functionalized PLGA-PEG nanoparticles for in vivo targeted drug delivery. *Biomaterials* **2007**, *28* (5), 869-76.
21. Karnik, R.; Gu, F.; Basto, P.; Cannizzaro, C.; Dean, L.; Kyei-Manu, W.; Langer, R.; Farokhzad, O. C., Microfluidic platform for controlled synthesis of polymeric nanoparticles. *Nano Lett* **2008**, *8* (9), 2906-12.
22. Valencia, P. M.; Basto, P. A.; Zhang, L.; Rhee, M.; Langer, R.; Farokhzad, O. C.; Karnik, R., Single-step assembly of homogenous lipid-polymeric and lipid-quantum dot nanoparticles enabled by microfluidic rapid mixing. *ACS Nano* **2010**, *4* (3), 1671-9.
23. Chandran, S. S.; Banerjee, S. R.; Mease, R. C.; Pomper, M. G.; Denmeade, S. R., Characterization of a targeted nanoparticle functionalized with a urea-based inhibitor of prostate-specific membrane antigen (PSMA). *Cancer Biol Ther* **2008**, *7* (6), 974-82.
24. Thomas, M.; Kularatne, S. A.; Qi, L.; Kleindl, P.; Leamon, C. P.; Hansen, M. J.; Low, P. S., Ligand-targeted delivery of small interfering RNAs to malignant cells and tissues. *Ann N Y Acad Sci* **2009**, *1175*, 32-9.
25. Kularatne, S. A.; Wang, K.; Santhapuram, H. K.; Low, P. S., Prostate-specific membrane antigen targeted imaging and therapy of prostate cancer using a PSMA inhibitor as a homing ligand. *Mol Pharm* **2009**, *6* (3), 780-9.
26. Hrkach, J.; Von Hoff, D.; Ali, M. M.; Andrianova, E.; Auer, J.; Campbell, T.; De Witt, D.; Figa, M.; Figueiredo, M.; Horhota, A.; Low, S.; McDonnell, K.; Peeke, E.; Retnarajan, B.; Sabnis, A.; Schnipper, E.; Song, J. J.; Song, Y. H.; Summa, J.; Tompsett, D.; Troiano, G.; Van Geen Hoven, T.; Wright, J.; Lorusso, P.; Kantoff, P. W.; Bander, N. H.; Sweeney, C.; Farokhzad, O. C.; Langer, R.; Zale, S., Preclinical Development and Clinical Translation of a PSMA-Targeted Docetaxel Nanoparticle with a Differentiated Pharmacological Profile. *Sci Transl Med* **2012**, *4* (128), 128ra39.
27. Zastre, J.; Anantha, M.; Ramsay, E.; Bally, M., Irinotecan-cisplatin interactions assessed in cell-based screening assays: cytotoxicity, drug accumulation and DNA adduct formation in an NSCLC cell line. *Cancer Chemother Pharmacol* **2007**, *60* (1), 91-102.
28. Gu, F. X.; Karnik, R.; Wang, A. Z.; Alexis, F.; Levy-Nissenbaum, E.; Hong, S.; Langer, R. S.; Farokhzad, O. C., Targeted nanoparticles for cancer therapy. *Nano Today* **2007**, *2* (3), 14-21.
29. Valencia, P. M.; Hanewich-Hollatz, M. H.; Gao, W.; Karim, F.; Langer, R.; Karnik, R.; Farokhzad, O. C., Effects of Ligands with Different Water Solubilities on Self-Assembly and Properties of Targeted Nanoparticles. *Biomaterials* **2011**, (*in press*).
30. Dhar, S.; Gu, F. X.; Langer, R.; Farokhzad, O. C.; Lippard, S. J., Targeted delivery of cisplatin to prostate cancer cells by aptamer functionalized Pt(IV) prodrug-PLGA-PEG nanoparticles. *Proc Natl Acad Sci U S A* **2008**, *105* (45), 17356-61.

31. Rhee, M.; Valencia, P. M.; Rodriguez, M. I.; Langer, R.; Farokhzad, O. C.; Karnik, R., Synthesis of size-tunable polymeric nanoparticles enabled by 3D hydrodynamic flow focusing in single-layer microchannels. *Adv Mater* **2011**, *23* (12), H79-83.
32. Vauthier, C.; Schmidt, C.; Couvreur, P., Measurement of the density of polymeric nanoparticulate drug carriers by isopycnic centrifugation. *J Nanoparticle Res* **1999**, *1*, 411–418.
33. Johnson, B. K.; Prud'homme, R. K., Mechanism for rapid self-assembly of block copolymer nanoparticles. *Phys Rev Lett* **2003**, *91* (11), 118302.
34. Avgoustakis, K., Pegylated poly(lactide) and poly(lactide-co-glycolide) nanoparticles: preparation, properties and possible applications in drug delivery. *Curr Drug Deliv* **2004**, *1* (4), 321-33.
35. Chou, T. C., Theoretical basis, experimental design, and computerized simulation of synergism and antagonism in drug combination studies. *Pharmacol Rev* **2006**, *58* (3), 621-81.
36. Reese, D. M.; Tchekmedyian, S.; Chapman, Y.; Prager, D.; Rosen, P. J., A phase II trial of irinotecan in hormone-refractory prostate cancer. *Invest New Drugs* **1998**, *16* (4), 353-9.

Chapter 6 - Putting all together: Microfluidic Platform for Combinatorial Synthesis and Optimization of Targeted Nanoparticles for Cancer Therapy

6.1. Introduction

Nanoparticles (NPs) able to encapsulate and deliver thousands of drug molecules per particle hold tremendous potential for treating various diseases such as cancer, inflammation and infectious diseases¹. Despite the high level of activity and enthusiasm focused on the development of NP therapeutics over the past 30 years, very few nanoparticle formulations have reached clinical translation and human impact². In fact, while there are myriads of proof-of-concept studies presenting novel NPs that target and kill cancer cells, there are significantly fewer examples where the engineering and optimization is carried out to reach clinical translation. This is due in part by the complexity of nanoparticle optimization, since for every disease type one needs to find the optimal interplay of biophysicochemical parameters (e.g. size, charge, surface composition, etc.) that simultaneously confer molecular targeting, immune

evasion and controlled drug release^{3,4}. In addition, technology platforms for the rapid synthesis of nanoparticles with a wide range of properties in a reproducible manner are only now starting to emerge⁵⁻⁷.

Microfluidics, the science and technology of manipulating nanoliter volumes in microscale fluidic channels, has impacted a range of applications including biological analysis, chemical synthesis, single cell analysis, and tissue engineering⁸. In nanomedicine, microfluidics has enabled the synthesis of nanoparticles with narrower size distributions, improved batch-to-batch reproducibility, and higher drug loadings^{9, 10}. Some key advantages of microfluidics include simplicity and reproducibility in fabrication; availability of various inexpensive materials for fabrication such as PDMS; and lower cost of resources, since only few micrograms of materials and few microliters of solvents are needed to obtain well-defined products. These advantages make the use of microfluidics ideal for the development of a platform that enables the rapid synthesis and optimization of nanoparticles¹¹.

In the present work, inspired by the combinatorial high-throughput synthesis of small molecules^{12, 13} and novel biomaterials¹⁴, we have developed a microfluidic platform for the combinatorial high-throughput synthesis of nanoparticles. In this system a number of nanoparticle precursors enter the system and a library of nanoparticles with distinct properties exits it. First, we demonstrate that this system allows for the synthesis of nanoparticle with a wide range of properties, with batch-to-batch reproducibility. Next, we show high-throughput synthesis and screening capabilities by rapidly synthesizing 45 different formulations with different sizes and PEG coverage, screening them for macrophage uptake *in vitro*, and comparing the results with *in vivo* pharmacokinetic studies. Finally, with the aim of further understanding the role of active targeting in nanoparticles, we use the microfluidic system to

synthesize targeted and non-targeted NPs with similar biophysicochemical properties and compare tumor accumulation *in vivo*. These studies have broad implications in nanomedicine, where such a platform can be used to rapidly optimize promising novel lipid and polymeric nanoparticles and move them quickly to pre-clinical studies.

6.2. Design and operation of microfluidic platform

Our microfluidic platform is composed of a multi-inlet mixing unit and a synthesis unit (Figure 6.1A). In the former unit, a number of nanoparticle precursors dissolved in organic solvent are placed in different inlets and efficiently mixed at various ratios in a 3D micromixer (Figure 6.1B). In the latter unit each precursor combination is rapidly mixed with water using a technique called 3D hydrodynamic flow focusing, where the nanoparticle precursors are squeezed three-dimensionally to a thin stream that rapidly diffuses with water, resulting in self-assembly of nanoparticles through the process of nanoprecipitation¹⁵ (Figure 6.1C and 1D). Each micromixer inlet is connected to a syringe mounted on a programmable syringe pump, which allows accurately flowing the precursors at specific ratios that ultimately defines the physicochemical properties of the resulting NP. A photograph of the device is presented in figure 6.1E and a TEM micrograph of representative NPs obtained through these systems is shown in figure 6.1F. To synthesize a diverse library of NPs, we used 15 different precursors based on poly(lactic-co-glycolic) acid-co-polyethylene glycol (PLGA-PEG). These included, PLGA-PEG with different end-functional groups (e.g. amine, carboxyl, methoxy), PLGA MWs (10k Da, 27kDa, 45kDa, and 95kDa), and PEG MWs (2kDa, 5kDa, and 10kDa); PLGA-PEG functionalized with a ligand (LIG) targeted to PSMA receptors overexpressed prostate cancer cell^{16, 17}; and PLGA with different fluorescent probes for NP detection (Figure A4.1).

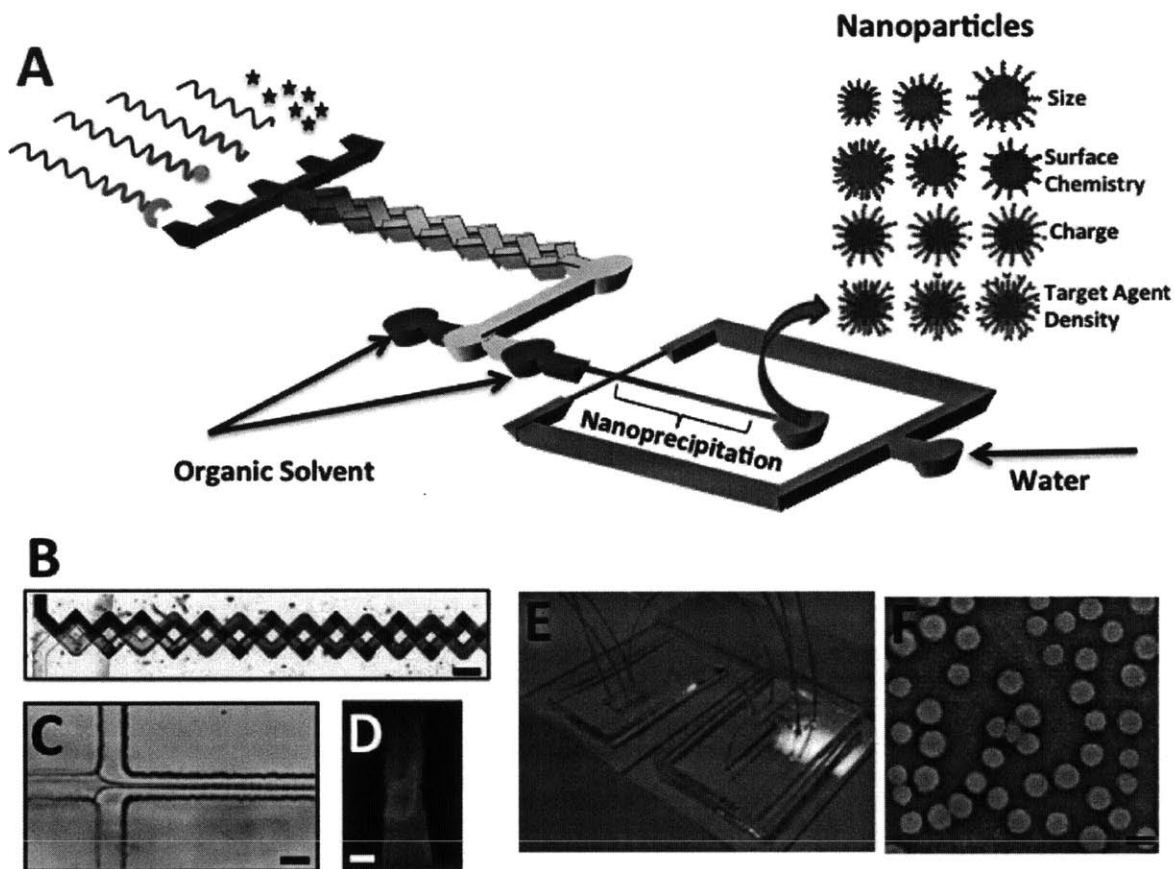


Figure 6.1. Microfluidic platform for high-throughput synthesis of nanoparticles.

(A) Schematic of system where NP precursors enter a multi-inlet mixer at different ratios producing a library of NPs upon self-assembly. (B) Mixer in operation showing complete mixing of streams at the end of the mixer. (C) Image of hydrodynamic flow-focusing where NPs self-assemble through nanoprecipitation. Scale bar = 20mm. (D) Image of vertical focusing of organic streams with polymeric precursors by two acetonitrile sheath streams. Scale bar = 10mm. (E) Image of microfluidic system with blue dye for visualization purposes. (F) Image of representative NPs produced by the system. Scale bar = 50nm.

6.3. Synthesis of nanoparticle library

To demonstrate the versatility of the platform, we synthesized a number of NPs spanning a wide range of physicochemical properties by strategically mixing ratios of different NP precursors. For instance, to vary the NP size we mixed PLGA-PEG with different PLGA MW ranging from 10kDa to 95kDa, resulting in sizes ranging from 25nm up to 200nm (Figure 6.2A).

For varying surface charge, previous studies reported that NPs comprised of PLGA-PEG-NH₂ exhibited a zeta potential of +10 to 15 mV while NPs comprised of PLGA-PEG-COOH exhibited a zeta potential of -10 to -15 mV, and those comprised of PLGA-PEG-OCH₃ remained neutral^{18, 19}. Therefore, by mixing polymers solutions containing, for instance, OCH₃ and COOH one can tune the surface charge from highly negative to neutral (Figure 6.2B). For varying surface ligand density, we mixed PLGA-PEG-LIG with unmodified PLGA-PEG at different ratios resulting in estimated ligand densities on the order of 10³-10⁵ ligands per micron square (i.e. ~10¹-10³ ligands per NP²⁰) (Figure 6.2C). Finally, for varying the final drug loading of the polymer, using docetaxel as model drug, we adjusted both the initial drug loading and the polymer concentration in acetonitrile—factors that were previously published to affect drug loading^{21, 22}. In this case, we had in one stream the drug, PLGA-PEG of a specific MW at 50mg/mL in another, and plain acetonitrile in the third one to modify the concentration from 50mg/mL down to 10mg/mL. Furthermore, other NP physicochemical properties that could be varied with these precursors but not shown here include drug release kinetics (by using PLGA with different ratios of LA:GA or different PLGA MW²²) and PEG density (by adding PLGA-PEG with a PEG block of different lengths or by varying the ratio of PLGA-PEG and free PLGA²³). Finally, these NPs could be prepared with excellent batch-to-batch reproducibility and much narrower size distributions compared to bulk synthesis (Figure A4.2). These results verify that by combinatorially mixing a number of NP precursors, mostly based from the same polymer PLGA-PEG, one can reproducibly produce a library of NPs spanning virtually the entire phase space of NP properties.

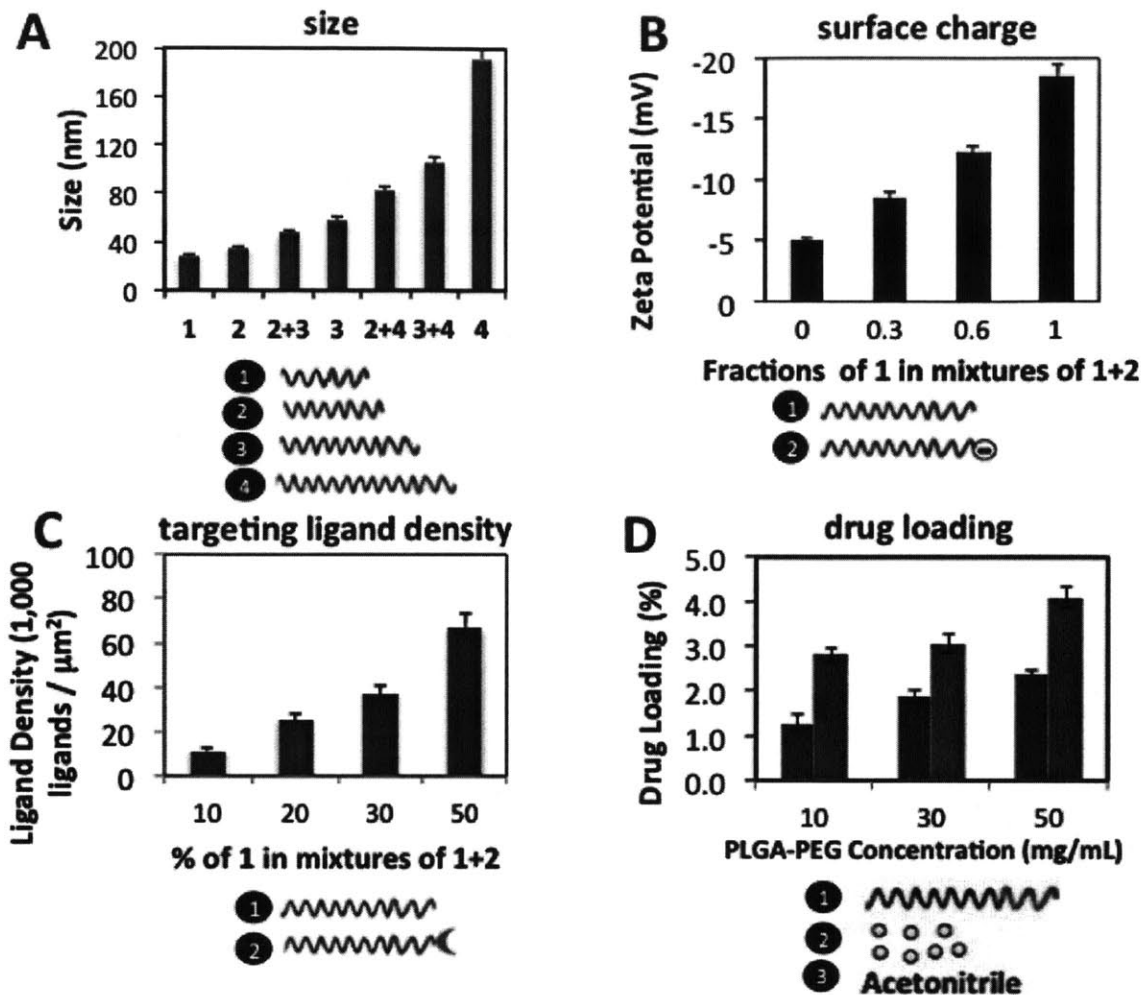


Figure 6.2. Synthesis of NPs with control over physicochemical properties.

(A) Variation of NP size by mixing polymers with different PLGA MW (from 10kDa to 95kDa). (B) Variation of NP surface charge by mixing polymers with different end functional group on the PEG block. Carboxyl group ($-\text{COOH}$) is negatively charged while methoxy group ($-\text{OCH}_3$) is neutral. (C) Variation of targeting ligand density by mixing polymers functionalized with targeting ligand together with unmodified polymer. (D). Variation of drug loading by mixing a polymer at a high concentration (50mg/mL) with different ratios of drug (to vary initial drug loading) and plain acetonitrile (to vary concentration). Legend: Blue block = PEG; Red block = PLGA.

6.4. High-throughput synthesis and screening of nanoparticles

Next, to show the utility of our system for high-throughput synthesis and screening of NPs, we picked 7 polymers containing different PLGA and PEG MWs as well as free PLGA to synthesize a library of NPs comprised of 45 different formulations with different size and PEG coverage. For the screening, we used an established *in vitro* macrophage binding and uptake assay²⁰, in which the extent of interaction between macrophages and nanoparticles depends on the NP physicochemical properties. In this assay, fluorescently labeled NPs were incubated with macrophages in 96-wells plates and then analyzed with flow cytometry using a high-throughput robotic sampler. Depending on the particle dosing per well and number of repeats per formulation, the time to synthesize 45 formulations may take from minutes to hours. In our case, the synthesis of 45 NP formulations that were dosed at 100mg of NPs per well at n=3, took close to 70 minutes—whereas by conventional pipetting it could take up to 10 times longer⁷. Figure 6.3A shows, the fluorescence intensity associated with NP binding and uptake by macrophages for the 45 formulations. For each formulation, we also measured NP size, estimated the PEG weight %, and reported the average PEG length. These results, indicate that NP formulations of small size (25-30nm), relatively high PEG wt. % (up to 33%) and longer PEG molecules (up to 10kDa) are the ones taken up least by macrophages, which agree with previous results reported on PEGylated NPs^{24, 25}. Additionally, it was observed that NP size was a key determinant in macrophage association more so than PEG coverage. For instance, a 30nm NP with PEG length of 5kDa was taken up less than a 50nm NP with length 10kDa. Again, coupling microfluidic

high-throughput synthesis with conventional high-throughput screening methods, a large number of NPs can be evaluated in a relative short amount of time.

In the body, NPs tend to be taken by the mononuclear phagocytic system (MPS) mostly present in the liver and the spleen, which directly affect their the circulation time²⁶. Thus, NP association with macrophages generally provides an idea of pharmacokinetic behavior of NPs. To evaluate this hypothesis, we selected 4 formulations showing different macrophage uptake behaviors and investigated their pharmacokinetic profile in vivo. For this experiment we increased the scale of production two orders of magnitude from hundreds of micrograms to tens of milligrams by simply programming the microfluidic system to run for a longer period of time. Interestingly, the NP properties remained essentially identical across batches of different scales, which we consider it a key advantage of the system. Figure 6.3B shows the pharmacokinetic profile of selected NP formulations that exhibited increasing macrophage uptake. Analysis of the PK profile revealed that the NP formulation with lowest macrophage uptake had the longest half-life (Figure 6.3C) and greatest area under the curve (AUC) (Figure 6.3D). These results confirm the hypothesis that NPs with higher interactions with macrophages would tend to circulate in blood for a shorter amount of time²⁷⁻²⁹. Consequently, our method to reproducibly synthesize NPs together with the in vitro macrophage uptake assay might be useful for selecting promising NP formulation for pre-clinical evaluation with respect to circulation time, as well as to identify which formulations have a high probability of not working in vivo—which can save significant amount of time and resources later on.

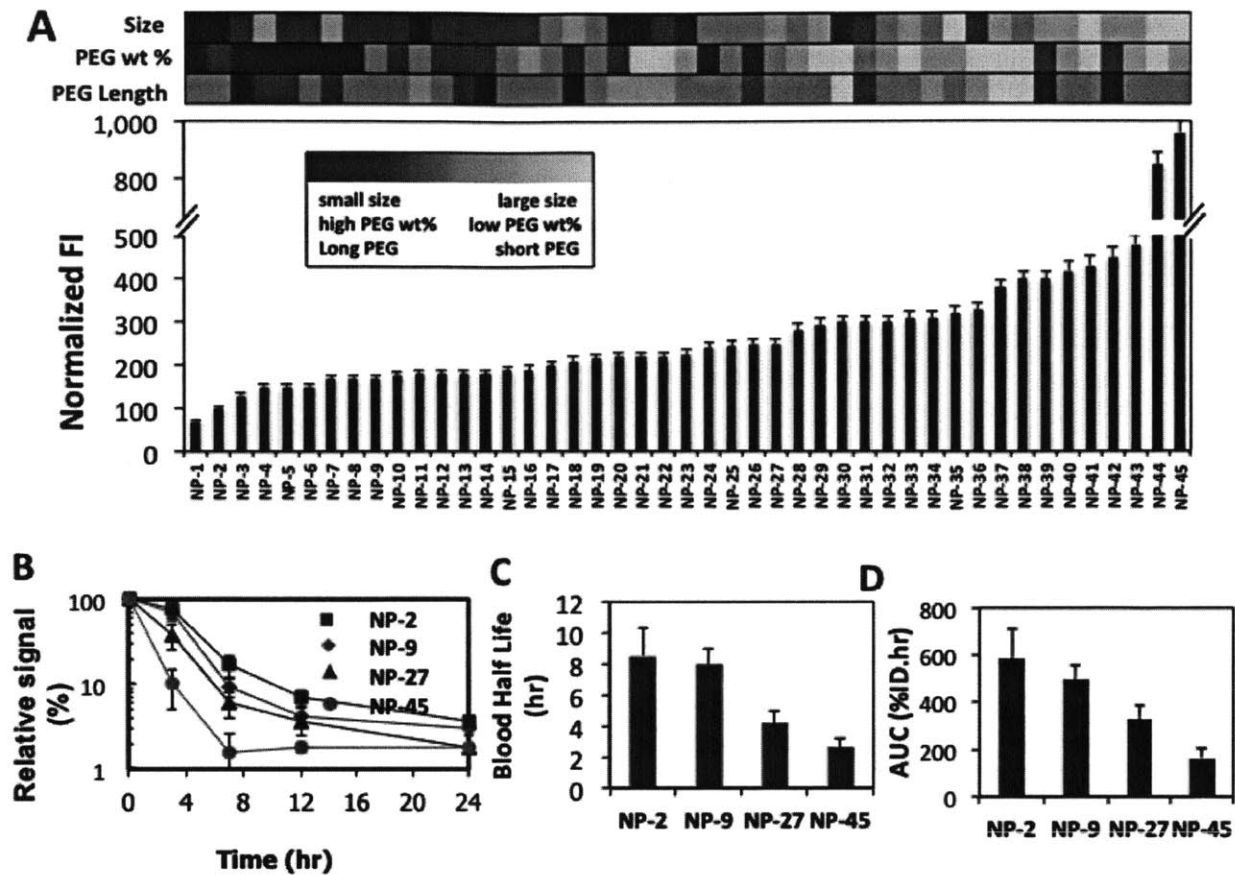


Figure 6.3. Synthesis and in vitro and in vivo screening of 45 NPs with different sizes and PEG coverage.

(A) Fluorescent intensity (FI) of macrophages associated with of Alexa-488-labeled NPs. Heat map indicating extent of size, PEG weight % and average PEG length for each formulation. (B) Pharmacokinetic profile measured by the relative fluorescence of Alexa-647-labeled NPs in blood. (C) Circulation half-life and (D) area under the curve of selected formulations with increasing macrophage binding and uptake.

6.5. Passive versus active nanoparticle targeting

Finally, we used the microfluidic system to obtain a deeper understanding of the biological behavior of NPs in vivo, specifically to shed light on the effects of NP passive versus active targeting on tumor accumulation. The existing paradigm behind passive targeting is that NPs can selectively extravasate the leaky vasculature of the tumor via the so-called enhanced

permeation and retention (EPR) effect simply by remaining in the circulation for sufficiently long times³⁰. In contrast, the rationale behind active targeting is that decoration of the NPs with homing molecules will confer them with more specificity for the cancer cells, and thus they will preferentially distribute in the tumor tissues³⁰. However, many of the studies comparing passive versus active targeting tend to focus on NPs whose physicochemical properties were modified upon the addition of the targeting ligand (e.g. size and charge). This has led to mixed results across studies where the role of active targeting is still debated³¹. In the present work, we used the microfluidic platform to synthesize an actively targeted NP (TNP) with similar properties as its passively targeted counterpart (herein called non-targeted NP) with respect to size and charge, which is difficult to do in bulk. First, we rapidly synthesized TNPs with different ligand densities, followed by screening them in vitro against LNCaP cells overexpressing PSMA receptors, as well as macrophages. The goal was to find TNPs with higher uptake by LNCaP cells, yet similar macrophage uptake as the non-targeted NPs. Figure 6.4A and 6.4B show the cancer cell and macrophage uptake, respectively, for five different formulations containing increasing amounts of ligands on the NP surface. The results indicated that when adding up to 20 molar % of PLGA-PEG-LIG to the NP formulation, a significantly increase in fold uptake by cancer cells was observed, yet there was only a small difference in macrophage uptake compared to non-targeted NPs. In addition, the average size and charge of NPs with up to 20 molar % of PLGA-PEG-LIG exhibited essentially the same size and charge as the one with just PLGA-PEG (40 nm and -0.5 mV) (Figure A4.3). Thus, for subsequent in vivo studies we chose as TNP the one comprised of 20 molar % which corresponds approximately to 200 ligands per NP. For the in vivo studies, we implanted 1×10^7 LNCaP cells to the flank of the mouse and let the tumor grow for 3-4 weeks until the tumor reached a size of close 100 mm³. Non-targeted NPs and

TNPs labeled with Alexa647 were injected via tail vein. After 24 hours the animals were sacrificed and the fluorescence of the main organs was measured (Figure 6.4C). While the fluorescent signal in most of the organs was similar for both formulations, the two main differences were observed for the spleen and for the tumor, where TNP showed significantly higher accumulation in tumor and less in the spleen versus the non-targeted one. In fact, the signal accumulation of TNPs tumor was close to 3.5-fold that of the non-targeted NP (figure 6.4D). These results suggest that active targeting of NPs does make a significant impact in the accumulation of NPs in the tumor when compared to non-targeted ones with similar biophysicochemical properties. While further studies should be carried out to investigate the kinetics of tumor accumulation, these preliminary results illustrate the importance of active targeting and their benefits in tumor accumulation.

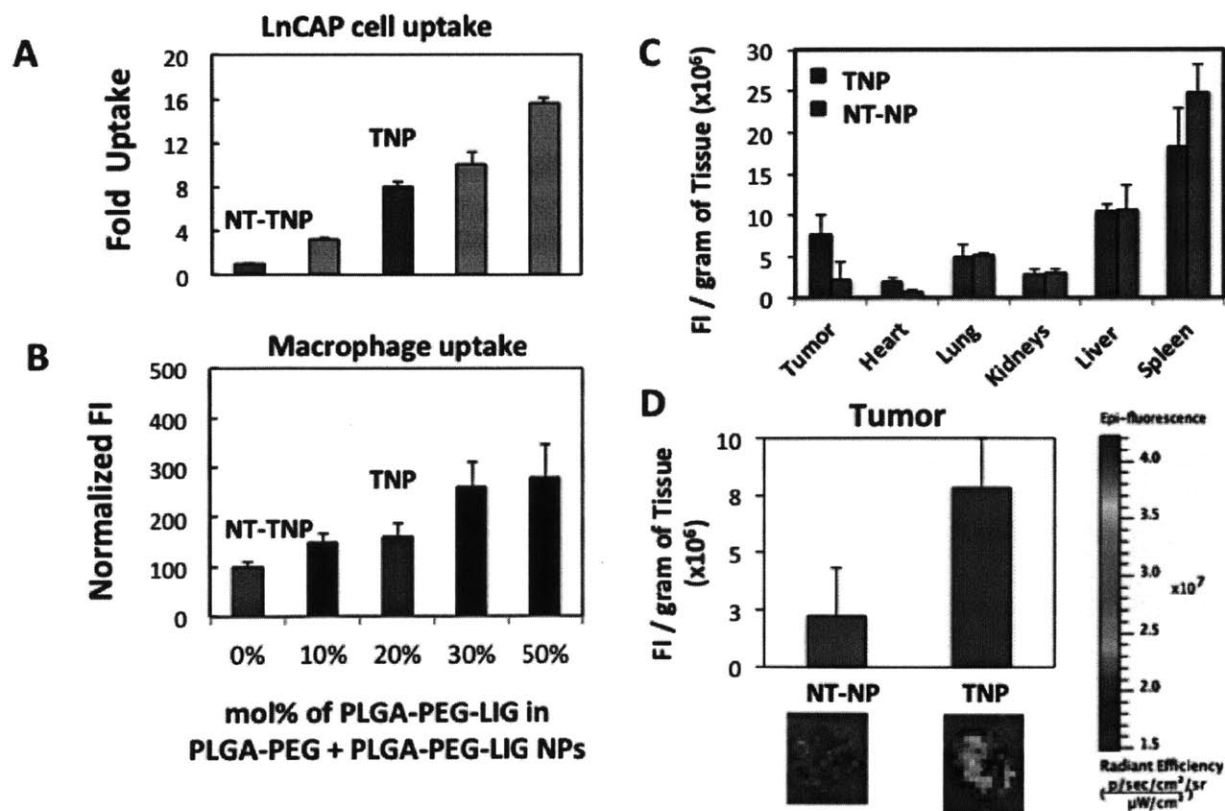


Figure 6.4. Comparison of biodistribution and tumor accumulation of targeted and non-targeted NPs with similar biophysicochemical properties.

(A) Fluorescent intensity of Alexa-488 labeled targeted NPs associated with macrophages. (B) Fold-uptake of targeted NPs by LNCaP measured by the fluorescent signal of targeted NPs over that of non-targeted NPs. (C) Biodistribution and (C) tumor accumulation of a targeted NP composed of 20% molar PLGA-PEG-LIG compared to non-targeted NP.

6.6. Conclusion

We reported a new microfluidic platform for the combinatorial, high-throughput synthesis of targeted polymeric nanoparticles. The system coupled with high-throughput conventional multi-well plate assays has the potential to accelerate the engineering and optimization of NPs against a specific target. It was first demonstrated that NPs with a wide range of properties can be generated by making a small library comprised of NPs with size from 25-200nm, zeta potential from -20 to +20 mV, ligand density from 0 to $\sim 10^5$ ligands/mm², and drug loading from 0 to 5%. Subsequently, we showed the high-throughput capabilities of the system by rapidly synthesizing 45 NP formulations of different sizes and PEG coverage, and screened them against macrophage uptake in vitro. Finally we performed both in vitro and in vivo proof-of-concept screenings to investigate the relation of macrophage uptake in vitro with pharmacokinetics in vivo (where low macrophage uptake correlates with longer circulation time), as well as investigate the tumor accumulation of targeted NPs versus non-targeted NPs of essentially identical biophysicochemical properties (where targeted NPs accumulate 3.5-fold in tumor versus non-targeted ones). Three key advantages of our system over existing bulk synthesis include (i) from a small set of NP precursors one can rapidly synthesize a NP library with a wide range of distinct physicochemical properties; (ii) the NPs prepared have high batch-to-batch reproducibility and lower polydispersity; (iii) NPs prepared at the microgram range have

the exact same properties are those prepared at the milligram range. These advantages allow for screenings both in vitro and in vivo with the goal of either accelerating the clinical translation of a specific formulation or obtain deeper fundamental understanding on the correlation of NP properties and biological behavior.

6.7. Materials and methods

Fabrication of Microfluidic System. The prototypical system was manufactured using the standard soft-lithographic technique, described in previous work²³. Briefly, SU-8 (MicroChem) resist was spun on a bare 4" silicon wafer and prebaked on a hot plate. After exposure to 365 nm UV light, the coated wafer was post-baked, resulting in the master mold. PDMS (Sylgard 184, Dow Corning) monomer and curing agent were mixed in a ratio of 10:1 by weight, poured over the silicon master mold, and degassed. After curing at 100 °C for 60 min, PDMS cast was carefully removed from the mold. The multi-inlet mixing unit was composed of two layers that were aligned and bonded together after placing each layer in plasma for 30 s. Inlets and outlet holes were drilled followed by placing the PDMS glass slide using air plasma. NP synthesis unit was composed of a single layer with inlet holes precisely drilled next to each other to achieve 3D flow focusing¹⁵. Typical channel dimensions used in the NP synthesis experiments had a width of 100 μm and a height of 60 μm for the vertical focusing part and had a width of 20 μm for the horizontal focusing part, or precipitation channel. The outlet of the mixer unit was connected to the middle inlets in the NP synthesis units while the side inlets were collected to syringes containing acetonitrile.

Nanoparticle precursors. PLGA-PEG-LIG was synthesized as previously reported¹⁷. Briefly, LIG was dissolved in 400 μL of dimethylformamide (DMF) and allowed to react with tBOC-NH-PEG-NHS in the presence of *N,N*-diisopropylethylamine (DIEA). The reaction product was

dialyzed for 24 h in water to remove unreacted LIG, then lyophilized, and finally resuspended in trifluoroacetic acid (TFA) to remove tBOC. Subsequently, PEG-LIG was dried and dissolved in DMSO. In parallel, PLGA-COOH was allowed to react with N-hydroxysuccinimide (NHS) in the presence of 1-ethyl-3-[3-dimethylaminopropyl] carbodiimide (EDC) in dichloromethane (DCM). The resulting PLGA-NHS was dried and dissolved in DMSO. Finally, PEG-LIG and PLGA-NHS in DMSO were mixed with DIEA, allowed to react, precipitated in cold methanol, and dried under vacuum.

Synthesis of PLGA-PEG was accomplished using EDC/NHS chemistry²¹. For PLGA-PEG with PEG of different PEG MWs and PEG functional groups was accomplished by conjugation of PLGA homopolymer with a carboxylate end-group to a monofunctional methoxy-PEG_x-NH₂, where x indicates PEG MW (2k, 5k, and 10k). For PLGA-PEG functionalized with carboxyl and amine groups, difunctional NH₂-PEG-COOH and NH₂-PEG-NH₂ were used, respectively (Laysan Bio, Arab, AL). Briefly, PLGA-Carboxylate was dissolved in DCM, followed by the addition of NHS and EDC to the solution. After 2 h the resulting product, PLGA-NHS, was precipitated in ethyl ether/methanol, collected by centrifugation, and drying under vacuum. PLGA-NHS was dissolved in DCM followed by addition of monofunctional or difunctional PEG together with DIEA. The resulting PLGA-PEG block copolymer was precipitated with ether/methanol washing solvent and washed with the same solvent to remove unreacted PEG.

The synthesis of PLGA-Alexa488 and PLGA-Alexa647 were accomplished by the conjugation of an activated PLGA-COOH with Alexa-488/647 Cadaverin through EDC/NHS conjugation. First, Alexa-488/647 was dissolved in 1 mL of DMF. Concurrently, PLGA-COOH (was mixed with EDC and NHS in 500 mL of DMF. Finally, PLGA solution was reacted with Alexa-

488/647 solution for 16 h at room temperature. The reaction product was precipitated in ice cold methanol and dried under vacuum.

Finally, PLGA-PEG with PLGA MWs of 27kDa, 45kDa, and 95kDa were purchased from Boehringer Ingelheim GmbH (Germany). PLGA-PEG with PLGA MW of 10kDa was purchased from Akina Inc (West Lafayette, IN). Unmodified PLGA with different MWs were purchased from Lactel (Pelham, AL).

Nanoparticle Synthesis and Characterization. NPs were prepared by nanoprecipitation¹⁵. Briefly, the organic stream (polymers and drugs) was run at 7 mL/min, vertical sheath streams (acetonitrile) were run at 3 mL/min while maintaining a total aqueous flow rate of 50 mL/min. NPs were collected at the outlet stream and washed three times with water using Amicon centrifugation filtration membrane to remove excess drugs and organic solvents. Dynamic light scattering (DLS) was used to determine particle size and size distribution, using a Zetasizer Nano ZS instrument (Malvern Instruments Ltd., U.K.). Particle visualization was carried out through TEM (JEOL 2011 instrument at an acceleration voltage of 200 kV). Drug loading and encapsulation efficiency (EE) were determined by quantifying the amount of docetaxel in the NP by dissolving them in a 50/50 acetonitrile/water solution immediately after synthesis and vortexed for several hours to induce NP dissociation. The amount of docetaxel inside the NPs was quantitated by HPLC with a UV reader at a wavelength of 267 nm. A calibration curve with known concentrations of docetaxel was prepared, and the amount of drug encapsulated in the NPs was calculated accordingly.

Nanoparticle Binding and Uptake by RAW264.7 and LNCaP cells. RAW 264.7 cells were cultured in DMEM medium with 10% fetal bovine serum, 50 units/mL penicillin and 50 mg/mL streptomycin. LNCaP cells were cultured in RPMI medium with 10% fetal bovine serum, 50

units/mL penicillin and 50 mg/mL streptomycin. Cells were seeded at a density of 50,000 cells per well on a 24-well plate. After 24 h, the cell medium was removed and replaced with NPs dissolved in the same medium at a concentration of 1 mg/mL. Cells and NPs were incubated for 4 h for the case of RAW 264.7 and LNCaP, followed by three washes with 1% BSA solution in PBS to remove excess NPs. RAW264.7 cells were removed from the plate using a cell scraper and centrifuged, while LNCaP cells were treated with trypsin, removed from the plate, and centrifuged. The resultant cell pellets were reconstituted in 250 μ L of PBS and placed on a 96-well plate for FACS analysis. Flow cytometry analysis was performed on a BD Biosciences LSR II with High-Throughput sampler (HTS) option, with 10,000 cells were collected for each measurement.

Pharmacokinetics and Biodistribution Studies. All animal studies were conducted under the supervision of MIT's Division of Comparative Medicine in compliance with the NIH's Principles of Laboratory Animal Care. For Pharmacokinetic studies wild-type Balb/c mice (Charles River Laboratories). Fluorescently labeled NPs (with Alexa-647) were injected via tail vein in groups of 4 mice per formulation. At different time points, few microliters of blood were sampled from the mouse and the fluorescence measured using IVIS imaging system. As a control, blood from mice with no NPs injected were used and the background fluorescence was measured. Plasma half-life was determined using the method described by H. Cabral et al³², whereas area under the curve was calculated by integrating the PK profile using the trapezoid method. For biodistribution studies, the xenograft tumor-bearing mouse model was constructed by inoculating 1×10^7 cells/0.2 mL freshly prepared from cell cultures and mixed with matrigel. The cells employed will be luciferase-expressing LNCaP cells (LNCap-luc), which allow for continuously monitoring the growth of the tumor by whole-animal luminescent imaging.

Tumor was allowed to grow for 3-4 weeks until it reached a size of close 100 mm³. NPs labeled with Alexa-647 were injected via tail vein in groups of 5 per NP formulation. After 24 h the animals were sacrificed, main organs were excised, weighted and their fluorescence was measured using IVIS.

6.8. References

1. Peer, D.; Karp, J. M.; Hong, S.; Farokhzad, O. C.; Margalit, R.; Langer, R., Nanocarriers as an emerging platform for cancer therapy. *Nat Nanotechnol* **2007**, *2* (12), 751-60.
2. Shi, J.; Xiao, Z.; Kamaly, N.; Farokhzad, O. C., Self-Assembled Targeted Nanoparticles: Evolution of Technologies and Bench to Bedside Translation. *Acc Chem Res* **2011**.
3. Hrkach, J.; Von Hoff, D.; Ali, M.; Andrianova, E.; Auer, J.; Campbell, T.; de Witt, D.; Figa, M.; Figueiredo, M.; Horhota, A.; Low, S.; McDonell, K.; Peeke, E.; Retnarajan, B.; Sabnis, A.; Schnipper, E.; Song, J.; Song, Y. H.; Summa, J.; Tompsett, D.; Troiano, G.; van Geen, T.; Wright, J.; LoRusso, P.; Kantoff, P. W.; Bander, N. H.; Sweeney, C. J.; Farokhzad, O. C.; Langer, R.; Zale, S., Preclinical Development and Clinical Translation of a PSMA-Targeted Docetaxel Nanoparticle with a Differentiated Pharmacological Profile. *Sci Transl Med* **2012**, *4*.
4. Murday, J. S.; Siegel, R. W.; Stein, J.; Wright, J. F., Translational nanomedicine: status assessment and opportunities. *Nanomedicine* **2009**, *5* (3), 251-73.
5. Chan, E. M.; Xu, C.; Mao, A. W.; Han, G.; Owen, J. S.; Cohen, B. E.; Milliron, D. J., Reproducible, high-throughput synthesis of colloidal nanocrystals for optimization in multidimensional parameter space. *Nano Lett* **2010**, *10* (5), 1874-85.
6. Kim, Y.; Lee Chung, B.; Ma, M.; Mulder, W. J.; Fayad, Z. A.; Farokhzad, O. C.; Langer, R., Mass Production and Size Control of Lipid-Polymer Hybrid Nanoparticles through Controlled Microvortices. *Nano Lett* **2012**, *12* (7), 3587-91.
7. Wang, H.; Liu, K.; Chen, K. J.; Lu, Y.; Wang, S.; Lin, W. Y.; Guo, F.; Kamei, K.; Chen, Y. C.; Ohashi, M.; Wang, M.; Garcia, M. A.; Zhao, X. Z.; Shen, C. K.; Tseng, H. R., A rapid pathway toward a superb gene delivery system: programming structural and functional diversity into a supramolecular nanoparticle library. *ACS Nano* **2010**, *4* (10), 6235-43.
8. Whitesides, G. M., The origins and the future of microfluidics. *Nature* **2006**, *442* (7101), 368-73.
9. Jahn, A.; Reiner, J. E.; Vreeland, W. N.; DeVoe, D. L.; Locascio, L. E.; Gaitan, M., Preparation of nanoparticles by continuous-flow microfluidics. *Journal of Nanoparticle Research* **2008**, *10* (6), 925-934.
10. Chen, D.; Love, K. T.; Chen, Y.; Eltoukhy, A. A.; Kastrup, C. J.; Sahay, G.; Jeon, A.; Dong, Y.; Whitehead, K. A.; Anderson, D. G., Rapid Discovery of Potent siRNA-Lipid-Nanoparticles Enabled by Controlled Microfluidic Formulation. *J Am Chem Soc* **2012**.
11. Valencia, P. M.; Farokhzad, O. C.; Karnik, R.; Langer, R., Microfluidic technologies for accelerating the clinical translation of nanoparticles. *Nat Nanotechnol* **2012**, *7* (10), 623-9.
12. Dolle, R. E., Historical overview of chemical library design. *Methods Mol Biol* **2011**, *685*, 3-25.

13. Macarron, R.; Banks, M. N.; Bojanic, D.; Burns, D. J.; Cirovic, D. A.; Garyantes, T.; Green, D. V.; Hertzberg, R. P.; Janzen, W. P.; Paslay, J. W.; Schopfer, U.; Sittampalam, G. S., Impact of high-throughput screening in biomedical research. *Nat Rev Drug Discov* **2011**, *10* (3), 188-95.
14. Siegwart, D. J.; Whitehead, K. A.; Nuhn, L.; Sahay, G.; Cheng, H.; Jiang, S.; Ma, M.; Lytton-Jean, A.; Vegas, A.; Fenton, P.; Levins, C. G.; Love, K. T.; Lee, H.; Cortez, C.; Collins, S. P.; Li, Y. F.; Jang, J.; Querbes, W.; Zurenko, C.; Novobrantseva, T.; Langer, R.; Anderson, D. G., Combinatorial synthesis of chemically diverse core-shell nanoparticles for intracellular delivery. *Proc Natl Acad Sci U S A* **2011**, *108* (32), 12996-3001.
15. Rhee, M.; Valencia, P. M.; Rodriguez, M. I.; Langer, R.; Farokhzad, O. C.; Karnik, R., Synthesis of size-tunable polymeric nanoparticles enabled by 3D hydrodynamic flow focusing in single-layer microchannels. *Adv Mater* **2011**, *23* (12), H79-83.
16. Chandran, S. S.; Banerjee, S. R.; Mease, R. C.; Pomper, M. G.; Denmeade, S. R., Characterization of a targeted nanoparticle functionalized with a urea-based inhibitor of prostate-specific membrane antigen (PSMA). *Cancer Biol Ther* **2008**, *7* (6), 974-82.
17. Valencia, P. M.; Basto, P. A.; Zhang, L.; Rhee, M.; Langer, R.; Farokhzad, O. C.; Karnik, R., Single-step assembly of homogenous lipid-polymeric and lipid-quantum dot nanoparticles enabled by microfluidic rapid mixing. *ACS Nano* **2010**, *4* (3), 1671-9.
18. Salvador-Morales, C.; Zhang, L.; Langer, R.; Farokhzad, O. C., Immunocompatibility properties of lipid-polymer hybrid nanoparticles with heterogeneous surface functional groups. *Biomaterials* **2009**, *30* (12), 2231-40.
19. Valencia, P. M.; Hanewich-Hollatz, M. H.; Gao, W.; Karim, F.; Langer, R.; Karnik, R.; Farokhzad, O. C., Effects of Ligands with Different Water Solubilities on Self-Assembly and Properties of Targeted Nanoparticles. *Biomaterials* **2011**, (*in press*).
20. Cheng, J.; Teply, B. A.; Sherifi, I.; Sung, J.; Luther, G.; Gu, F. X.; Levy-Nissenbaum, E.; Radovic-Moreno, A. F.; Langer, R.; Farokhzad, O. C., Formulation of functionalized PLGA-PEG nanoparticles for in vivo targeted drug delivery. *Biomaterials* **2007**, *28* (5), 869-76.
21. Avgoustakis, K., Pegylated poly(lactide) and poly(lactide-co-glycolide) nanoparticles: preparation, properties and possible applications in drug delivery. *Curr Drug Deliv* **2004**, *1* (4), 321-33.
22. Karnik, R.; Gu, F.; Basto, P.; Cannizzaro, C.; Dean, L.; Kyei-Manu, W.; Langer, R.; Farokhzad, O. C., Microfluidic platform for controlled synthesis of polymeric nanoparticles. *Nano Lett* **2008**, *8* (9), 2906-12.
23. Ma, L. L.; Jie, P.; Venkatraman, S. S., Block copolymer 'stealth' nanoparticles for chemotherapy: Interactions with blood cells in vitro. *Adv Funct Mater* **2008**, *18* (5), 716-725.
24. Gref, R.; Luck, M.; Quellec, P.; Marchand, M.; Dellacherie, E.; Harnisch, S.; Blunk, T.; Muller, R. H., 'Stealth' corona-core nanoparticles surface modified by polyethylene glycol (PEG): influences of the corona (PEG chain length and surface density) and of the core composition on phagocytic uptake and plasma protein adsorption. *Colloids Surf B Biointerfaces* **2000**, *18* (3-4), 301-313.
25. Bertrand, N.; Leroux, J. C., The journey of a drug-carrier in the body: An anatomophysiological perspective. *J Control Release* **2011**.
26. Shan, X.; Liu, C.; Yuan, Y.; Xu, F.; Tao, X.; Sheng, Y.; Zhou, H., In vitro macrophage uptake and in vivo biodistribution of long-circulation nanoparticles with poly(ethylene-glycol)-modified PLA (BAB type) triblock copolymer. *Colloids Surf B Biointerfaces* **2009**, *72* (2), 303-11.

27. Sheng, Y.; Yuan, Y.; Liu, C.; Tao, X.; Shan, X.; Xu, F., In vitro macrophage uptake and in vivo biodistribution of PLA-PEG nanoparticles loaded with hemoglobin as blood substitutes: effect of PEG content. *J Mater Sci Mater Med* **2009**, *20* (9), 1881-91.
28. Perry, J. L.; Reuter, K. G.; Kai, M. P.; Herlihy, K. P.; Jones, S. W.; Luft, J. C.; Napier, M.; Bear, J. E.; Desimone, J. M., PEGylated PRINT Nanoparticles: The Impact of PEG Density on Protein Binding, Macrophage Association, Biodistribution, and Pharmacokinetics. *Nano Lett* **2012**, *12* (10), 5304-10.
29. Kamaly, N.; Xiao, Z.; Valencia, P. M.; Radovic-Moreno, A. F.; Farokhzad, O. C., Targeted polymeric therapeutic nanoparticles: design, development and clinical translation. *Chem Soc Rev* **2012**, *41* (7), 2971-3010.
30. Duncan, R.; Gaspar, R., Nanomedicine(s) under the microscope. *Mol Pharm* **2011**, *8* (6), 2101-41.
31. Valencia, P. M.; Pridgen, E.; Perea, B.; Gadde, S.; Sweeney, C.; Kantoff, P. W.; Bander, N. H.; Lippard, S. J.; Langer, R.; Karnik, R.; Farokhzad, O. C., Synergistic cytotoxicity of irinotecan and cisplatin in dual-drug targeted polymeric nanoparticles. *Nanomedicine* **2012**.
32. Cabral, H.; Matsumoto, Y.; Mizuno, K.; Chen, Q.; Murakami, M.; Kimura, M.; Terada, Y.; Kano, M. R.; Miyazono, K.; Uesaka, M.; Nishiyama, N.; Kataoka, K., Accumulation of sub-100 nm polymeric micelles in poorly permeable tumours depends on size. *Nat Nanotechnol* **2011**, *6* (12), 815-23.

Chapter 7 - Outlook: The Relationship Between Nanoparticles Properties and Biological Behavior—a Deep Dive.

7.1. Introduction.

Despite the advances in the field of NPs as drug carriers and thousands of related publications in the last 30 years, only remarkably few have made it to the bedside. The wide gap between bench discoveries and clinical translation can be partly explained by the lack of fundamental understanding of the strengths and limitations of both targeted and non-targeted NPs¹. While there is wide knowledge on a myriad of NP systems made of different materials and encapsulating a wide range of drugs against several model diseases, there is limited deep understanding on what set of NP properties results in highly effective therapeutics with low off-target toxicity. The goal would be to use the state-of-the art platform technology developed in this work as a tool to deepen the current understanding of NPs at different levels of interactions, mainly NP-proteins, NP-organs, and NP-body. We would aim to answer fundamental questions that would help us to elucidate the phenomena happening at different levels and how they are interrelated. Mainly we want to answer: **1)** how do NP physicochemical properties and protein

adsorption patterns correlate to circulation and tissue distribution kinetics? 2) What are the main NP characteristics affecting the accumulation of NPs in the tumor? 3) How does active targeting and drug release rates from NPs affect the kinetics of drug accumulation in the tumor and how does it compare to drug in its conventional dosage form?

7.2. What we have learned so far

Research in the last decades has cultivated a set of “rules of thumb” that guide scientists when designing of nanoscale drug delivery systems for cancer therapy. For instance, with respect to size, it is important to have a NP with a size >10 nm to avoid kidney filtration and <100 - 150 nm to minimize recognition by the organs of mononuclear phagocyte system (MPS) like the liver and spleen². NPs with neutral surface charges are preferred to minimize protein adsorption and activation of the complement system³. With respect to surface hydrophilicity, protective poly(ethylene glycol) (PEG) coatings are customary. PEG chains with a length of ~ 3000 - $10,000$ endow NPs with a “stealth hydrophilic layer” that results in the increase of NP circulation time. Usually, PEG coverage between 2-10% on the NP surface are sufficient to elicit this effect⁴. Finally, when targeting ligands are used, the optimal density on the surface is a balance between sufficiently abundant to increase cellular uptake and sufficiently dilute to maintain the surface properties and the stealth effect⁵. Essentially, the exact number depends on the nature of the ligand⁶. Nevertheless, recent studies have indicated that there is much more to these rules currently unknown and unexplored. For instance in some reports, negative charges on the NP noticeably contribute to MPS capture and clearance from the bloodstream⁷⁻⁹, while that effect is not observed in other studies¹⁰⁻¹³. Similarly while some studies demonstrated NP blood circulation time varies with NP size^{4, 14}, recent studies have shown that NP size did not affect the NP pharmacokinetics but only the biodistribution¹⁵. Furthermore, while some studies have

shown that active targeting (i.e., having a targeting ligand on the NP surface) increases NP tumor accumulation¹⁶, others have shown that active targeting affects intracellular delivery but not tumor accumulation¹⁷. This is a clear sign that these succinct design rules are simplistic in nature and that further understanding is required. For instance, even though it is known that NPs with a size between 10-100 nm can passively accumulate in tumors, within these limits, the size sensitivity of the kinetics of liver and spleen distribution is not known. Similarly, the influence of size and surface charge on the optimal PEG coverage (density and length) is not established either. In summary, while there is empirical understanding of the effects of NP properties on their biological behavior at a basic level, there is a lack of sufficiently comprehensive understanding to determine key design criteria and to consistently bring NPs to the clinic in a more effective way. Such knowledge would not only be useful to move current NP formulations from bench side to bedside, but could also allow us to design truly improved therapeutics that substantially increase the survival of cancer patients.

7.3. Three key research directions

Based on the aforementioned, we have identified three key problems that are very important on their own and when studied in concert, and that could provide substantially deeper understanding in the field: 1) Determining the relation of NP physicochemical properties to the kinetics of NP interactions with proteins in biological fluids *ex vivo*, and in different organs *in vivo*. 2) Understanding the impact of active targeting on the kinetics of tumor accumulation in a rigorous and unbiased way. 3) Understanding the kinetics of tumor's exposure to total and free drug with targeted and non-targeted NPs. These problems will be highlighted in more detail in the next paragraphs.

(1) The need for correlating NP physicochemical properties with ex vivo protein adsorption, and in vivo pharmacokinetics and biodistribution in all relevant organs: In general, pharmacokinetics and biodistribution of NPs directly relate to their physicochemical properties¹⁸⁻²⁰. Currently, the most common way to understand the effect of NP physicochemical properties to in vivo behavior is to characterize the NP properties in aqueous non-biological fluids, and correlate those properties to what is seen in vivo (e.g., circulation time, distribution to a specific organ, and/or efficacy). However, there is currently a large “black box” regarding key aspects of the NPs interactions with the body such as dynamic changes in NP properties upon contact with biological fluids and non-specific distribution in tissues such as liver, spleen, kidneys and lungs (Figure 7.1). Only focusing on blood circulation profiles or terminal tumor accumulation is similar to trying to understand a complex chain of reactions by concentrating only on the final yield of end-products. To achieve a clearer portrait, implementation of a “systems approach” provides a more coherent and robust solution. In such method each “unit” is investigated both independently and in relation with other units²¹. Consequently, the relations between NP properties and their biological performances could be addressed using a systems approach by analyzing the influence of each NP characteristic (size, charge, surface composition, and ligand density) on (i) the NP interaction with proteins in biological fluids ex vivo, and (ii) the effect of these behaviors on blood circulation, and tissue accumulation kinetics for all relevant organs (lungs, kidneys, liver, spleen)^{22, 23}. Semi-empirical models would allow us to understand and predict how a specific NP property changes when dissolved in blood, how these changes affect other NP properties, and how they affect overall tissue distribution kinetics in vivo^{23, 24}. For example, the rates at which the NPs accumulate or are cleared by different organs may be more readily correlated with NP properties in vitro and ex vivo than the circulation half-life that is a

combination of the resulting effects of individual organs. Through this approach, it may be possible to determine the key NP attributes that result in long blood circulation times, and minimal accumulation in the MPS.

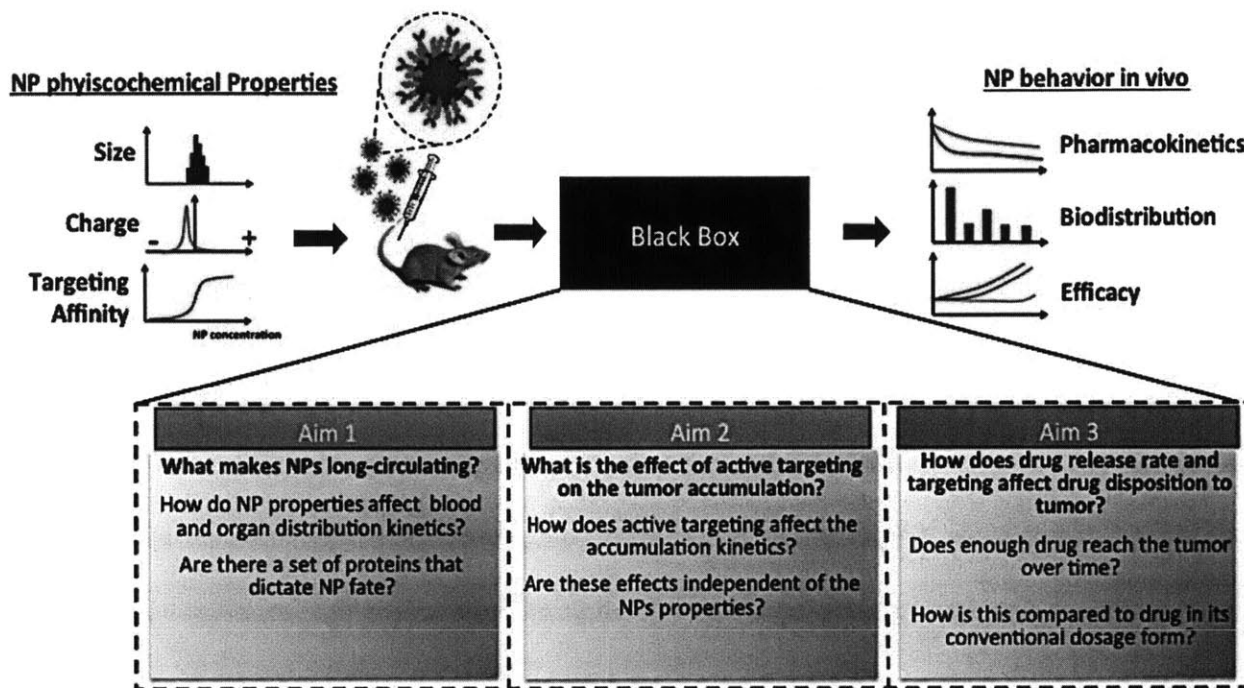


Figure 7.1. Questions to answer in future work.

(2) Impact of passive versus active targeting on the tumor accumulation kinetics: The existing paradigm behind passive targeting is that the leaky vasculature in tumor possess pores which size are between 10 to 2,000 nm, depending on the type of tumor²⁵. Small NPs can therefore passively extravasate and target tumor tissue via the so-called enhanced permeation and retention (EPR) effect simply by remaining in the circulation for sufficiently long times²⁶. In contrast, the rationale behind active targeting is that decoration of the NPs with “homing” molecules will confer them more specificity for the diseased cells, and thus that they will preferentially distribute in the tumor tissues increasing NP tumor uptake and accumulation²⁷. However, when solely measuring the distribution of targeted NPs to a tumor, the distinctive

effect of the ligand cannot be dissociated from the concomitant EPR effect. Furthermore, because most targeting ligands alter the NPs' residence time in the bloodstream, comparative studies between targeted and non-targeted formulations are biased by the inherent dissimilarities in total blood exposition. As a result, questions remain on the pertinence of using targeting ligands to enhance the specificity of NPs²⁸. While studying the NP behavior in vivo and ex vivo in healthy animals would have answered whether the targeting alters the interactions with the blood proteins and circulation properties of the NPs, our main focus here would be on providing a bona fide evaluation of the impact of the active targeting on NP tumor deposition. Our approach is to compare targeted and non-targeted NPs with similar circulation times and size with their tumor accumulation kinetics. Based on these results, data-driven semi-empirical models could be built to potentially increase further the understanding of the phenomena at stake. From these studies the aim would be to develop a mechanistic understanding of the effects of active targeting by matching pairs of targeted and non-targeted NPs with similar biophysicochemical properties and clearly assessing their effect on NP tumor accumulation.

(3) Tumor exposure to free and encapsulated drug with targeted and non-targeted nanoparticles versus the unformulated drug: Tumors offer a very heterogeneous environment where a highly disorganized network of collagen and high interstitial pressure hinders diffusion of NPs inside the hyperdense center of the tumor²⁹. Today, the vast majority on NP tumor accumulation, penetration and distribution studies focus on how deep a NP penetrates a tumor and how it is distributed away from the blood vessels. However, there is limited information, if any, on (i) how the drug released from the NP is distributed in the tumor, (ii) how this distribution changes over time, and (iii) how it is affected by the release kinetics of the NP. This leads to a bigger question on whether the concentration of drug released from the NP in the

tumor is sufficient to exert its cytotoxic effect against cancer cells and prevent cancer cells to develop resistance over time. While drug concentration kinetics in the tumor are frequently studied during the development of small molecules, this has not been the case for the development of NPs. The goal would be to develop an understanding of how NP properties (including drug release rates) affect the tumor accumulation kinetics of a drug (both free and encapsulated) and comparing it to non-encapsulated free drug, and how is this correlated to NP efficacy. Building on the knowledge acquired in previous proposed studies and utilizing formulations with comparable tumor deposition rates, one could focus on targeted and non-targeted NPs as well as slow- and fast-releasing NPs. We believe that answering these questions will be key for the future design of highly effective NP therapeutics, exploiting their full potential.

7.4. References

1. Jain, K. K., Advances in the field of nanooncology. *BMC Med* **2010**, *8*, 83.
2. Chou, L. Y.; Ming, K.; Chan, W. C., Strategies for the intracellular delivery of nanoparticles. *Chem Soc Rev* **2011**, *40* (1), 233-45.
3. Salvador-Morales, C.; Zhang, L.; Langer, R.; Farokhzad, O. C., Immunocompatibility properties of lipid-polymer hybrid nanoparticles with heterogeneous surface functional groups. *Biomaterials* **2009**, *30* (12), 2231-40.
4. Perrault, S. D.; Walkey, C.; Jennings, T.; Fischer, H. C.; Chan, W. C., Mediating tumor targeting efficiency of nanoparticles through design. *Nano Lett* **2009**, *9* (5), 1909-15.
5. Pirollo, K. F.; Chang, E. H., Does a targeting ligand influence nanoparticle tumor localization or uptake? *Trends Biotechnol* **2008**, *26* (10), 552-8.
6. Kamaly, N.; Zeyu, X.; Valencia, P. M.; Radovic-Moreno, A.; Farokhzad, O. C., Targeted polymeric therapeutic nanoparticles: design, development and clinical translation. *Chem Soc Rev* **2012**, (*In Press*).
7. Levchenko, T. S.; Rammohan, R.; Lukyanov, A. N.; Whiteman, K. R.; Torchilin, V. P., Liposome clearance in mice: the effect of a separate and combined presence of surface charge and polymer coating. *International Journal of Pharmaceutics* **2002**, *240*, 95-102.
8. Arnida; Janat-Amsbury, M.; Ray, A.; Peterson, C. M.; Ghandehari, H., Geometry and surface characteristics of gold nanoparticles influence their biodistribution and uptake by macrophages. *European Journal of Pharmaceutics and Biopharmaceutics* **2011**, *77*, 417-423.

9. Arvizo, R. R.; Miranda, O. R.; Moyano, D. F.; Walden, C. A.; Giri, K.; Bhattacharya, R.; Robertson, J. D.; Rotello, V. M.; Reid, J. M.; Mukherjee, P., Modulating pharmacokinetics, tumor uptake and biodistribution by engineered nanoparticles. *PLoS ONE* **2011**, *6*, e24374.
10. Xiao, K.; Li, Y.; Luo, J.; Lee, J. S.; Xiao, W.; Gonik, A. M.; Agarwal, R. G.; Lam, K. S., The effect of surface charge on in vivo biodistribution of PEG-oligocholeic acid based micellar nanoparticles. *Biomaterials* **2011**, *32*, 3435-3446.
11. He, C.; Hu, Y.; Yin, L.; Tang, C.; Yin, C., Effects of particle size and surface charge on cellular uptake and biodistribution of polymeric nanoparticles. *Biomaterials* **2010**, *31*, 3657-3666.
12. Gabizon, A.; Papahadjopoulos, D., Liposome formulations with prolonged circulation time in blood and enhanced uptake by tumors. *Proceedings of the National Academy of Sciences of the United States of America* **1988**, *85*, 6949-6953.
13. Yamamoto, Y.; Nagasaki, Y.; Kato, Y.; Sugiyama, Y.; Kataoka, K., Long-circulating poly(ethylene glycol)-poly(D,L-lactide) block copolymer micelles with modulated surface charge. *Journal of Controlled Release* **2001**, *77*, 27-38.
14. Cho, W. S.; Cho, M.; Jeong, J.; Choi, M.; Han, B. S.; Shin, H. S.; Hong, J.; Chung, B. H.; Cho, M. H., Size-dependent tissue kinetics of PEG-coated gold nanoparticles. *Toxicol Appl Pharmacol* **2010**, *245* (1), 116-23.
15. Cabral, H.; Matsumoto, Y.; Mizuno, K.; Chen, Q.; Murakami, M.; Kimura, M.; Terada, Y.; Kano, M. R.; Miyazono, K.; Uesaka, M.; Nishiyama, N.; Kataoka, K., Accumulation of sub-100 nm polymeric micelles in poorly permeable tumours depends on size. *Nat Nanotechnol* **2011**, *6* (12), 815-23.
16. Gu, F.; Zhang, L.; Teply, B. A.; Mann, N.; Wang, A.; Radovic-Moreno, A. F.; Langer, R.; Farokhzad, O. C., Precise engineering of targeted nanoparticles by using self-assembled biointegrated block copolymers. *Proc Natl Acad Sci U S A* **2008**, *105* (7), 2586-91.
17. Choi, C. H.; Alabi, C. A.; Webster, P.; Davis, M. E., Mechanism of active targeting in solid tumors with transferrin-containing gold nanoparticles. *Proc Natl Acad Sci U S A* **2010**, *107* (3), 1235-40.
18. Alexis, F.; Pridgen, E.; Molnar, L. K.; Farokhzad, O. C., Factors affecting the clearance and biodistribution of polymeric nanoparticles *Molecular Pharmaceutics* **2008**, *5* (4), 505-515.
19. Bertrand, N.; Leroux, J. C., The journey of a drug carrier in the body: an anatomophysiological perspective. *Journal of Controlled Release* **2012**, *x*, Epub ahead of print.
20. Li, S. D.; Huang, L., Pharmacokinetics and biodistribution of nanoparticles. *Mol Pharm* **2008**, *5* (4), 496-504.
21. Kitano, H., A robustness-based approach to systems-oriented drug design. *Nat Rev Drug Discov* **2007**, *6* (3), 202-210.
22. Yamamoto, Y.; Nagasaki, Y.; Kato, Y.; Sugiyama, Y.; Kataoka, K., Long-circulating poly(ethylene glycol)-poly(D,L-lactide) block copolymer micelles with modulated surface charge. *J Control Release* **2001**, *77* (1-2), 27-38.
23. Blanco, E.; Bey, E. A.; Khemtong, C.; Yang, S. G.; Setti-Guthi, J.; Chen, H.; Kessinger, C. W.; Carnevale, K. A.; Bornmann, W. G.; Boothman, D. A.; Gao, J., Beta-lapachone micellar nanotherapeutics for non-small cell lung cancer therapy. *Cancer Res* **2010**, *70* (10), 3896-904.
24. Li, M.; Al-Jamal, K. T.; Kostarelos, K.; Reineke, J., Physiologically based pharmacokinetic modeling of nanoparticles. *ACS Nano* **2010**, *4* (11), 6303-17.
25. Hobbs, S. K.; Monsky, W. L.; Yuan, F.; Roberts, W. G.; Griffith, L.; Torchilin, V. P.; Jain, R. K., Regulation of transport pathways in tumor vessels: role of tumor type and

microenvironment. *Proceedings of the National Academy of Sciences of the United States of America* **1998**, *95* (8), 4607-4612.

26. Matsumura, Y.; Maeda, H., A new concept for macromolecular therapeutics in cancer chemotherapy: mechanism of tumorotropic accumulation of proteins and the antitumor agent smancs. *Cancer Research* **1986**, *46*, 6387-6392.

27. Huynh, N. T.; Roger, E.; Lautram, N.; Benoit, J. P.; Passirani, C., The rise and rise of stealth nanocarriers for cancer therapy: passive versus active targeting. *Nanomedicine (Lond)* **2010**, *5* (9), 1415-33.

28. Duncan, R.; Gaspar, R., Nanomedicine(s) under the microscope. *Mol Pharm* **2011**, *8* (6), 2101-41.

29. Jain, R. K.; Stylianopoulos, T., Delivering nanomedicine to solid tumors. *Nature Reviews: Clinical Oncology* **2010**, *7*, 653-664.

Appendix 1. Supporting information for chapter 2.

1. Comparing NPs with microfluidics vs. NP with previously published method

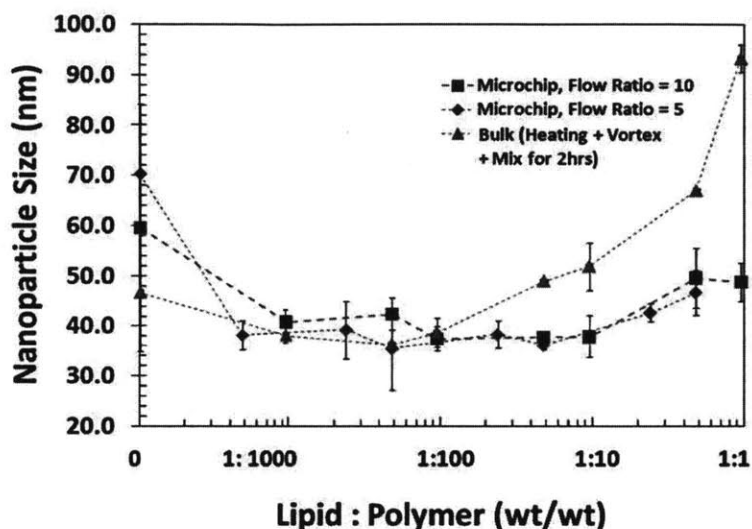


Figure A1.1. Changes in average NP size dependency on lipid:polymer (wt/wt).

Average NP sizes at different lipid concentrations from NPs prepared using a prior method described L. Zhang, et al., 2008, are also included for comparison purposes. From 1:1 all the way to 1:100 lipid to PLGA ratio the NP size obtained from the microfluidic synthesis is smaller than those prepared in “bulk.” As shown in Figure 2.2a, changes in flow ratio does not seem to have a significant effect on NP size.

2. Change in size over time of nanoparticles made with different precursors at different conditions

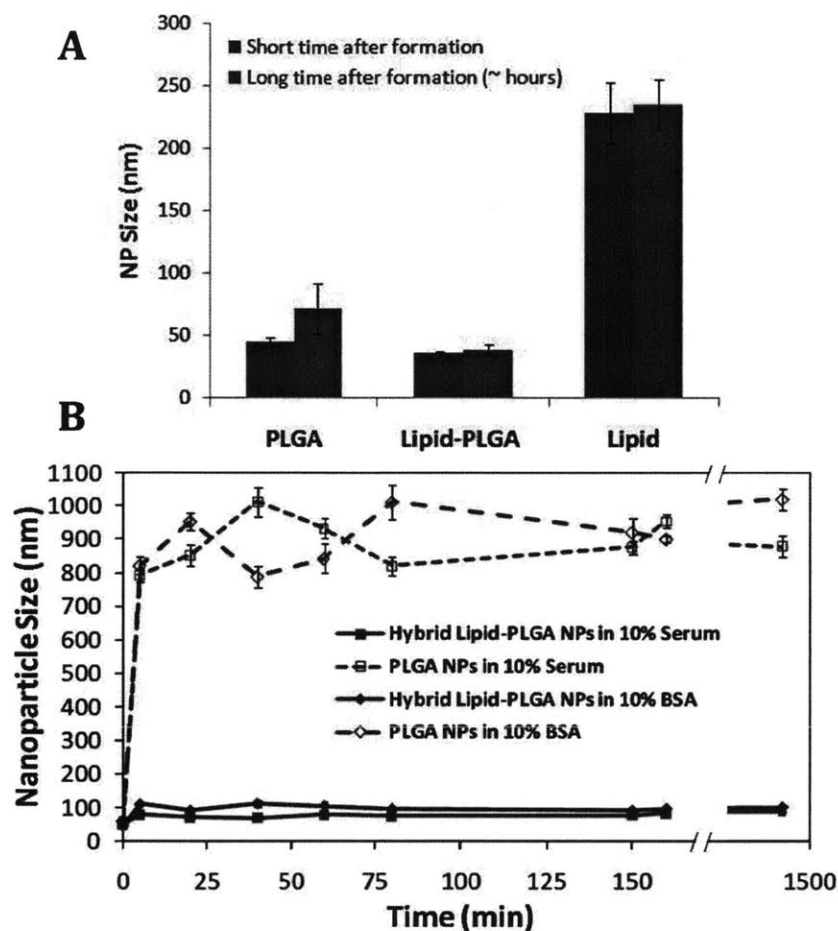


Figure A1.2. Effect of time on NPs made with different precursors and at different conditions.

(A) NPs in water made with polymer only initially had a size of 40-50 nm and then increase to a size of 50-100nm within a few hours of formation. NPs made with both lipid and polymer had a size of 40nm, which remained essentially unchanged within several hours. NPs made with only lipid had a wide distribution of sizes ranging from 200-300nm but the sizes did not change within several hours. (B) Hybrid Lipid-polymeric NPs were stable in both 10% BSA and 10% Serum at 37°C. In contrast, PLGA NPs had a dramatic increase in size after they were incubated in BSA and Serum.

3. Investigating the effect of DSPE-PEG on lipid-PLGA NP stability

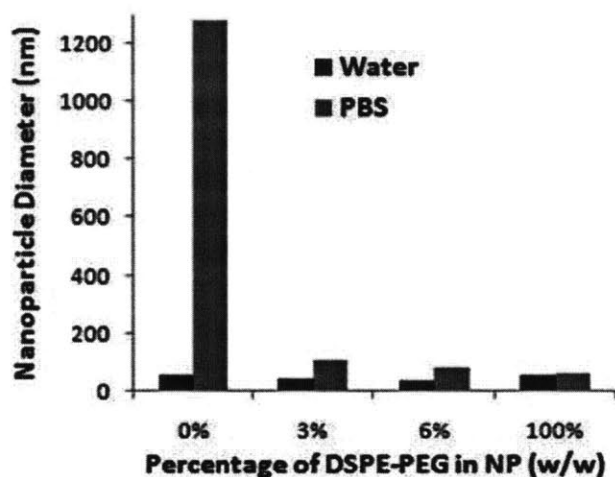


Figure A1.3. Effect of DSPE-PEG in stability of lipid-PLGA NP.

When DSPE-PEG is absent, although there is a lipid layer around the polymeric core, the resulting NP is not stable in PBS. When the amount of DSPE-PEG is increased to 3% a slight increase in NP size is observed when NPs are suspended in PBS compared to water. A smaller increase in NP size is observed for 6% of DSPE-PEG and an insignificant increase in size is observed when only DSPE-PEG covers the polymeric core.

4. NPs made at slow mixing conditions

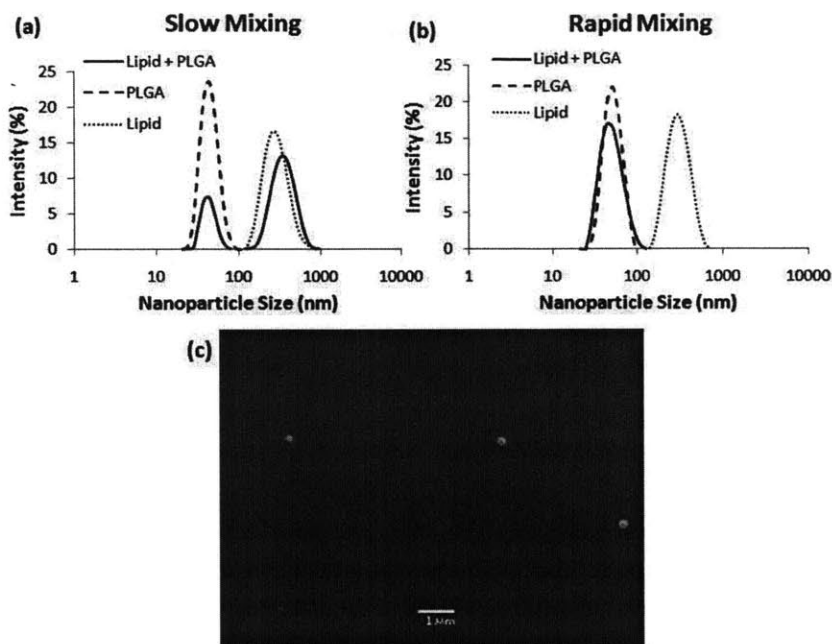


Figure A1.4. Size distribution of hybrid NPs with different properties.

(a) Size distribution of NPs made at slow mixing conditions. (b) Size distribution of NPs made at rapid mixing using microfluidic channels. Solid line: NPs obtained from a mixture of PLGA and lipid at a lipid to polymer ratio of 1 : 10. Note that two distinct peaks are present at the characteristic size of polymeric NPs (50nm) and liposomes (250nm). Dashed line: NPs obtained when only PLGA is present. Dotted line: NPs obtained when only lipid is present. (c) SEM image of NPs made from a mixture of PLGA and lipid at a lipid to polymer ratio of 10 : 1. Because of the resolution limitations of SEM only NPs with size larger than about 150nm can be observed. The NP sizes shown in this image are 170nm, 250nm, and 290nm, and are characteristic of liposomes. Scale bar is 1μm. Before imaging, NPs were sputtered with few nanometers of gold. Acceleration voltage used was 15kV.

5. Determining mixing time in channel

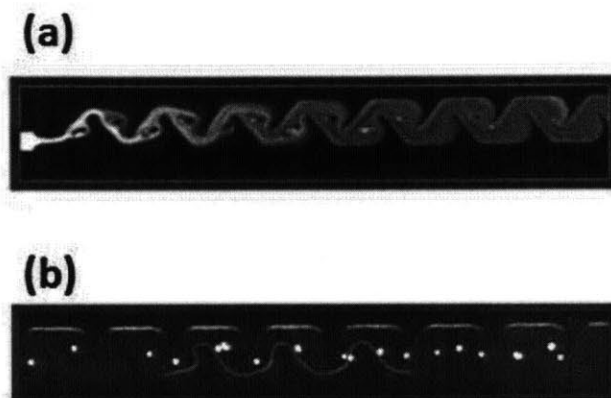


Figure A1.5 Determination of mixing time.

(a) Using fluorescent dye as the input in the organic solvent stream, complete mixing occurs at 1.4 cm in the Tesla channels. (b) Observation of fluorescent bead transport used to calculate mixing time within the channel design. First the track length of the bead at a specific exposure time is calculated from the image. From the track length and exposure time, the fluid velocity was calculated. In this study the track length used to calculate the fluid velocity was the average of 50 track lengths measured from 50 different images. In addition, other different fluid velocities at different exposure times were measured and no significant variability was found. The mixing time of ~ 10 ms was determined by using the average fluid velocity times the distance at which complete mixing was observed.

6. Self-assembly of lipid-QDs NPs inside microfluidic channel

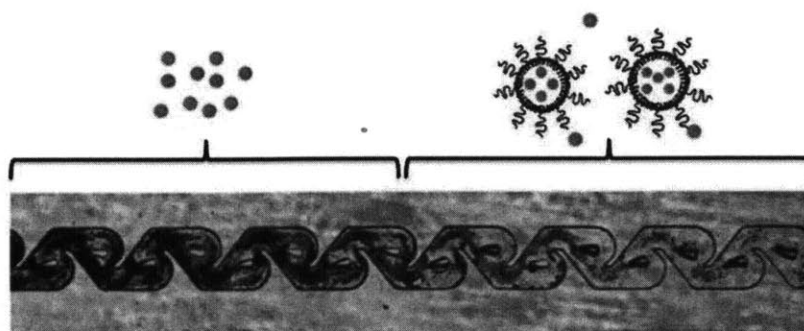


Figure A1.6. Observation of self-assembly.

Light microscope screen capture of entire Tesla channel ($60 \mu\text{m} \times 20 \mu\text{m}$) illustrating areas of QD aggregation followed by lipid coverage in the formation of hybrid-QD NPs.

Appendix 2 – Supporting information for chapter 3

Synthesis of PLGA and PLGA-PEG NPs

Figure A2.1 shows how PLGA particles easily grow and aggregate on the channel wall when they encounter the anti-solvent (water) under the Phase II conditions (similar aggregation also occurs in 2D HFF). 3D HFF under Phase I conditions, however, provided a robust and predictable means to successfully synthesize PLGA nanoparticles at the equivalent condition without any aggregation.

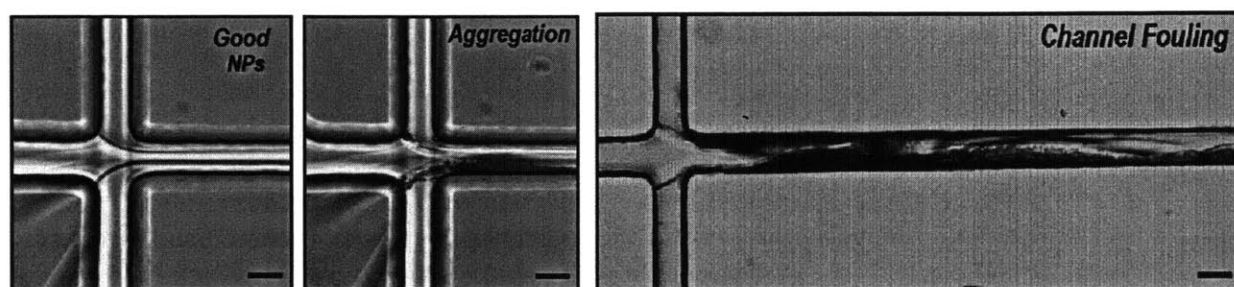


Figure A2.1. Synthesis of PLGA NPs.

Synthesis of PLGA NPS from pure PLGA_{70K} precursors (10 mg/mL) by 3D HFF for varying operation parameters. (a) Channel image at the conditions that result good synthesis of NPs and (b) that are susceptible to aggregation. (c) Channel fouling due to long-term aggregation of PLGA microparticles (bottom) (scale bars 20 μm).

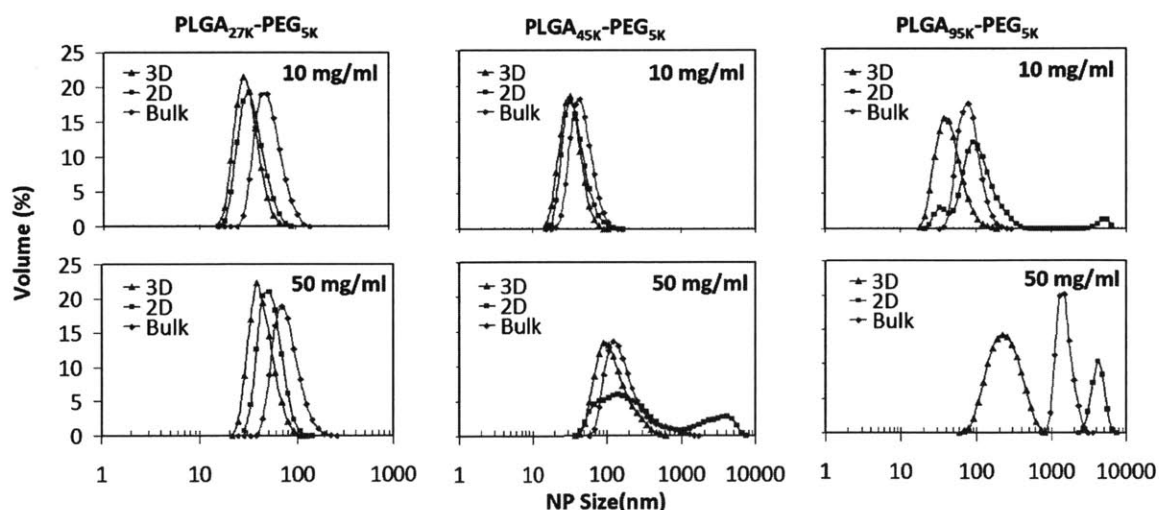


Figure A2.2. Comparison of size distributions by volume fraction of PLGA-PEG NPs.

NPs prepared by microfluidic 3D HFF, 2D, and bulk mixing methods for the precursor concentrations of 10 (low) and 50 mg/mL (high), respectively. Aggregated particles are found in the 1000-10,000 nm range.

Figure A2.2 shows the size distributions of NPs made from various MW polymer precursors at low and high concentrations (10mg/mL and 50mg/mL, respectively) using the three different methods. At high concentrations, NPs obtained by 2D HFF and bulk methods yielded highly polydisperse particles of extremely large size (>1000 nm), while the implementation of 3D HFF consistently resulted in smaller NPs with relatively low polydispersity regardless of polymer concentrations. These observations indicate that 2D HFF is comparable with 3D HFF only for small MW polymers or very low polymer concentrations where the channels are less susceptible to fouling.

Aggregated particles are larger and thus reflect more light so that the solution with aggregated particles can look opaque. Figure A3.3 shows direct visualization of collected sample solutions that contain synthesized PLGA-PEG particles with various sizes.

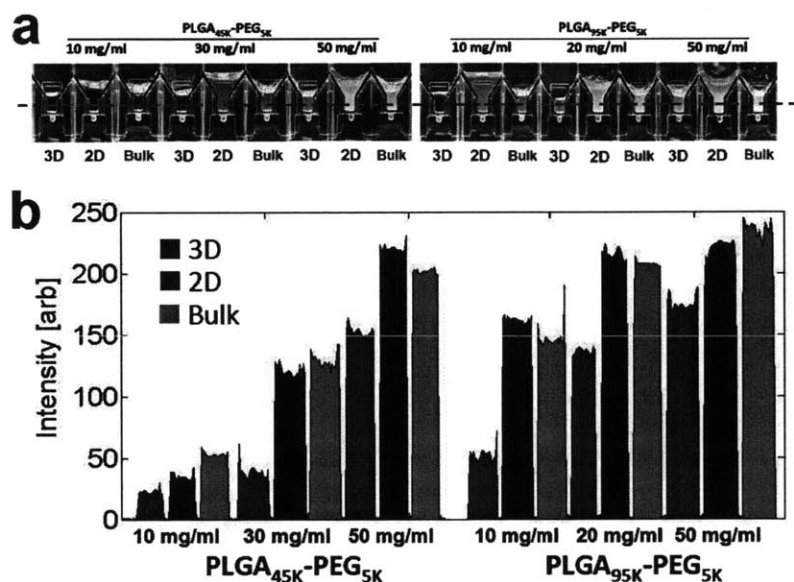


Figure A2.3. Cloudiness of various PLGA-PEG NPs.

(a) Photos of NP solutions prepared by 3D HFF, 2D HFF, and bulk synthesis. Opacity of the solution roughly indicates the average size of NPs in the solution. Clear solutions contain small NPs (< ~50 nm) and opaque solutions have large particles up to several microns. (b) Calculated light intensity along the red dashed line in (a) to estimate the opacity of the solutions.

Appendix 3 – Supporting information for chapter 4

Table A3.1. Gel Permeation Chromatography (GPC) on TL-conjugated and non-conjugated PLGA-PEG copolymers

Polymer	Mn	Mw	PID
PLGA	40,066	54,103	1.35
PEG	4,603	5,221	1.13
PLGA-PEG	47,751	57,703	1.21
PLGA-PEG-Folate	49,551	59,789	1.20
PLGA-PEG-RGD	50,005	61,002	1.22

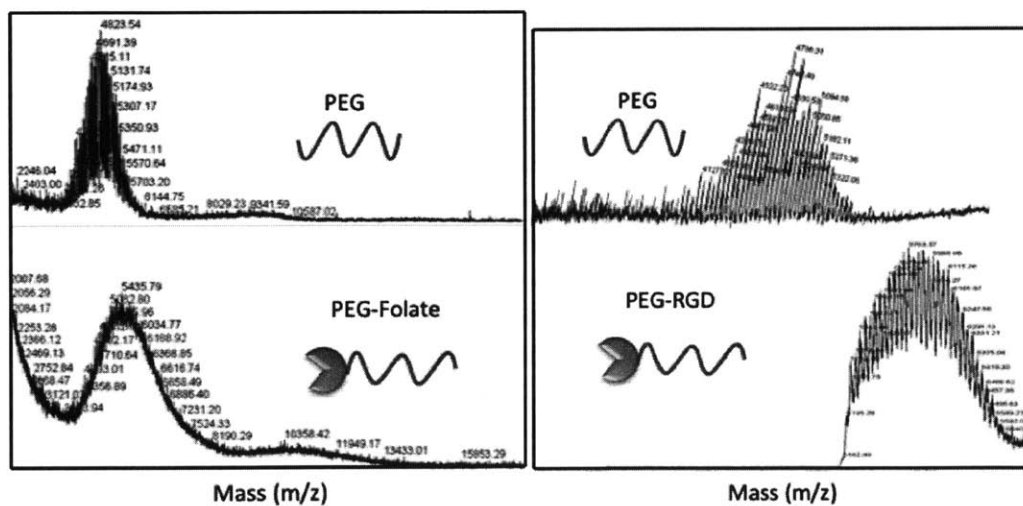


Figure A3.1 . MALDI-TOF to verify conjugation of PEG-RGD and PEG Folate.
Note: No free folate or free RGD was observed.

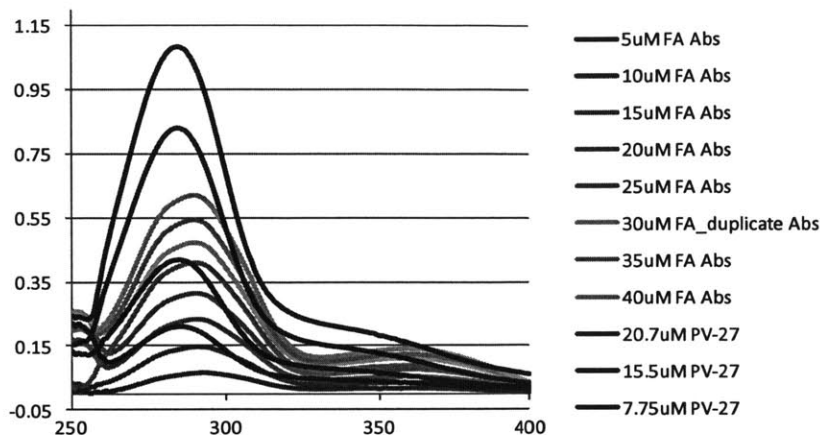


Figure A3.2. UV-VIS to quantify amount of folate present on PLGA-PEG-Folate
 Yellow/green colors correspond to calibration points and red corresponds to PLGA-PEG-Folate.

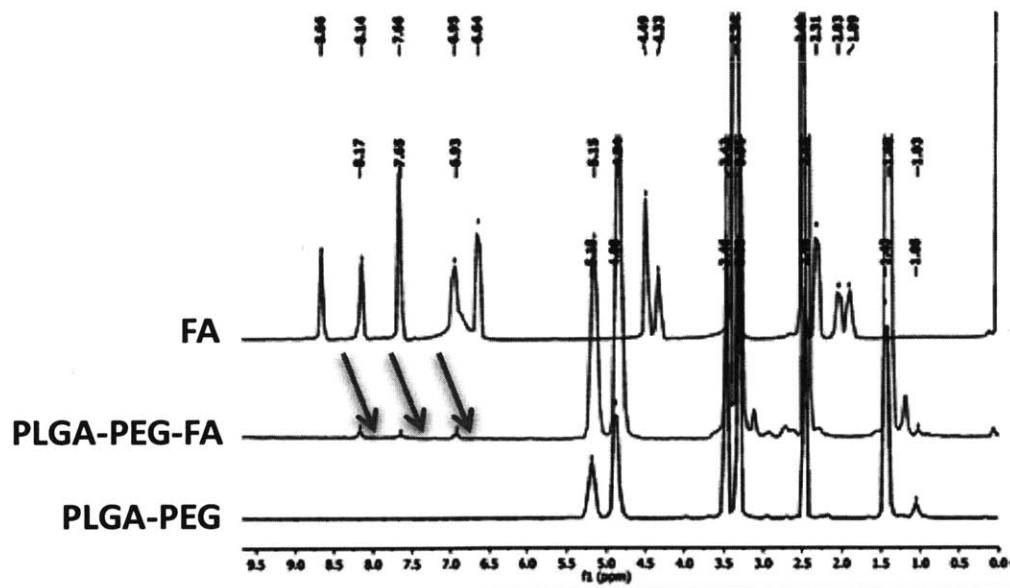


Figure A3.3. 1H NMR on PLGA-PEG-Folate

Among other factors, PLGA-PEG-Folate and PLGA-PEG-RGD conjugation efficiencies might affect the accuracy of the comparison of expected versus detected number of folate and RGD molecules on the nanoparticle surface. However, EDC/NHS reactions are known to high efficiencies up to 95% (Lee, S., Murthy, N., Biochem and Biophys Res Comm., 360 p275-9, 2007).

Appendix 4. Supporting information for chapter 6

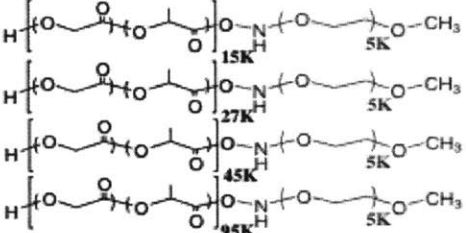
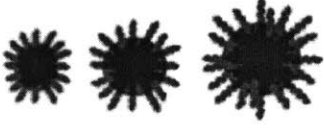
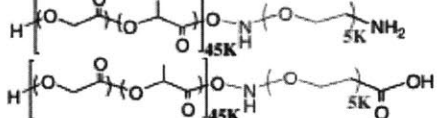
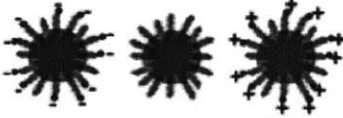
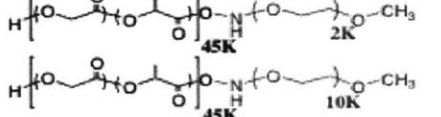

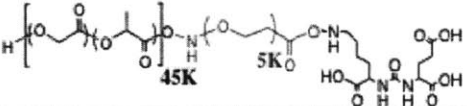
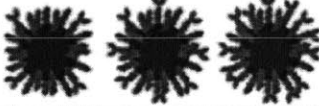
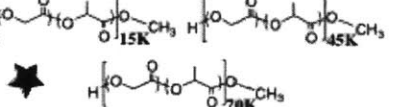

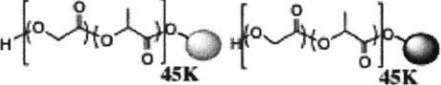
Nanoparticle Precursors	Nanoparticle Property Controlled
<p>PLGA-PEG with different MW of PLGA blocks</p> 	<p>Size</p> 
<p>PLGA-PEG with different PEG functional end-group</p> 	<p>Charge</p> 
<p>PLGA-PEG with different MW of PEG block</p> 	<p>Surface hydrophobicity</p> 
<p>PLGA-PEG-LIG</p> 	<p>Targeting ligand density</p> 
<p>Hydrophobic Drug and PLGA of different MW</p> 	<p>Drug Loading and release</p> 
<p>PLGA-fluorescent probe or -radioactive probe</p> 	<p>None – used for detection <i>in vitro</i> and <i>in vivo</i> experiments.</p>

Figure A4.1. NP precursors used for the synthesis of NP library with a wide range of physicochemical properties.

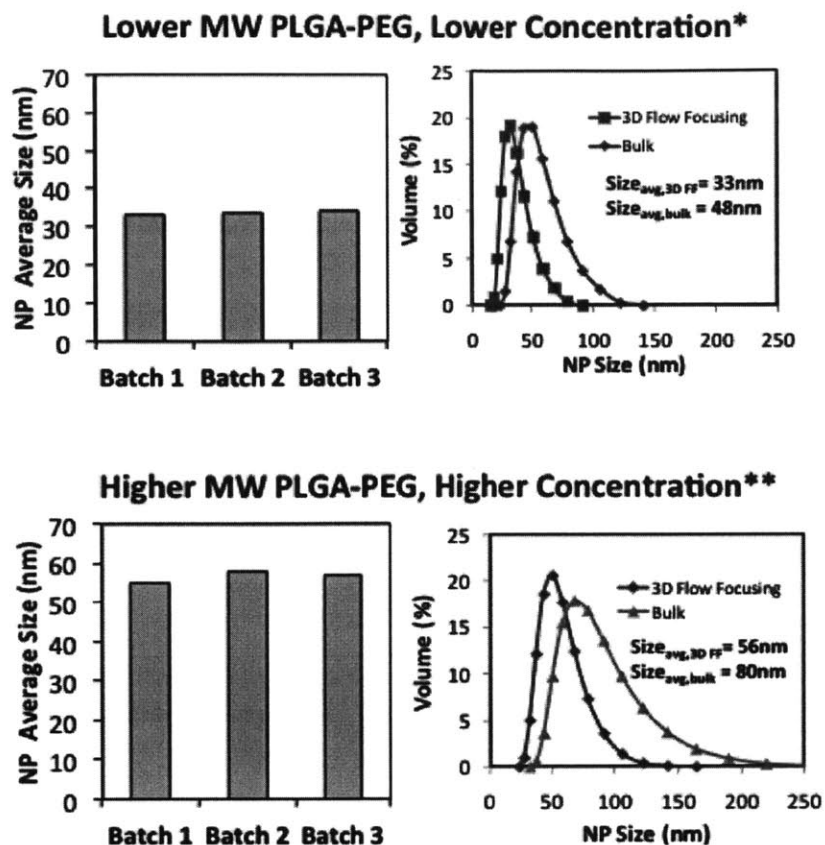


Figure A4.2. Batch-to-batch reproducibility of targeted NPs prepared in the microfluidic system.

Comparison of size distribution obtained by microfluidic synthesis versus bulk synthesis.

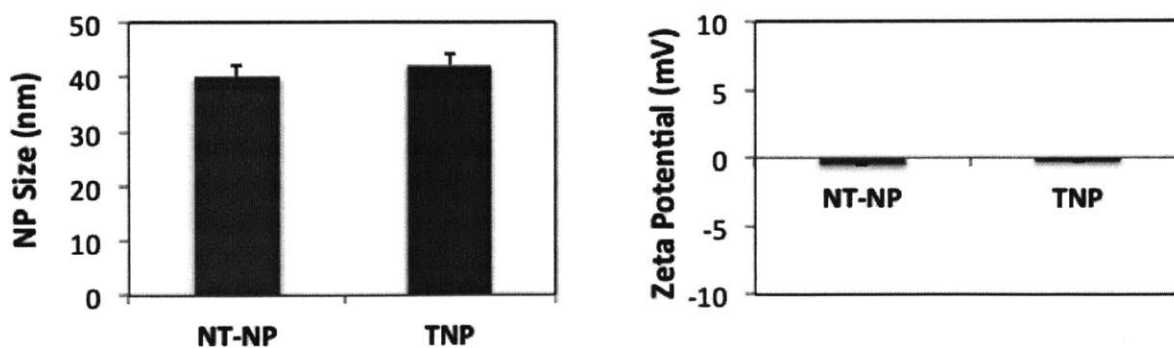


Figure A4.3. Average size and zeta potential of non-targeted NPs (NT-NP) and targeted NPs (TNP).